ROBUST NONLINEAR OBSERVER

FOR A NON-COLLOCATED FLEXIBLE MOTION SYSTEM

A Thesis
Presented to
The Academic Faculty

by

Mohsin Waqar

In Partial Fulfillment
of the Requirements for the Degree
Masters of Science in the
George W. Woodruff School of Mechanical Engineering

Georgia Institute of Technology
May 2008

ROBUST NONLINEAR OBSERVER

FOR A NON-COLLOCATED FLEXIBLE MOTION SYSTEM

Approved by:

Dr. Wayne J. Book, Advisor
School of Mechanical Engineering
Georgia Institute of Technology

Dr. Nader Sadegh
School of Mechanical Engineering
Georgia Institute of Technology

Dr. Stephen Dickerson, Emeritus
School of Mechanical Engineering
Georgia Institute of Technology

Date Approved: 4/31/2008

ACKNOWLEDGEMENTS

TABLE OF CONTENTS

LIST OF TABLES

LIST OF FIGURES

SUMMARY

Robustness of the closed-loop system has repercussions on both stability and performance, making the study of robustness very important. Fundamentally, the performance and stability of closed-loop systems utilizing state-feedback are tied to that of the observers. The primary goal of this thesis is to develop a robust nonlinear observer and closely examine the usefulness of the observer in the presence of non-collocation and parametric uncertainty and as an integral component in closed-loop control. The usefulness of the observer being investigated depends on robustness, accuracy, computational burden, 'tunability,' ease of design, and ease of implementation on an actual flexible motion system.

The design and subsequent integration of the Kalman filter, an optimal observer, into a closed-loop system is well known and systematic. However, there are shortcomings of the Kalman filter in the presence of model uncertainty which are highlighted in this work. Simulation studies are conducted using the Simulation Module in National Instruments LabVIEW 8.5 and experiments are conducted on a physical system consisting of a single flexible link with non-collocation of actuators and sensors using LabVIEW Real Time 8.5. Simulations serve as a means to analyze the performance of the optimal observer and the robust observer by analyzing their dynamic behavior as well as that of the closed-loop system with each observer in place. The focus of experiments is on investigating implementation of the robust observer, including initialization and tuning of observer design parameters off-line and on-line.

Simulations verify the robustness properties of the sliding mode observer while experiments show that the robust observer can be implemented at fast control rates and that replacing the Kalman filter with a robust observer has direct ramifications on closed-loop performance.

CHAPTER 1

INTRODUCTION

1.1 Background and Problem Statement

Control of long-reach yet light-weight space and industrial manipulators are two immediate benefits of on-going research on the topic of flexible motion systems. A potentially farther reaching benefit is the possibility of improving the accuracy and precision of any robotic manipulator in which actuators and sensors are non-collocated. Such manipulators are not common today in industry precisely because of the challenging control problem. Greater design freedom in the design of manipulators will exist if we can use advanced control theory combined with modern technology to apply control torques at distances through a flexible structure and achieve not just stable but high performance control.

The basic approach taken in this thesis work falls under improved control algorithms for feedback control, which is a proven approach for employing flexible motion systems [1]. While a wide range of design objectives for a robotic manipulator may exist, measures related to either stability or performance that controls practitioners often care about include local or global stability regions, speed of response and positioning accuracy and repeatability of the useful endpoint of the link. When stationary, we want to ensure the steadiness of the end point of the link by removing residual vibrations.

1.1.1 Motivation

Robustness of the closed-loop system has repercussions on both stability and performance, making the study of robustness very important. The study of robustness may entail studying how sensitive the flexible motion system is to temporary or persistent

disturbances and model uncertainty. Model uncertainty can be broken down into parametric uncertainty (structured uncertainty) and unstructured uncertainty. Parametric uncertainty is often easier to characterize. For example, the inertia of the flexible link may be known to lie between a lower and upper amount. An example of unstructured uncertainty is unmodeled dynamics (i.e. actuator dynamics or higher flexible modes).

There is further motivation for studying robustness. The controls problem is very challenging when the system is inherently non-minimum phase. The combination of non-collocation and the flexible nature of the link is the cause of non-minimum phase behavior. The time delay between torque input at one end of the link and tip displacement at the other end, caused by a finite wave propagation speed, is the culprit. Model-based controllers hold promise for high performance control yet frequently encountered model inaccuracy can severely affect the stability and consistent performance of a closed-loop control system [2]. The combination of model inaccuracy and the presence of non-collocation, and hence non-minimum phase behavior under the right circumstances, exacerbates the situation. The study of robustness of a non-minimum phase closed-loop control system to model inaccuracy is thus of high interest.

PID based joint control based on tip position has been shown to fail. State-feedback control on the other hand has been shown to be effective at driving the link tip to a desired position or at a desired velocity while commanding vibrations towards zero [2]. However, there are two obstacles to this control approach. First, an observer for estimating the complete state based on imperfect real world measurements becomes crucial. Second, state-feedback control has been shown to be sensitive to small changes in payload and parameters [3]. Hence, the focus of this work on observers in the presence of model uncertainty. An overview of the state-feedback controller and observer used in this work can be found in section 1.2.2.

1.1.2 Problem Statement

The primary goal of this thesis then is to develop a robust nonlinear observer and closely examine the usefulness of the observer for application to control of a flexible robotic link in the presence of non-collocation and parametric uncertainty and as an integral component in closed-loop control. The usefulness of the observer being investigated depends on robustness, accuracy, computational burden, 'tunability,' ease of design, and ease of implementation on a physical flexible motion system. Details of the experimental test-bed can be found in section 6.1. An important distinction at this point is that directly comparing the performance of the sliding mode observer to the Kalman filter, an optimal observer common in practice will better place the performance of the observer into useful context and allow the reader to judge the sliding mode observer for what its worth.

1.2 Non-collocation and Control Overview

Non-collocation of actuators and sensors offers at least two benefits. Greater precision can result in theory by placing the sensor at the useful end of a robotic link, collocated with end-of-arm tooling instead of the actuator. Truly high precision is achievable by minimizing error at the tool and not at the joint. Cost is often the overruling factor in design, taking precedence over performance. The number and placement of actuators and sensors determines the cost of implementing control. Naturally, non-collocation may be the direct result of cost considerations. Lastly, non-collocation may result because of the physical impossibility of collocating actuators.

1.2.1 Non-collocation and Non-minimum Phase Behavior

Improved dynamic modeling plays a critical role in non-collocated systems. It is important for the model to properly represent the non-minimum phase behavior if it is present. One way in which the presence of non-minimum behavior is detected is by

looking at system zeros. Positive zeros are a direct indication. It is readily seen that since the zeros of a system depend on the <u>A</u>, <u>B</u> and <u>C</u> matrices in the state-space realization of the system, the system zeros depend on the placement of actuators and sensors.

Another way in which the presence of non-minimum behavior is detected is by studying the time response plot. If there are an odd number of positive system zeros, there will be initial undershoot. Initial undershoot is another direct indication of non-minimum phase behavior. That is, the flexible link tip initially moves in the reverse direction. Multiple positive system zeros mean multiple direction reversals in a step response [4].
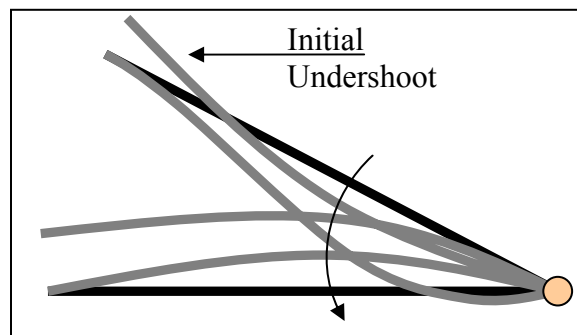
Figure 1.1: Motion of a flexible robotic link.

Non-minimum phase zeros limit closed-loop performance. This is because the closed-loop poles are made up of open-loop poles and zeros. As loop gain increases, poles move towards unstable zeros and destabilization occurs when the loop transfer function has non-minimum phase zeros. Such systems have limited gain margins which implies a limit on the robustness of the closed-loop system.

Non-collocation on its own presents a challenging control problem. There is a direct correlation between parameter uncertainty and instability of a non-collocated closed-loop system. In certain non-collocated systems, system poles and zeros alternate as one moves up the imaginary axis in the s-plane. In such systems, zero flipping occurs

as parameters vary according to Canon [5]. Zero flipping refers to a zero moving in between system poles. This occurs because system zeros are actually more sensitive than system poles to parameter variation. Even more so in the presence of low damped modes, in which case the zero does not need to be shifted far before zero flipping directly leads to system instability.
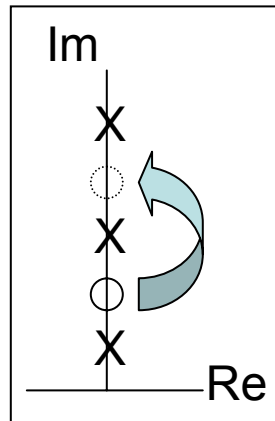
Figure 1.2: Zero flipping due to parameter variation in non-collocated system.

1.2.2 Observer and Controller

A typical approach is to separate the problem of estimation and control. This is a simpler two-step approach which works well for linear systems. The block diagram depicted in Figure 1.3 is based on the experimental test-bed to be discussed in section 6.1. Also note that the simulations to be discussed in Chapter 5 are also based on the same control system structure. The observer plays a critical role in the closed-loop system at hand. Based on imperfect measurements from the real world, the observer estimates the complete state to be used for state-feedback. The two observers tested are the Kalman filter and the sliding mode observer. Their performance is judged based on the quality of their estimates and the performance of the closed-loop control system in the presence of parameter uncertainty.
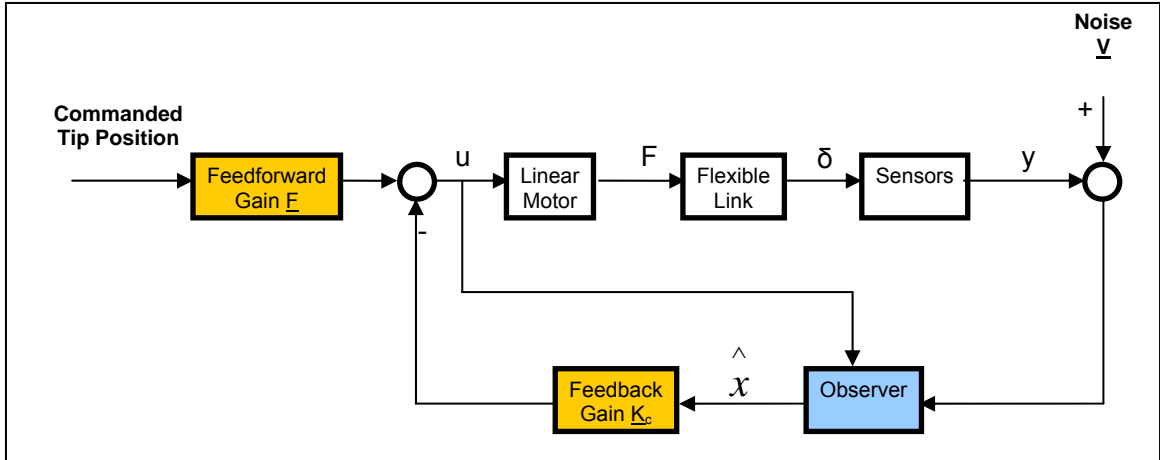
Figure 1.3: Block diagram of control system.

In this thesis work, locating the closed-loop poles is based on the method of symmetric root locus, a version of the optimal linear quadratic regulator problem. In this method, the closed-loop poles are restricted to the locus. This convenient approach allows the designer to achieve a balance between tracking error and control effort by tuning a single parameter, τ. Appendix A provides the procedure for design of the symmetric root locus. In addition, a feed-forward term is used for properly introducing a non-zero reference input to the controller. Appendix B provides the procedure for design of the feed-forward gain.

1.3 Literature Review for Robust Observer

Slotine et al [6] suggest a general design procedure based on the variable structure systems theory for a sliding mode observer for nonlinear systems with bounded nonlinearities and uncertainties. The design problem is essentially an arbitrary pole placement problem for selecting the observer gains. In a direct comparison with the Kalman filter, the authors show that in a simple linear system in the presence of bounded parametric uncertainty, the sliding mode observer produces stable estimates with reduced error.

6

Chalhoub and Kfoury [7] design a fourth order sliding mode observer with a single collocated measurement for a single flexible link manipulator under closed-loop control. A nonlinear model of the flexible link based on the Lagrangian approach is used in simulations. They adapt Slotine's variable structure systems theory based observer design with modifications to the observer structure. They present a unique method for selecting time-varying switching gains, in which each element of the observer gain matrix is selected one at a time based on designated constraints. Based on simulations, they show that in the presence of parametric uncertainty, closed-loop control based on estimates is stable. They attempted but failed to show robustness of the observer in open-loop form to unmodeled dynamics. With a similar observer design approach as their previous work, Chalhoub and Kfoury [8] design a sixth order sliding mode observer with three measurements for estimating the rigid and flexible motion present in an internal combustion engine, presenting only simulations.

Diverting from the variable structure system theory approach proposed by Slotine, Kim and Inman [9] design a sliding mode observer for an active cantilevered beam based on a Lyapunov-based approach. Based on simulations, they report unstable estimates under impulse response by the Kalman filter in the presence of uncontrolled modes while the sliding mode observer estimates remain stable. Based on experimental results, they go on to show that their closed-loop system with the sliding mode observer with both parametric uncertainty and residual modes under impulse response remains stable and in fact reduces vibrations while the system with the Kalman filter goes unstable. The distinction should be made that their system is not a motion system.

Elbeheiry and Elmaraghy [10] design an eight order sliding mode observer with two measurements based on the Lyapunov-based approach for a two link flexible joint manipulator under PI joint control. Simulations and experimental results are presented, however like Zaki [11], the observer is not part of the closed-loop. More significantly, they do not directly showcase the robustness properties of the sliding mode observer.

Instead they discuss the performance of a Luenberger/sliding mode switching observer which resembles gain scheduling. However, they do offer a methodology, a set of conditions rather than a systematic procedure, for proper sliding mode observer design.

Zaki et al [11] design a fourteenth order sliding mode observer based on the Lyapunov-based approach for a two flexible link manipulator under PD joint control. Simulations are conducted with a linearized system model along with the sliding mode observer and a boundary layer placed on the switching surface. His results verify that the sliding mode observer produces stable estimates in the presence of parametric uncertainty in open-loop form. Experimental results are presented, showing accurate tip velocity estimates with the observer in open-loop form, with no parametric uncertainties. A set of conditions for proper sliding mode observer design is presented, similar to the one published by Elbeheiry and Elmaraghy [10], both of who are co-authors of this work by Zaki.

CHAPTER 2

SYSTEM MODEL

The control algorithm for feedback control in this research involves model based observers and controllers. The flexible motion system is decomposed into flexible and rigid subsystems. The models for the flexible subsystem are used in design of the controller and observer used in both simulations and for experiments. The model for the rigid subsystem on the other hand was a means to identify critical parameters needed for control of the hardware. The rigid subsystem model is not directly used in any simulation.

2.1 Flexible Sub-System

A model for a flexible subsystem considers the energy stored in the form of kinetic and potential energy when the link is twisted, compressed or bent. A more accurate model will consider energy storage from all three of these deformations. However, for real time control purposes, models may be simplified at the cost of accuracy to reduce the computational burden. If kinetic and potential energy storage is separated in lumped components, the model will lead directly to ordinary differential equations. This approach leads to what is referred to as a lumped parameter model. A model of this form is detailed in section 2.1.

Distributed parameter models on the other hand consider the spatially distributed nature of mass and compliance [2]. Such models consider the simultaneous storage of kinetic and potential energy in a continuous element such as a bar [12]. In such a model, location of a point on the link can be described by rigid body motion of the link and elastic deflection. A model of this form is detailed in section 2.2.

2.1.1 Simple Model

In a lumped parameter model for the flexible subsystem, the flexible link is made up of discrete inertias and springs. Dissipation effects may be modeled by including discrete dampers. Knowledge of rigid body inertias, spring constants and damper coefficients allows specification of the equations of motion. The flexible subsystem is described by one second-order ordinary differential equation per degree/order of the flexible subsystem. Thus the model has finite degrees of freedom meaning a finite number of modes.

Figure 2.1 depicts a lumped parameter model that illustrates the principles of non-minimum phase in a flexible link. Here m_1 represents the lumped (particle) tip mass and m_2 represents the base mass as a rigid body at the sliding end. The arrangement of the discrete spring k and damper c leads to non-minimum phase behavior which is observable in the response of the tip mass. A concentrated external force is applied to the rigid body at the link base.
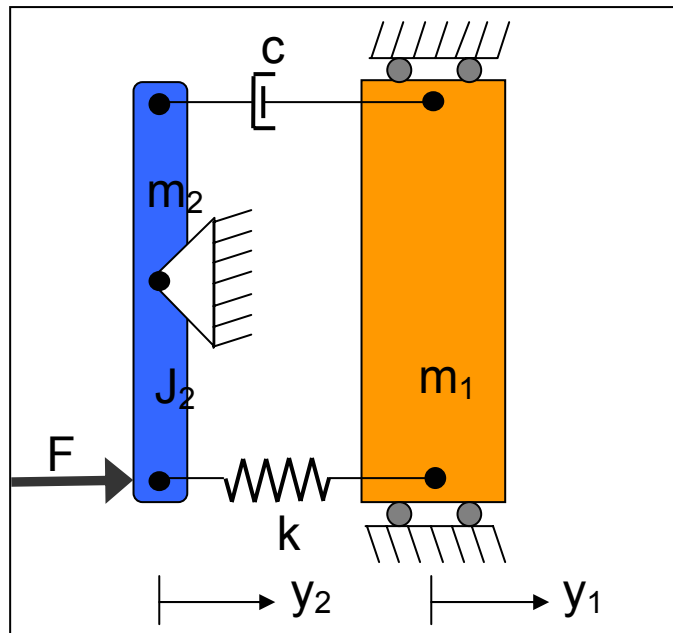
Figure 2.1: Lumped parameter model for flexible link.
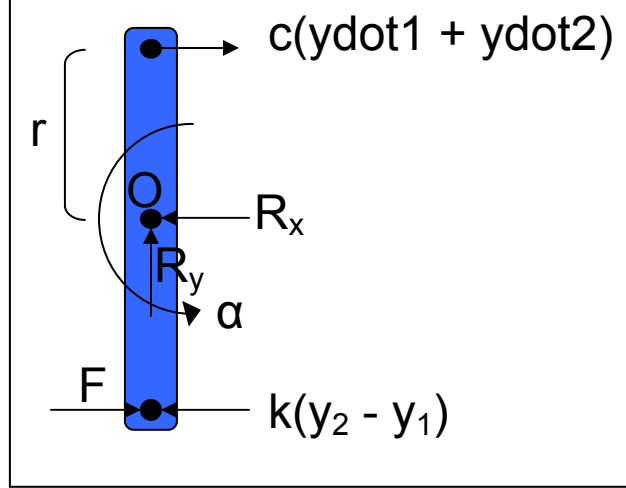
Figure 2.2: Free body diagram of the rigid body in the lumped parameter model.

Force and moment balance of each lumped mass separately leads to the equations of motion. For the base mass, the mass moment of inertia of m_2 is found as

$$J_2 = \frac{m_2(2r)^2}{12}.$$ (2.1)

Summing the moments about the pivot point O gives

$$\sum M_0 = J_2\alpha = Fr - kr(y_2 - y_1)r - cr(\dot{y}_1 + \dot{y}_2)$$ (2.2)

where angular acceleration using small angle approximation is

$$\alpha = \frac{\ddot{y}_2}{r}.$$ (2.3)

Solving for acceleration of m_2 leads to the first equation of motion

$$\ddot{y}_2 = \frac{3F}{m_2} - \frac{3k}{m_2}y_2 + \frac{3k}{m_2}y_1 - \frac{3c}{m_2}\dot{y}_1 - \frac{3c}{m_2}\dot{y}_2$$ (2.4)
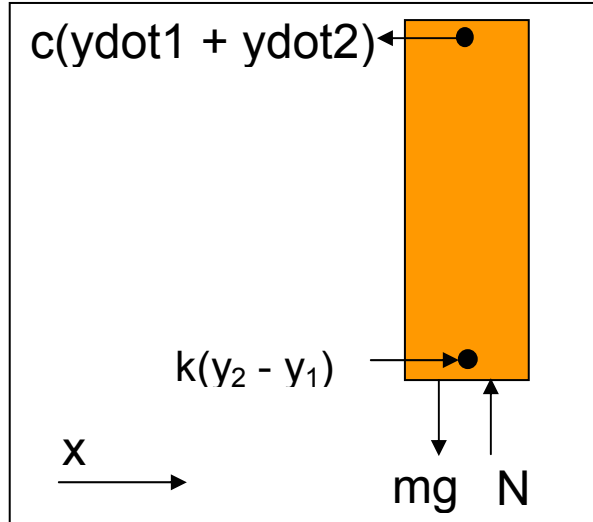
Figure 2.3: Free body diagram of tip mass in lumped parameter model.

Summing the external forces in the x direction leads to the second equation of motion

$$\ddot{y}_1 = -\frac{c}{m_1}\dot{y}_1 - \frac{c}{m_1}\dot{y}_2 + \frac{k}{m_1}y_2 - \frac{k}{m_1}y_1 . \qquad (2.5)$$

Using the state assignments

$$x_1 = y_1 \qquad (2.6)$$

$$x_2 = \dot{y}_1 \qquad (2.7)$$

$$x_3 = y_2 \qquad (2.8)$$

$$x_4 = \dot{y}_2 \qquad (2.9)$$

the two second-order differential equations for the two degree of freedom system may now be rewritten as four first order differential equations

$$\dot{\underline{x}} = \begin{bmatrix} 0 & 1 & 0 & 0 \\ -\dfrac{k}{m_1} & -\dfrac{c}{m_1} & \dfrac{k}{m_1} & -\dfrac{c}{m_1} \\ 0 & 0 & 0 & 1 \\ \dfrac{3k}{m_2} & -\dfrac{3c}{m_2} & -\dfrac{3k}{m_2} & -\dfrac{3c}{m_2} \end{bmatrix} \underline{x} + \begin{bmatrix} 0 \\ 0 \\ 0 \\ \dfrac{3}{m_2} \end{bmatrix} F . \qquad (2.10)$$

Parameters of the model used in simulations and experiments are provided in Table 2.1. The necessary parameters were determined in the following straightforward manner. Tip mass m_1 is a measured quantity from the experimental test-bed. The damping ratio of the first mode was approximated using logarithmic decrement. With empirical knowledge of the location of the first mode and its damping ratio, the stiffness k was approximated. With knowledge of the stiffness k and the damping ratio, the damping coefficient c was approximated. The non-minimum phase property of the model is indicated by the positive zero at 3.06e3.

It must be noted that the actual measured base mass m_2 is 9.6kg, yet a final value of 20kg was used for both simulations and experiments, for the reason that the tuned value of 20kg resulted in better estimates and superior performance of the closed-loop system on the experimental test-bed. To be consistent, the same value was used in simulations.

Table 2.1: Lumped parameter model parameters and modal characteristics.

	Model Data
Tip Mass (kg)	0.110
Base Mass (kg)	20
Stiffness (N/m)	131.4
Damping (N-s/m)	0.04
Resulting First Mode (Hz)	5.5
Resulting Positive Zero (Hz)	3.06e3

2.1.2 Detailed Model

Any free vibration consists of superposition of individual mode shapes. In a real system, there are an infinite number of natural frequencies and corresponding mode shapes. However, the method of assumed modes, a distributed parameter approach to modeling, employed in this work neglects high frequency modes and represents the solution in terms of a finite number of modes. Note however that the non-minimum phase characteristics of the system are retained.

The essence of the procedure is to describe the continuously variable spatial shapes of the flexible link by basis or shape functions. The time variable amplitudes of the basis functions become the state variables. The basis functions are used to construct the energy expressions which lead to inertia, stiffness and damping matrices, as well as the generalized forces from the power input.

Figure 2.4 depicts the model of the flexible link. The guided end of the link is a sliding joint allowing translation only. At this end of the link, a concentrated transverse force is applied to the link and a damper is used to represent viscous (dynamic) friction at the joint. At the free end, a lumped (particle) mass represents the payload of the flexible link. As in any modeling task, several assumptions are made to simply the analysis. The link has a uniform cross-section, consists of linear elastic material, undergoes flexure only (no axial or torsional displacement), and moves in the horizontal plane.
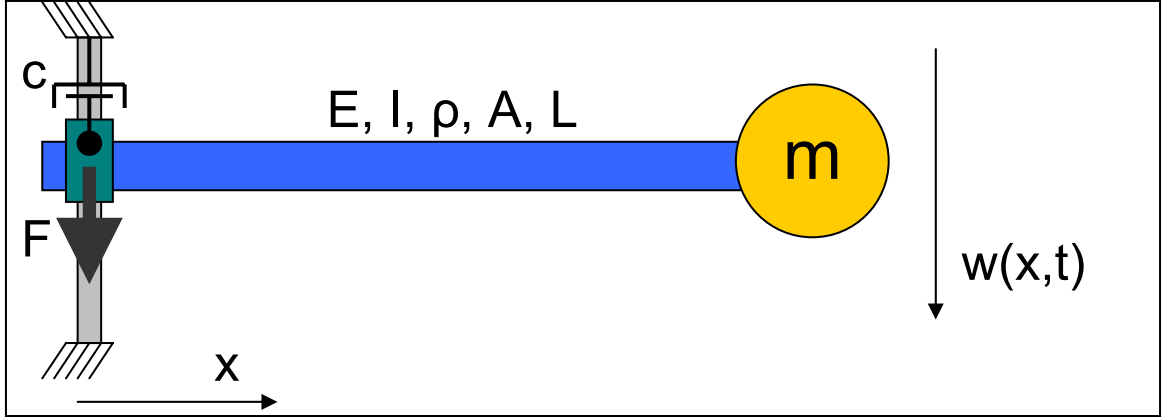
Figure 2.4: Assumed modes method model for flexible link.

To keep the order of the model manageable, only the first three flexible modes and the rigid body mode will be modeled. The four independent and continuously differentiable basis functions suggested by Ginsberg [12] are

$$\psi_1(x) = 1 \tag{2.11}$$

$$\psi_2(x) = \cos\left(\frac{\pi x}{2L}\right) \tag{2.12}$$

$$\psi_3(x) = \cos\left(\frac{\pi x}{L}\right) \tag{2.13}$$

$$\psi_4(x) = \cos\left(\frac{3\pi x}{2L}\right) \tag{2.14}$$

where x is the location along the link and L is the link length.

The distributed parameter model considers the state of displacements, forces, moments and stresses at the ends of the link, known as boundary conditions. Zero slope at the guided end is represented by the boundary condition, for i = 1 to 4,

$$\psi_i^{'}(0) = 0 . \tag{2.15}$$

Note that the last three basis functions satisfy the boundary condition above. They vanish at the location on the link where it does not deflect. Since rigid body motion is

possible for this motion system, the first basis function satisfying free-free boundary conditions for the link must be included.

The kinetic energy of the link and the lumped tip mass is

$$T = \frac{1}{2}\int_0^L \rho A \dot{w}^2 dx + \frac{1}{2}\sum m \dot{w}(x_m,t)^2 \qquad (2.16)$$

where L is the length of the link, ρ is the density, A is the cross sectional area, m is the lumped tip mass and w is displacement. The tip mass moves in unison with the link. The potential energy of the link, also known as strain energy, is found by integrating over the link length as

$$V = \frac{1}{2}\int_0^L EI \ddot{w}^2 dx \qquad (2.17)$$

where E is Young's modulus and I is the cross-sectional area moment of inertia. The power dissipated due to the viscoelastic effect and the external discrete damper is

$$P_{dis} = \int_0^L \gamma EI \left(\frac{\partial^2 \dot{w}}{\partial x^2}\right)^2 dx + \sum c(\dot{w}(x_c,t))^2 \qquad (2.18)$$

where γ is the loss factor and c is the damping coefficient of the discrete damper located at x_c. The viscoelastic effect refers to energy dissipated under deformation of a purely elastic material. Hence it is the consideration of structural damping in the model. The power input to the link by the concentrated transverse force F is

$$P_{in} = \sum F\dot{w}\left(x_F,t\right) \qquad (2.19)$$

where F is applied at location x_F.

By substituting the basis functions into the expressions for T, V, P_{dis}, and P_{in}, and evaluating the definite integrals, we eventually obtain the inertia, stiffness, damping matrices and the generalized forces. The integrals were evaluated analytically and verified by the math software Maple. Appendix X provides the procedure in further detail. The reader is referred to Ginsberg [12] for a complete overview of the procedure.

$$M = \rho AL \begin{bmatrix} 1 & \dfrac{2}{\pi} & 0 & \dfrac{-2}{3\pi} \\ \dfrac{2}{\pi} & \dfrac{1}{2} & \dfrac{2}{3\pi} & 0 \\ 0 & \dfrac{2}{3\pi} & \dfrac{1}{2} & \dfrac{6}{5\pi} \\ \dfrac{-2}{3\pi} & 0 & \dfrac{6}{5\pi} & \dfrac{1}{2} \end{bmatrix} + m \begin{bmatrix} 1 & 0 & -1 & 0 \\ 0 & 0 & 0 & 0 \\ -1 & 0 & 1 & 0 \\ 0 & 0 & 0 & 0 \end{bmatrix} \tag{2.20}$$

$$K = \dfrac{EI}{L^3} \begin{bmatrix} 0 & 0 & 0 & 0 \\ 0 & \dfrac{\pi^4}{32} & \dfrac{\pi^3}{6} & 0 \\ 0 & \dfrac{\pi^3}{6} & \dfrac{\pi^4}{2} & \dfrac{27\pi^3}{10} \\ 0 & 0 & \dfrac{27\pi^3}{10} & \dfrac{81\pi^4}{32} \end{bmatrix} \tag{2.21}$$

$$C = \gamma K + c \begin{bmatrix} 1 & 1 & 1 & 1 \\ 1 & 1 & 1 & 1 \\ 1 & 1 & 1 & 1 \\ 1 & 1 & 1 & 1 \end{bmatrix} \tag{2.22}$$

The 4x4 matrix of ones in equation 2.22 results from evaluating the trigonometric basis functions at the location of the dashpot along the beam, at x=0. The viscoelastic effect for most materials is negligible in the presence of external dashpots. The generalized forces are

$$Q = F \begin{bmatrix} 1 \\ 1 \\ 1 \\ 1 \end{bmatrix}. \tag{2.23}$$

The equations of motion are

$$M\ddot{q} + C\dot{q} + Kq = Q \tag{2.24}$$

where q are generalized coordinates, M is the inertia matrix, C is the damping matrix, K is the stiffness matrix and Q are the generalized forces. Proceeding to modal analysis, the general eigenvalue problem leads to the eigenvalues (vibration modes) and eigenvectors

(mode shapes). For obtaining free vibration modes, we only need the inertia and stiffness matrices.

Solving the general eigenvalue problem

$$\left(\underline{K} - \lambda \underline{M} \right) \underline{\phi} = \underline{0} \tag{2.25}$$

leads to the eigenvalues

$$\omega = \sqrt{\frac{EI}{\rho A L^4}} \sqrt{\lambda} . \tag{2.26}$$

In this work, Matlab was used to solve the general eigenvalue problem. The normalized eigenvectors

$$\underline{\Phi} = \frac{\underline{\phi}}{\left(\underline{\phi}^T \underline{M} \underline{\phi} \right)^{\frac{1}{2}}} \tag{2.27}$$

are used to convert the equations of motion from generalized coordinates q to modal coordinates η by decoupling the modes as

$$\underline{q} = \underline{\Phi} \underline{\eta} . \tag{2.28}$$

The decoupled equations of motion

$$\underline{\ddot{\eta}} = \underline{\Phi}^T \underline{Q} - \underline{\Phi}^T \underline{C} \underline{\Phi} \underline{\dot{\eta}} - [diag(\omega^2)] \underline{\eta} \tag{2.29}$$

may now be written in state space form.

$$\begin{bmatrix} x_1 \\ x_2 \\ x_3 \\ x_4 \\ x_5 \\ x_6 \\ x_7 \\ x_8 \end{bmatrix} = \begin{bmatrix} \eta_1 \\ \eta_2 \\ \eta_3 \\ \eta_4 \\ \dot{\eta}_1 \\ \dot{\eta}_2 \\ \dot{\eta}_3 \\ \dot{\eta}_4 \end{bmatrix} \tag{2.30}$$

$$\underline{\dot{x}} = \underline{A}\underline{x} + \underline{B}\underline{u} \tag{2.31}$$

18

The modal coordinates in conjunction with the basis functions are used to evaluate displacement at the base of the link and the acceleration at the link tip, at instants of interest.

$$\underline{y} = \begin{bmatrix} w(x=0,t) \\ \ddot{w}(x=L,t) \end{bmatrix} = \underline{\psi}(x)\underline{\Phi}\underline{\eta} = \underline{C}x + \underline{D}\underline{u} \tag{2.32}$$

To validate the model, the predicted undamped modes were compared to those predicted by a frequency domain solution or the transfer matrix method. The procedure and comparison is discussed in Appendix C. As expected, the accuracy of the highest mode predicted by the assumed modes method model is poor [12].

A special note must be made regarding the damping matrix $\underline{C}$. The decoupled equations of motion derived using modal analysis are only valid under the assumption of light damping (mode damping ratios $\ll 1$). In that case the off-diagonal terms of

$$\underline{\Phi}^T\underline{C}\underline{\Phi} \tag{2.33}$$

may be dropped. Otherwise, damped modal analysis is recommended by Ginsberg [12]. For the case at hand, the model with viscous damping at the guided end is inertially and elastically decoupled but indeed still coupled due to damping. The author found that retaining all the elements of the damping matrix $\underline{C}$ and using the proper approximation of damping coefficient c detailed in section 2.2, and using a combination of Matlab optimization of model parameters as well as trial and error manual parameter tuning resulted in a good match between experimental and modeled damped modes, as shown in Table 2.2.

The discrepancy between the actual and the modeled tip mass may be due to the rigid body tip mass (see Figure 6.1) being modeled as a point mass. The heavier model tip mass represents the increase in kinetic energy due to the rotational energy storage of the actual rigid body mass.

Table 2.2: Experimental and AMM model parameters and resulting modal characteristics.

	Experimental Data	**AMM Model Data**
Tip Mass (kg)	0.110	0.25
Length (m)	0.32	0.48
Width (m)	0.035 (1 3/8")	0.04
Thickness (m)	.003175 (1/8")	0.0024
Material	AISI 1018 Steel	Not Applicable
Density (kg/m^3)	7870	9838
Young's Modulus (GPa)	205	205
First Mode (Hz)	5.5	5.7
Second Mode (Hz)	49.5	49.0
Third Mode (Hz)	130.5	219.3

The model parameters were tuned with a goal of minimizing the error in the predicted modes. The two step procedure is as follows. Model parameter were first optimized using the 'fmincon' function in Matlab with uncertainty bounds of +/- 50% on tip mass and link length and +/- 25% on the rest. The goal of the optimization routine was to minimize squared error with error being the difference between experimental modes and modeled modes. Error in the first and second modes was weighted 100 times more than the third mode during optimization, because the highest mode predicted by an assumed modes method model is generally unreliable.

Up to this point in the model tuning procedure, damped modes (experimental) have been compared to undamped modes (model), which are the solution to the general eigenvalue problem which neglects the damping matrix. The second step is to use the $a_{tip}(s)/F(s)$ bode plot of the state space model with damping appropriately modeled and manually tune the tip mass and link length until the predicted and experimental first two modes match up well. This step is straightforward because the modeled modes are relatively close to the experimental modes already. The modes are most sensitive to changes in the tip mass and link length which makes them convenient tuning parameters for this step. The optimized model is compared to experimental data in Figure 2.5 and the root locus is plotted in Figure 2.6. Note the anomaly in the experimental data in Figure 2.5 around 17hz is the aluminum base frame in the test-bed passing through resonance. Also note the presence of three positive system zeros in the root locus.
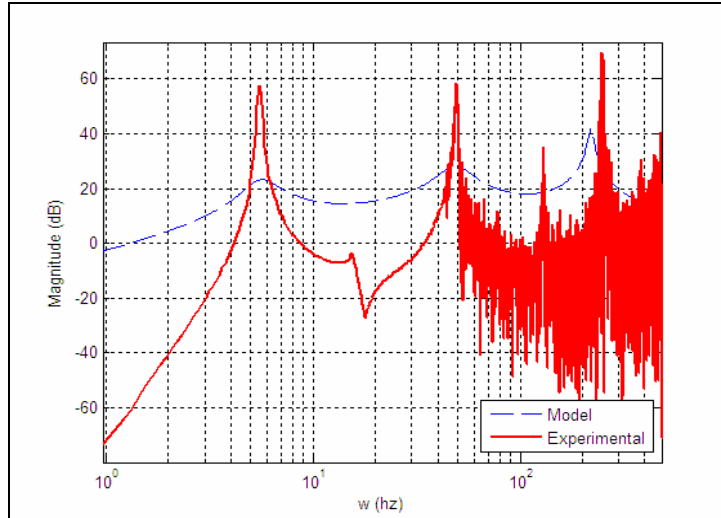
Figure 2.5: $Y_2(s)/U(s)$ magnitude vs. frequency plot of damped model as compared to experimental data.

Poles	Zeros
0	0
-6.3 +/- i34.8	0
-35.6 +/- i1.38	+/- 67.9
-53.3 +/- i302.6	+/- 45.8
-202.2	+/- 1.41
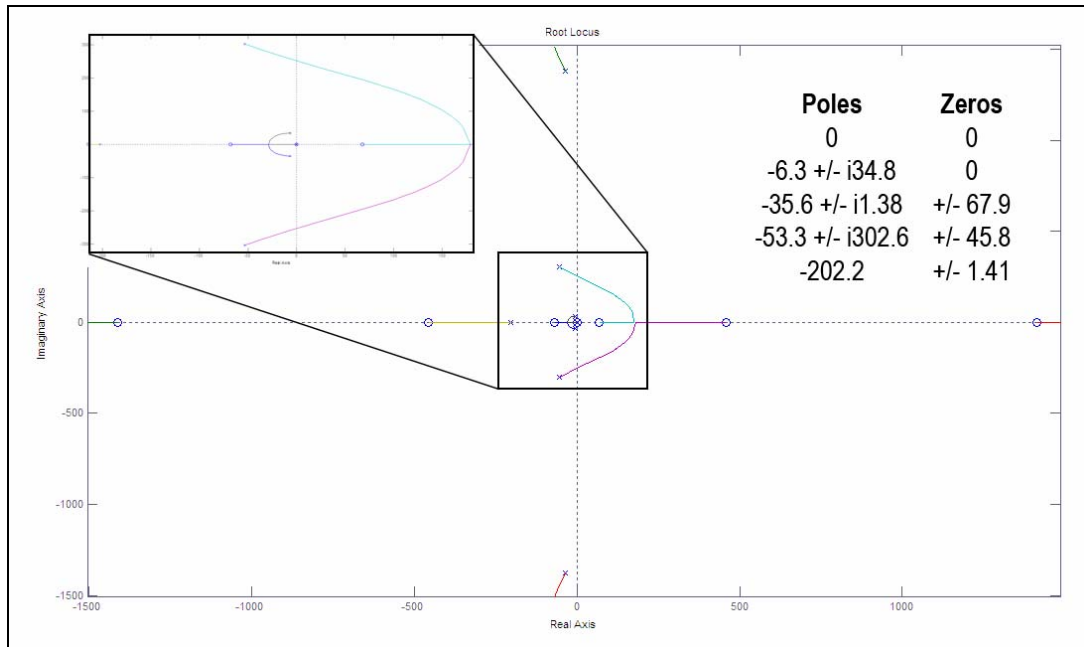
Figure 2.6: Root locus for $a_{tip}(s)/F(s)$.

22

A note must be made in regards to the overdamped modes of the optimized model apparent in Figure 2.5. The optimized model which considers the viscous damping at the sliding end of the link proved far easier to implement on the experimental test-bed. Optimized versions of the model which neglect viscous damping predict highly oscillatory motion of the sliding end of the link. Figure 2.7 depicts the modal properties of such a model. Observers implemented on the test-bed utilizing this model provided very poor estimates of the sliding end's motion. With Figures 2.5 and 2.7 in mind, the author believes further tuning of the model parameters will result in a happy medium between the modal properties predicted by the two versions.
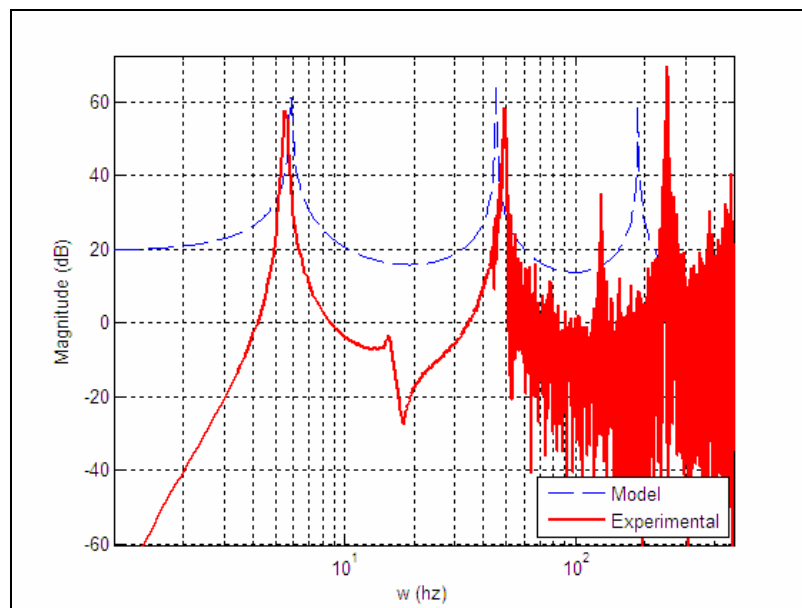
Figure 2.7: $Y_2(s)/U(s)$ magnitude vs. frequency plot of model without viscous damping as compared to experimental data.

2.2 Rigid Sub-System

The rigid subsystem in the experimental test-bed was modeled for the purpose of identifying motor gain and damping. Estimates for both parameters are needed for control purposes. Assuming a type-1 motion system, the transfer function for the rigid subsystem is

$$\frac{Y_b(s)}{V(s)} = \frac{K_m}{Ms^2 + bs} \tag{2.34}$$

where K_m is the motor gain (N/V), M is motor mass (kg), and b is viscous damping between the motor and the track (N*s/m). The Matlab function 'fmincon' was used with bounds of +/-25%, +/-10%, (0,inf) on Km, M, and b, respectively. The goal of the optimization was to minimize the sum of the squared error between experimental response and model response.

The initial guess on the motor gain is based on the average of several spring-scale measurements while a voltage from 3-6V is applied to the linear motor. The initial guess on the mass is based on direct mass measurements and the initial guess on damping is completely arbitrary. The result of the optimization based on step and ramp inputs are summarized in Table 2.3.
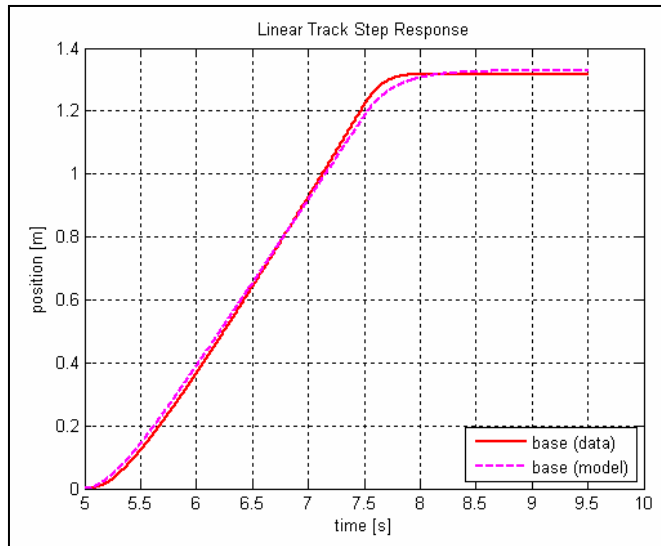
Figure 2.8: Rigid subsystem step response (3V applied from t=5 to t=7.5 sec).
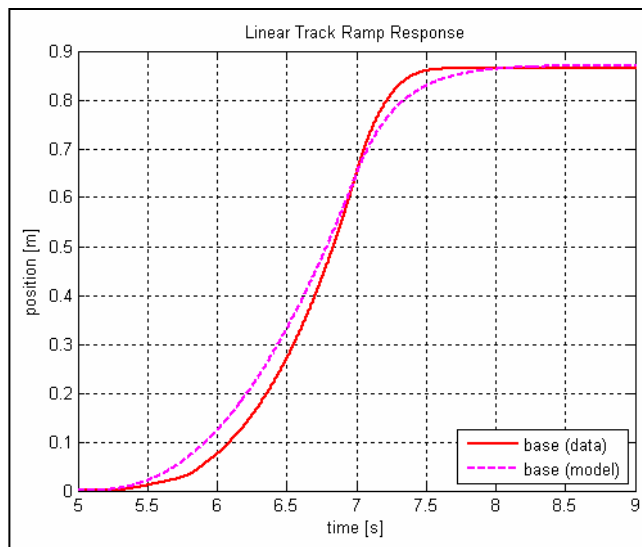
Figure 2.9: Rigid subsystem ramp response (0-5V from t=5 to t=7 sec).

25

Table 2.3: Rigid subsystem parameter identification using Matlab.

	Initial Guess	Based on Step Input	Based on Ramp Input
K_m (N/V)	8.17	6.9	6.13
M (kg)	9.6	10.52	10.56
b (N*s/m)	50	38.97	35.16

CHAPTER 3

OPTIMAL OBSERVER

For stochastic linear systems with fully known parameters, the Kalman filter is commonly employed and yields reliable estimates. Section 3.1 highlights some notable aspects of the Kalman filter and describes the manner in which the Kalman filter provides optimal estimates. The purpose of section 3.1 is to illustrate the intuitive concepts behind optimal estimation, rather than derive the filter equations. The design and subsequent integration of the Kalman filter into a closed-loop system is well known and systematic and is discussed in section 3.2. Lastly, the shortcomings of the Kalman filter in the presence of model uncertainty are highlighted in section 3.3.

3.1 Overview of Kalman Filter

Like the Luenberger observer, the Kalman filter is used when internal states are not fully measurable directly or are very costly to measure. The filter can be defined as an optimal recursive data processing algorithm [13]. The descriptor "recursive" means that the filter does not require all previous data to be kept in storage. The descriptor "optimal" will be discussed in an intuitive fashion in detail below. The filter assumes the dynamic system can be described by linear differential equations. The Kalman filter is designed to deal with the fact that sensors do not provide perfect and complete data. There is always measurement uncertainty in sensor signals due to electrical noise, distortion from sensor's internal dynamics, etc. The Kalman filter is also designed with the notion of imperfect system models in mind. However the consideration of model imperfections is limited, as will become apparent.
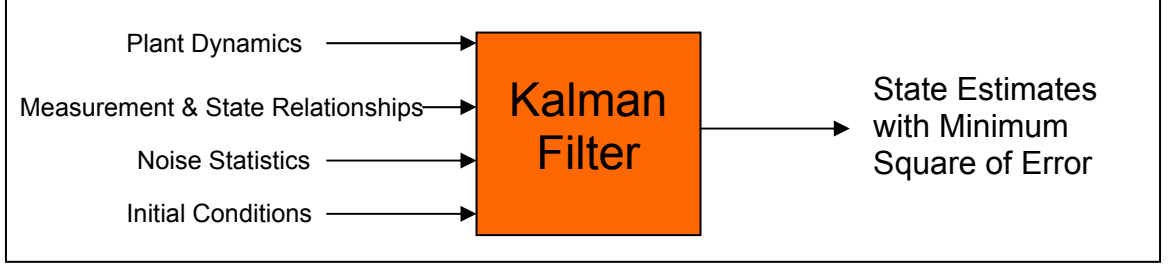
Figure 3.1: Illustrating operation of the Kalman filter.

The continuous time Kalman filter equations are as follows. Given the system model with known input $\underline{u}$,

$$\underline{\dot{x}} = \underline{A}\underline{x} + \underline{B}\underline{u} + \underline{G}\underline{w} \tag{3.1}$$

where $\underline{w}$ is white Gaussian process noise with covariance $\underline{Q}$, the measurement model given by

$$\underline{y} = \underline{C}\underline{x} + \underline{v} \tag{3.2}$$

where $\underline{v}$ is white Gaussian measurement noise with covariance $\underline{R}$, and initial conditions

$$E\left[\underline{x}(0)\right] = \underline{\hat{x}}(0) \tag{3.3}$$

and

$$E\left[(\underline{x}(0) - \underline{\hat{x}}(0))(\underline{x}(0) - \underline{\hat{x}}(0))^T\right] = P_o, \tag{3.4}$$

then the state estimate is given by

$$\underline{\dot{\hat{x}}} = \underline{A}\underline{\hat{x}} + \underline{B}\underline{u} + \underline{K}_L(\underline{y} - \underline{C}\underline{\hat{x}}), \tag{3.5}$$

where $(\underline{y} - \underline{C}\underline{\hat{x}})$ is known as the measurement innovation, the error covariance propagation is given by

$$\underline{P} = \underline{A}\underline{P} + \underline{P}\underline{A}^T + \underline{G}\underline{Q}\underline{G}^T - \underline{K}_L\underline{R}\underline{K}_L^T \tag{3.6}$$

where $\underline{P}(0) = \underline{P}_o$ and the Kalman gain $\underline{K}_L$ is given by

$$\underline{K}_L = \underline{P}\underline{C}^T\underline{R}^{-1} \tag{3.7}$$

when process and measurement noise are uncorrelated. The process noise covariance matrix $\underline{Q}$ provides a measure of uncertainty in the process and is directly tunable during design. Essentially it treats the value of a state variable as a normal distribution with some known mean and variation. Similarly the measurement noise covariance matrix $\underline{R}$ provides a measure of uncertainty in the measurements but is fixed based on sensor signal uncertainty statistics. The error covariance matrix $\underline{P}$ provides a measure of uncertainty in state estimates and depends directly on $\underline{Q}$.

The first notable aspect of the Kalman filter is that it provides optimal estimates, which means state estimates are based on the minimization of error in some respect. This is accomplished by choosing the optimum value for Kalman gain $\underline{K}_L$ which minimizes the weighted scalar sum of the diagonal elements of the error covariance matrix $\underline{P}$ defined as

$$P_k = E\left[e_k e_k^T \right] \tag{3.8}$$

where E is the expectation or mean value and e_k is the estimate error at step k. In this way, selection of the Kalman gain $\underline{K}_L$ minimizes the mean squared estimate error. It has been proven elsewhere that for a Gaussian time-varying signal, the optimal predictor is a linear predictor [14]. Another aspect of the filter's optimality is that the filter incorporates all available measurements, regardless of their uncertainty, to estimate quantities of interest. It combines data from all sensors with knowledge about system dynamics to generate the "best" estimate.

The second notable aspect of the Kalman filter is the predictor-corrector nature of the filter, incorporating knowledge of measurement and model uncertainties. Each estimate is a prediction followed by a correction. The Kalman gain $\underline{K}_L$ determines how much to weight model predictions, which are the terms

$$\underline{A}\underline{\hat{x}} + \underline{B}\underline{u} \tag{3.9}$$

in equation 3.5 and corrections, which are the terms

$$\underline{K}_L(\underline{y} - \underline{C}\hat{\underline{x}}) \tag{3.10}$$

in equation 3.5 based on fresh measurements. Intuitively, it can be seen from the Kalman gain update equation 3.7 that as uncertainty in measurements increases, the Kalman gain $\underline{K}_L$ decreases which results in weighting predictions based on the model more heavily. It can also be seen in the error covariance update equation 3.6 that in the absence of measurements, and thus in the absence of the $-\underline{K}_L\underline{R}\underline{K}_L{}^T$ term, the error covariance matrix $\underline{P}$ grows with the constant addition of uncertainty due to an imperfect model which indicates increasing uncertainty in estimates.

The third notable aspect of the Kalman filter is the stability of its estimates in the unforced case

$$\dot{\hat{\underline{x}}} = (\underline{A} - \underline{K}_L\underline{C})\hat{\underline{x}}. \tag{3.11}$$

While optimality does not guarantee stability, in practice the estimates are globally asymptotically stable even when measurements are suppressed [14]. That is, $\hat{\underline{x}}(t) \to 0$ as $t \to \infty$ for any initial condition $\hat{\underline{x}}(0)$. The formal proof for stability is documented, however it can be very restrictive and in many practical cases, the conditions are not satisfied. Some of the more difficult to meet conditions cited include complete observability and controllability. Even in such cases where the strict definition of asymptotically stability is not satisfied, the observer is in fact stable over a finite time interval of interest. The reader is referred to Gelb [14] for further discussion on stability.

The fourth notable aspect of the Kalman filter is the ability for off-line development. At steady state the error covariance matrix $\underline{P}$ becomes constant, and if the noise covariance matrices $\underline{Q}$ and $\underline{R}$, and if $\underline{A}$, $\underline{B}$ and $\underline{C}$ system matrices are already constant, the Kalman gain $\underline{K}_L$ becomes constant. The two main advantages of this steady-state Kalman filter over the recursive filter are the simplification in design and implementation and reduced computational burden. The disadvantage of such an observer is that it provides sub-optimal estimates at best, which means a loss in estimate accuracy

must be accepted. The loss of accuracy however occurs during the transient portion of estimation. In theory, at steady state, the optimal and sub-optimal predictions are identical.

3.2 Design of Kalman Filter

The state-space realization of the Kalman filter in closed-loop in the presence of process and noise uncertainties as well as parameter variation is illustrated in Figure 3.2.
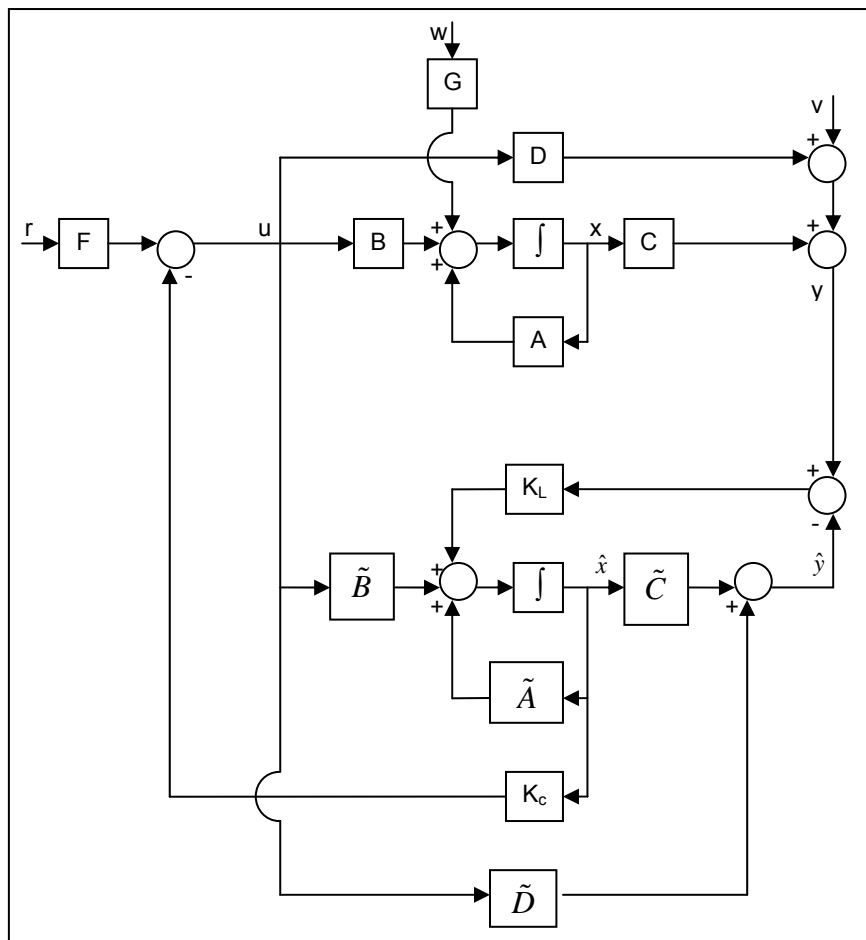
Figure 3.2: State space realization of Kalman Filter in closed-loop.

Given the system model of equation 3.1 with a measurement model

$$\underline{y} = \underline{C}\underline{x} + \underline{D}\underline{u} + \underline{v} \tag{3.12}$$

and the steady-state Kalman filter

$$\dot{\hat{\underline{x}}} = \hat{\underline{A}}\hat{\underline{x}} + \hat{\underline{B}}\underline{u} + \underline{K}_L(\underline{y} - \hat{\underline{C}}\hat{\underline{x}}) \tag{3.13}$$

with observer output equation

$$\hat{\underline{y}} = \hat{\underline{C}}\hat{\underline{x}} + \hat{\underline{D}}\underline{u} + \underline{v} \tag{3.14}$$

where estimate error

$$\underline{e} = \underline{y} - \hat{\underline{y}} \tag{3.15}$$

$$= \underline{C}\underline{x} - \hat{\underline{C}}\hat{\underline{x}} + (\underline{D} - \hat{\underline{D}})\underline{u} + \underline{v} \tag{3.16}$$

and given the control law

$$\underline{u} = \underline{F}r - \underline{K}_c\hat{\underline{x}} \tag{3.17}$$

where $\underline{F}$ is the feed-forward gain and $\underline{K}_c$ is the feed-back gain, the plant dynamics become

$$\dot{\underline{x}} = \underline{A}\underline{x} - \underline{B}\underline{K}_c\hat{\underline{x}} + \underline{B}\underline{F}r + \underline{G}w, \tag{3.18}$$

the measurement model becomes

$$\underline{y} = \underline{C}\underline{x} - \underline{D}\underline{K}_c\hat{\underline{x}} + \underline{D}\underline{F}r + \underline{v}, \tag{3.19}$$

the observer dynamics become

$$\dot{\hat{\underline{x}}} = (\hat{\underline{A}} - \hat{\underline{B}}\underline{K}_c - \underline{K}_L\hat{\underline{C}} - \underline{K}_L\underline{D}\underline{K}_c + \underline{K}_L\hat{\underline{D}}\underline{K}_c)\hat{\underline{x}} + \underline{K}_L\underline{C}\underline{x} + (\hat{\underline{B}}\underline{F} + \underline{K}_L\underline{D}\underline{F} - \underline{K}_L\hat{\underline{D}}\underline{F})r + \underline{K}_L v$$
$$\tag{3.20}$$

and the observer output equation becomes

$$\hat{\underline{y}} = (\hat{\underline{C}} - \hat{\underline{D}}\underline{K}_c)\hat{\underline{x}} + \hat{\underline{D}}\underline{F}r. \tag{3.21}$$

Combining the plant and the observer dynamics leads to

$$
\begin{bmatrix} \dot{x} \\ \dot{\hat{x}} \end{bmatrix} = \begin{bmatrix} \underline{A} & -\underline{BK}_c \\ \underline{K}_L\underline{C} & \hat{\underline{A}} - \hat{\underline{B}}\underline{K}_c - \underline{K}_L\hat{\underline{C}} - \underline{K}_L\underline{DK}_c + \underline{K}_L\hat{\underline{D}}\underline{K}_c \end{bmatrix} \begin{bmatrix} x \\ \hat{x} \end{bmatrix} + \begin{bmatrix} \underline{BF} & \underline{G} & 0 \\ \hat{\underline{B}}F + \underline{K}_L\underline{DF} - \underline{K}_L\hat{\underline{D}}F & 0 & \underline{K}_L \end{bmatrix} \begin{bmatrix} r \\ w \\ v \end{bmatrix}
$$

.

$$(3.22)$$

Combining the measurement model and the observer output equation leads to

$$
\begin{bmatrix} y \\ \hat{y} \\ u \end{bmatrix} = \begin{bmatrix} \underline{C} & -\underline{DK}_c \\ 0 & \hat{\underline{C}} - \hat{\underline{D}}\underline{K}_c \\ 0 & -\underline{K}_c \end{bmatrix} \begin{bmatrix} x \\ \hat{x} \end{bmatrix} + \begin{bmatrix} \underline{DF} & 0 & I \\ \hat{\underline{D}}F & 0 & 0 \\ \underline{F} & 0 & 0 \end{bmatrix} \begin{bmatrix} r \\ w \\ v \end{bmatrix}.
$$

$$(3.23)$$

   With the closed-loop system formulation complete, the remaining step is to find the

Kalman gain $\underline{K}_L$. Table 3.1 provides the procedure for obtaining the steady-state Kalman

gain.

Table 3.1: Determination of steady-state Kalman gain $\underline{K}_L$.

1.	Find $\underline{R}$ and $\underline{Q}$ 1a) For each measurement, find μ and σ^2 to get $\underline{R}$. 1b) Set $\underline{Q}$ small, non-zero.
2.	Find $\underline{P}$ using Matlab CARE function.
3.	Find $\underline{K}_L = \underline{P}\,\underline{C}^T\underline{R}^{-1}$ 3a) Observer poles given by eigenvalues of ($\underline{A}$-$\underline{L}\underline{C}$) where $\underline{A}$ and $\underline{C}$ are from the observer model.
4.	Tune $\underline{Q}$ as needed if estimates are poor.

3.3 Known Limitations

The main limitation of the Kalman filter, despite the fact that it is indeed based on the notion of incomplete models of real-world systems, is the sensitivity to model uncertainty. This stems from the fact that the filter formulation contains an exact system model. Variations in the observed system that occur *after* deployment of the Kalman filter severely degrade the performance and stability of the filter. This is because modeling errors are not explicitly accounted for during filter formulation but only an additive noise for the measurement and input is provided. For instance, in the observation of a second order dynamic system with a single measurement,

$$\begin{bmatrix} \dot{x}_1 \\ \dot{x}_2 \end{bmatrix} = \begin{bmatrix} x_2 \\ f \end{bmatrix} \tag{3.24}$$

where $y = x_1$, the Kalman filter in the presence of model uncertainty is given by

$$\begin{bmatrix} \dot{\hat{x}}_1 \\ \dot{\hat{x}}_2 \end{bmatrix} = \begin{bmatrix} \hat{x}_2 - K_1 \tilde{x}_1 \\ \hat{f} - K_2 \tilde{x}_1 \end{bmatrix} \tag{3.25}$$

where $\hat{f}$ indicates model uncertainty and K_1 and K_2 are observer gains. The observer error dynamics are then given by

$$\begin{bmatrix} \dot{\tilde{x}}_1 \\ \dot{\tilde{x}}_2 \end{bmatrix} = \begin{bmatrix} \tilde{x}_2 - K_1 \tilde{x}_1 \\ \Delta f - K_2 \tilde{x}_1 \end{bmatrix} \tag{3.26}$$

where $\Delta f = f - \hat{f}$. It is obvious that the term Δf due to model uncertainty has the potential to destabilize the observer error dynamics. However, the process noise covariance matrix $\underline{Q}$ does offer an opportunity to tune the filter in the presence of model uncertainty. This "tunability" feature of the Kalman filter will be investigated in this work.

CHAPTER 4

ROBUST OBSERVER

The robustness of the sliding mode observer stems from the fact that the design of the sliding mode observer is based on prior knowledge of the upper bounds on system uncertainties. System uncertainties as discussed earlier may include parametric uncertainties, unstructured uncertainties or external disturbances. The focus of this thesis work is on parametric uncertainty and thus that will be assumed to be the primary source of model uncertainty considered during observer formulation. Two distinct design approaches have been identified over the course of literature review and will be discussed separately. The outcome from either approach is an observer in which high-speed switching state functions force the observer estimate error dynamics to remain stable in the presence of perturbations due to parametric uncertainty. The nonlinear nature of the discontinuous state functions result in a nonlinear observer.

4.1 Overview of Sliding Mode Behavior

In order to develop an intuitive feel for what actually occurs in the observer dynamics during sliding mode motion, it is first necessary to have a firm grasp of commonly used terminology from Variable Structure Systems theory. The term sliding mode describes a unique behavior of a dynamic system which may be identified by a visualization of system dynamics in state space. When a dynamic system is in sliding mode, its state trajectories are confined to a sliding surface in state space. Before sliding mode motion begins, the initial behavior of the state vector as it is driven towards the sliding surface is called the reaching phase. The sliding surface is a line (in two dimensions) or a hyper plane (in higher dimensions) in state space which is designed to accommodate a sliding motion.

During sliding motion, the equations of motion of the system become the equation of the sliding surface. In the case of sliding mode observers, during sliding mode motion, the order of the observer dynamics is reduced by the number of measurements. For instance, given the sliding surface $\dot{x} + cx = 0$ for a second order system, note that its solution $x(t) = x(t_o)e^{-c(t-t_o)}$ does not depend on either plant parameters or perturbations. This so called invariance property is one promising aspect of the technique [Utkin]. The term manifold is defined as the intersection of the multiple sliding surfaces. For sliding surfaces that are planes, the manifold is a line passing through the state space origin.

Sliding mode behavior arises in systems with control as a discontinuous state function. During ideal sliding mode motion, the discontinuous state function switches infinitely fast and the state vector slides along the sliding surface rather than chatter. The signum function

$$Sgn(s) = \left\{ \begin{array}{c} 1 \\ -1 \end{array} \right\} \text{ if } \left\{ \begin{array}{c} s > 0 \\ s < 0 \end{array} \right\} \tag{4.1}$$

is typically employed for the switching control action.

4.2 General Observer Form

Given a dynamic system, with known input $\underline{u}$,

$$\underline{\dot{x}} = \underline{A}\underline{x} + \underline{B}\underline{u} + \Delta \underline{A}\underline{x}, \tag{4.2}$$

where $\Delta \underline{A}\underline{x}$ represents perturbations due to parametric uncertainty, the sliding mode observer has the structure

$$\underline{\dot{\hat{x}}} = \underline{A}\underline{\hat{x}} + \underline{B}\underline{u} + \underline{K}_L(\underline{y} - \underline{\hat{y}}) + \underline{K}_s(\text{sgn}(\underline{y} - \underline{\hat{y}})) \tag{4.3}$$

where $\underline{K}_L$ is the Kalman gain and $\underline{K}_s$ is the sliding mode gain. It is interesting to note that in the presence of Gaussian white measurement or process noise, the sliding mode observer consists of the Kalman filter (or Luenberger observer in the case of a

deterministic linear system) plus the additional discontinuous state functions. Slotine [6] describes the Kalman filter terms in the observer equation as the source of damping in state estimate trajectories while the discontinuous terms handle any perturbations due to parametric uncertainties. A notable aspect of this particular observer design is that the two parts of the observer are designed separately.

As an illustration of the interplay between the two gain matrices and parametric uncertainty, in the observation of an unforced second order dynamic system with a single measurement,

$$\begin{bmatrix} \dot{x}_1 \\ \dot{x}_2 \end{bmatrix} = \begin{bmatrix} x_2 \\ f \end{bmatrix} \tag{4.4}$$

where $y = x_1$, the error dynamics of the sliding mode observer in the presence of parametric uncertainty are given by

$$\begin{bmatrix} \dot{\tilde{x}}_1 \\ \dot{\tilde{x}}_2 \end{bmatrix} = \begin{bmatrix} \tilde{x}_2 - L_1\tilde{x}_1 - k_1\,\mathrm{sgn}(\tilde{x}_1) \\ \Delta f - L_2\tilde{x}_1 - k_2\,\mathrm{sgn}(\tilde{x}_1) \end{bmatrix} \tag{4.5}$$

where Δf indicates parametric uncertainty, L_1 and L_2 are Kalman filter gains assuring asymptotic stability of estimate error, and k_1 and k_2 are the sliding mode gains which are designed to deal with the uncertainty. It should be noted that given exact knowledge of plant parameters in an idealized world, addition of the sliding mode terms to the observer provide no direct benefit.

It is already clear how Kalman filter gains are selected. The question now is how to select the sliding mode gains. The Kalman filter gains are selected independent of the sliding mode observer gains but the later gains are based on the Kalman filter gains. Thus the sliding mode gains are influenced by the dynamics of the Kalman filter. The design repercussions of this will become apparent. Two design approaches have been identified. Section 4.2 discusses the variable structure systems theory approach applied by Slotine

[6] and Chalhoub [7]. Section 4.3 discusses the Lyapunov approach applied by Wallcott and Zak [15], Elbeheiry et al [10], Zaki et al [11] and Kim and Inman [9].

4.3 Variable Structure Systems Theory Approach

In the variable structure systems theory approach, the design of the sliding surface and the sliding condition are explicitly addressed. The general approach is to first design one sliding surface per measurement. Second, design a sliding condition to reach the sliding surface in finite time. Third, design the observer gains to satisfy the sliding condition. The meaning of sliding condition will become clearer in section 4.3.1.

4.3.1 Observer Design

For a sliding mode observer, we are concerned with the sliding mode behavior that occurs not in state space but in error space, where error is the difference between actual and estimated states, as depicted in Figure 4.1. Thus the problem of estimation has been reduced to that of remaining on the surface for all $t > 0$. The observer is said to be in sliding mode once the discontinuous state function becomes infinitely fast which means estimate errors have reached zero. In practice, if estimate error reaches zero, the condition is flagged and the discontinuous terms are set to zero.
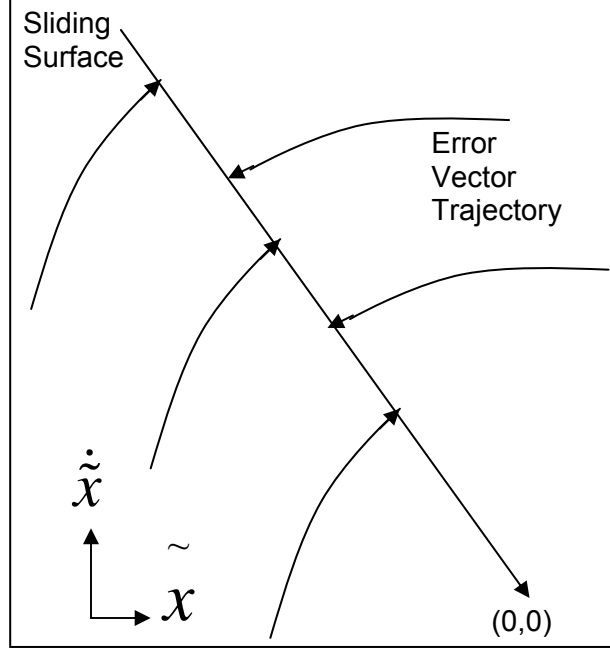
Figure 4.1: Sliding mode behavior in error space for a sliding mode observer.

The number of sliding surfaces corresponds to the number of measurements. All the sliding surfaces pass through the origin of the state space. Essentially, states slide along one sliding surface until the state vector meets another surface. It then begins sliding along the intersection of the two surfaces, always tending towards the state space origin.

Slotine [6] proposes the design of an observer for general nonlinear systems. His approach has been adapted here for linear systems. Given the observer structure

$$\dot{\hat{\underline{x}}} = \underline{\hat{A}}\underline{\hat{x}} - \underline{K}_L(\underline{\hat{y}} - \underline{y}) - \underline{K}_s(\text{sgn}(\underline{\hat{y}} - \underline{y})) \tag{4.6}$$

where $\underline{\hat{x}} \in R^n$, $\underline{\hat{A}}$ is our model of $\underline{A}$, $\underline{K}_L$ and $\underline{K}_s$ are n x p Kalman and sliding mode gain matrices, respectively, where p is the number of measurements, and

$$\underline{\hat{y}} - \underline{y} = \underline{c}_i\underline{\hat{x}} - y_i \tag{4.7}$$

where $\underline{c}_i$ is the ith row of the p x n $\underline{C}$ matrix, then the sliding surfaces are defined as

$$\underline{s} := \underline{\hat{y}} - \underline{y} = \underline{C}(\underline{\hat{x}} - \underline{x}) . \tag{4.8}$$

A sliding surface thus corresponds to an estimate error. The p dimensional surface $\underline{s} = 0$ is attractive and sliding will occur in the vicinity of the sliding surface if

$$\frac{1}{2}\frac{d}{dt}s_i^2 \le -\eta|s_i| \tag{4.9}$$

or written alternatively,

$$s_i\dot{s}_i \le -\eta|s_i| \ , \ i = 1...p \tag{4.10}$$

where η is a design parameter. The condition implies the squared distance to the surface as measured by s_i^2 decreases along all system trajectories. In other words, at all times when the estimate error is not zero, satisfying the condition above means the error vector trajectory is pointed towards the sliding surface in error space and thus towards the origin of the error space. This is referred to as the sliding condition.

During sliding mode motion, the order of the system dynamics are effectively reduced by n – p. According to Slotine, the approximate dynamics of this reduced order system can be formally derived using the equivalent control method posed by Utkin [6]. For the state estimation problem, Slotine gives the equivalent dynamics of the reduced order error dynamics of the observer when in sliding mode motion as

$$\dot{\underline{x}} = (\underline{I} - \underline{K}_s(\underline{C}\underline{K}_s)^{-1}\underline{C})\Delta\underline{f} \tag{4.11}$$

where $\Delta\underline{f} = \hat{\underline{A}} - \underline{A}$. Given knowledge of the upper bound on uncertainty, the sliding mode gain $\underline{K}_s$ can thus be designed to ensure stable observer error dynamics with perturbation explicitly accounted for. Essentially the problem of non-linear observer design has become a linear pole placement problem. The n – p poles of the homogeneous part of equation 4.11 can be placed arbitrarily to be critically damped (negative real parts only) by selection of the elements of $\underline{K}$.

To find $\underline{K}_s$ for a given problem at hand, Chalhoub et al [7] generate constraint equations by evaluating the sliding condition in equation 4.10 and the reduced order observer error dynamics in equation 4.11. The number of constraint equations generated

by the sliding condition depends on the number of sliding surfaces, or number of measurements. The number of constraint equations generated by equation 4.11 is largely influenced by the measurement matrix $\underline{C}$. The difficulty encountered in generating the constraint equations for the later step is discussed next in section 4.3.2.

4.3.2 Limitations of Design Approach

The first drawback of this approach is that once the constraint equations for the sliding mode gain $\underline{K}_s$ have been generated, bounds on a number of unknown quantities have to arbitrarily selected. To illustrate the ad-hoc nature of the arbitrary pole placement problem, an example is useful. Given the lumped parameter model by equation 2.10,

$$\underline{\dot{x}} = \begin{bmatrix} x_2 \\ f_2(x_1, x_2, x_3, x_4) \\ x_4 \\ f_4(x_1, x_2, x_3, x_4, u) \end{bmatrix} \tag{4.12}$$

with a single measurement, the flexible link tip position, given by

$$\underline{y} = \begin{bmatrix} 1 & 0 & 0 & 0 \end{bmatrix} \underline{x}, \tag{4.13}$$

then the sliding surface is given by

$$s = \hat{x}_1 - x_1. \tag{4.14}$$

The goal is to find the sliding mode gain

$$\underline{K}_s = \begin{bmatrix} k_{11} \\ k_{21} \\ k_{31} \\ k_{41} \end{bmatrix}. \tag{4.15)}$$

The rate of change of estimate error is given by

$$\dot{s}_1 = \tilde{x}_2 - K_{11}\tilde{x}_1 - k_{11} \operatorname{sgn}(\tilde{x}_1), \tag{4.16}$$

where K_{11} is a Kalman gain and k_{11} is a sliding mode gain. The complete steps are detailed in Appendix E. Evaluating the sliding condition in equation 4.10 for the single sliding surface results in a single constraint equation on k_{11} given by

41

$$k_{11} \geq \eta + \frac{\tilde{x}_2}{\text{sgn}(\tilde{x}_1)} - K_{11}|\tilde{x}_1|, \tag{4.17}$$

where η is a user defined parameter and K_{11} is a Kalman gain. To generate more constraint equations on $\underline{K}$, the reduced order observer error dynamics in equation 4.11 are evaluated and give

$$\underline{\dot{\tilde{x}}} = \begin{bmatrix} 0 & 0 & 0 & 0 \\ 0 & -\dfrac{k_{21}}{k_{11}} & 0 & 0 \\ 0 & -\dfrac{k_{31}}{k_{11}} & 0 & 1 \\ 0 & -\dfrac{k_{41}}{k_{11}} & 0 & 0 \end{bmatrix} \begin{bmatrix} \tilde{x}_1 \\ \tilde{x}_2 \\ \tilde{x}_3 \\ \tilde{x}_4 \end{bmatrix} + \begin{bmatrix} 0 & 0 \\ 1 & 0 \\ 0 & 0 \\ 0 & 1 \end{bmatrix} \begin{bmatrix} \Delta f_2 \\ \Delta f_4 \end{bmatrix}, \tag{4.18}$$

where Δf_2 and Δf_4 are perturbations due to parameter uncertainty. Again, the complete steps are detailed in Appendix E. Given the upper bounds on the perturbations, the objective is to select k_{21}, k_{31} and k_{41} to ensure asymptotically stable dynamics of the homogeneous part of equation 4.18 while explicitly accounting for the two perturbation terms. When each row of the observer error dynamics in equation 4.18 is expanded, the following three constraint equations result:

$$k_{21} = k_{11} \frac{\Delta f_2}{\tilde{x}_2} \tag{4.19}$$

$$k_{31} = k_{11} \frac{\tilde{x}_4}{\tilde{x}_2} \tag{4.20}$$

$$k_{41} = k_{11} \frac{\Delta f_4}{\tilde{x}_2}. \tag{4.21}$$

The first limitation of the approach now becomes clear. Upper bounds must be selected not only on the perturbation terms Δf_2 and Δf_4 but also $\tilde{x}_2$ and $\tilde{x}_4$. As the order of system model increases, so does the amount of "guesstimation" on estimate errors. The

author has yet to find published work proposing a systematic approach for determining these upper bounds, to in some sense ensure an optimal solution for $\underline{K}_s$.

Second, as the number of measurements increases and the more populated or "dense" the $\underline{C}$ matrix becomes, the more "guesstimation" on estimate error bounds becomes necessary. To elaborate on this point, it can be shown that for the lumped parameter model of equation 4.12 with two measurements leads to an 8x2 sliding mode gain $\underline{K}_s$. There are eight unknowns to determine yet it can be shown that only four constraint equations can be generated in total; two from the two sliding surfaces via equation 4.10 and two from evaluation of the reduced order observer error dynamics via equation 4.11. One technique employed by Chalhoub et al [7] is to set off-diagonal terms in the homogenous part to zero, in the resulting differential equation from equation 4.11. This is since only the diagonal terms of the homogenous part are necessary to ensure an asymptotically stable response. For example, in equation 4.18, only k_{11} and k_{21} really matter. The author found that for simple cases such as the lumped parameter model, the pole placement problem is manageable as long as the measurements are direct state outputs resulting in a simple $\underline{C}$ matrix.

Applying the variable structure systems theory design approach to the assumed mode methods model of equations 2.30, 2.31 and 2.32 becomes vary tedious and the technique employed by Chalhoub of setting off-diagonal terms to zero does not suffice. Given the measurement model of equation 2.32 with the two measurements being flexible link sliding end position and free end acceleration, the $\underline{C}$ matrix takes the form

$$\underline{C} = \begin{bmatrix} C_{11} & C_{12} & C_{13} & C_{14} & 0 & 0 & 0 & 0 \\ C_{21} & C_{22} & C_{23} & C_{24} & C_{25} & C_{26} & C_{27} & C_{28} \end{bmatrix}. \tag{4.22}$$

The "dense" nature of the $\underline{C}$ matrix is because the states in the assumed modes method model are generalized coordinates which must be transformed into meaningful quantities of interest by the $\underline{C}$ matrix. Evaluation of equation 4.11 this time results in a

"dense" homogenous part and the resulting pole placement problem becomes very tedious by hand.

The third limitation worthy of mentioning is that the gains depend on the time varying measurement $\tilde{x}_1$ and $\mathrm{sgn}(\tilde{x}_1)$. A time varying $\underline{K}_s$ will lead to a higher computational burden for real-time control application.

4.4 Lyapunov Approach

The alternative to the design approach just discussed is the Lyapunov approach. The attractive aspect of this approach is that the sliding mode gain $\underline{K}_s$ is determined as a whole, not one element individually at a time. Nor does not this approach require the designer to select bounds on state estimate errors. Perhaps for these reasons, the Lyapunov approach was found to be more common in published work reviewed by the author.

4.4.1 Observer Design

Walcott and Zak [15] propose an observer design which solves the Lyapunov matrix equation to find the sliding mode gain $\underline{K}_s$. Consider the dynamic system defined in section 4.1 with known input $\underline{u}$ and parametric uncertainties represented by $\Delta \underline{A} \underline{x}$,

$$\dot{\underline{x}} = \underline{A}\underline{x} + \underline{B}\underline{u} + \Delta \underline{A}\underline{x}, \tag{4.2}$$

and the observer structure as defined earlier in section 4.1,

$$\dot{\hat{\underline{x}}} = \underline{A}\hat{\underline{x}} + \underline{B}\underline{u} + \underline{K}_L(\underline{y} - \hat{\underline{y}}) + \underline{K}_s(\mathrm{sgn}(\underline{y} - \hat{\underline{y}})). \tag{4.3}$$

First consider the unforced case

$$\dot{\underline{x}} = \underline{A}\underline{x} + \Delta \underline{A}\underline{x}. \tag{4.23}$$

Taking the estimate error as $\hat{\underline{x}} - \underline{x}$ results in the observer error dynamics

$$\dot{\tilde{\underline{x}}} = (\underline{A} - \underline{K}_L\underline{C})\tilde{\underline{x}} + \underline{K}_s(\mathrm{sgn}(\underline{y} - \hat{\underline{y}})) - \Delta \underline{A}\underline{x}, \tag{4.24}$$

where $\underline{K}_L$ is the Kalman gain, $\underline{K}_s$ is the sliding mode gain and $\Delta \underline{A} x$ represents parametric uncertainties. The goal is now to design $\underline{K}_s$ such that the discontinuous state function $\underline{K}(\text{sgn}(\underline{y} - \hat{\underline{y}}))$ overpowers the parametric uncertainties $\Delta \underline{A} x$ assuring stable observer error dynamics.

Walcott and Zak show that the following implementation of $\underline{K}_s$ meets the observer design objectives:

$$\underline{K}_s = \rho \underline{P}^{-1} \underline{C}^T , \qquad (4.25)$$

where ρ is a user selected positive scalar, $\underline{P}$ is the unique, positive definite solution to the Lyapunov matrix equation

$$(\underline{A} - \underline{K}_L \underline{C})\underline{P} + \underline{P}(\underline{A} - \underline{K}_L \underline{C})^T = -\underline{Q}_p \qquad (4.26)$$

and $\underline{C}$ is the output matrix.

First it needs to be shown how exactly the perturbations due to parametric uncertainties are handled in the observer error dynamics in equation 4.24. The observer error dynamics are rewritten as

$$\dot{\tilde{x}} = (\underline{A} - \underline{K}_L \underline{C})\tilde{x} + \rho \underline{P}^{-1} \underline{C}^T (\text{sgn}(\underline{y} - \hat{\underline{y}})) - \underline{P}^{-1} \underline{C}^T \underline{\xi} , \qquad (4.27)$$

where

$$\underline{\xi} = (\underline{P}^{-1} \underline{C}^T)^{-1}(\Delta \underline{A} x) . \qquad (4.28)$$

Since the term $\underline{P}^{-1} \underline{C}^T$ appears in both the discontinuous state function term and the parametric uncertainty term, it can effectively be canceled out. Two observations can now be made. First, as long as

$$\rho \geq \|\underline{\xi}\| , \qquad (4.29)$$

which says the Euclidean norm of the vector representing perturbations is bounded by the (user selected) scalar ρ , then the perturbations due to parametric uncertainties are overpowered by ρ. Second, the term $\text{sgn}(\underline{y} - \hat{\underline{y}})$ provides the correct direction of action

by the discontinuous state function. The result is $\lim_{t\to\infty}\tilde{x}=0$ or in other words, asymptotically stable observer error dynamics.

4.4.2 Observer Stability

The proof of asymptotic stability is provided by Walcott and Zak [15] and is reproduced here for reference. Consider the following positive definite Lyapunov function candidate

$$V(e) = e^T P e \qquad (4.30)$$

where $e = \hat{x} - x$ and $\underline{P}$ is the unique, positive definite solution to the Lyapunov matrix equation. Then the time derivative of this Lyapunov function candidate is given by

$$\dot{V}(e) = e^T(A_o^T P + PA_o)e - 2\frac{e^T P(P^{-1}C^T Ce)}{\|Ce\|}\rho - 2e^T PP^{-1}C^T \xi \qquad (4.31)$$

where $A_o = A - LC$ and ξ represents model uncertainties and disturbances. Also note that $\frac{Ce}{\|Ce\|}$ is interchangeable with $\text{sgn}(\hat{\underline{y}} - \underline{y})$. Equation 4.31 can be simplified to

$$\dot{V}(e) = -e^T Q_p e - 2\|Ce\|\rho - 2e^T C^T \xi . \qquad (4.32)$$

Taking the Euclidean norm of the last term of 4.32 and noting $\rho \geq \|\underline{\xi}\|$ yields

$$\dot{V}(e) \leq -e^T Q_p e - 2\|Ce\|\rho + 2\|Ce\|\xi . \qquad (4.33)$$

Thus $\dot{V}(e) < 0$ and it has been shown that $\lim_{t\to\infty}\tilde{x}=0$.

4.4.3 Boundary Layer Observer

The shortcoming of the discontinuous state function is that the term leads to the undesirable phenomena of chattering. To assure the estimates converge to some arbitrarily small neighborhood of the true states, Walcott and Zak [15] suggest use of a boundary layer. Use of a boundary layer produces a continuous and smooth switching

46

control action. A simplified version of the boundary layer proposed by Walcott and Zak employed in this work takes the form

$$S = \begin{cases} \rho \underline{P}^{-1}\underline{C}^{T}\, \mathrm{sgn}(\underline{y}-\hat{\underline{y}}) & \text{if } \left\| \underline{y}-\hat{\underline{y}} \right\| > \lambda \\ \rho \underline{P}^{-1}\underline{C}^{T}\, \dfrac{\underline{y}-\hat{\underline{y}}}{\lambda} & \left\| \underline{y}-\hat{\underline{y}} \right\| \le \lambda \end{cases} \tag{4.34}$$

where S is the discontinuous state function in the sliding mode observer equation 4.3. Here λ is the width of the boundary layer. Outside of the boundary layer, the usual discontinuous state function is used. Within the boundary layer, the formerly-discontinuous station function is now proportional to the estimate error. Note that when the width of the boundary layer is zero, then the boundary layer observer becomes the original sliding mode observer. Also note that as estimate error tends to zero, the formerly-discontinuous state function tends to zero which is not true of the non-boundary layer sliding mode observer.

The proof of boundary layer observer error dynamic stability using Lyapunov functions as in the earlier case is provided by Walcott and Zak, in a similar fashion as earlier. The interested reader is referred to the direct source.

4.4.4 Limitations of Design Approach

At least one author has cited the difficulty under certain circumstances in solving the matrix Lyapunov equation [10]. Sliding mode observers based on high gain Luenberger observers and for high-order systems is one combination which has been shown to pose a challenge. Typically the Lyapunov equation is satisfied by selecting a positive-definite symmetric $\underline{Q}_p$ which leads to a unique positive-definite symmetric $\underline{P}$. While it is not advised, the Lyapunov equation can be solved in reverse by selecting a $\underline{P}$ first and finding a $\underline{Q}_p$ which satisfies the equation. The solution in this reverse approach is not always conclusive. Having said that, it should be noted that the author of this work

was able to use the Lyapunov matrix equation solvers provided in the software Matlab and LabVIEW and obtained solutions for both the fourth order and eight order models.

Another difficulty is in placing the upper bounds on time varying uncertainty. Observer design calls for selecting a $\rho \geq \left\| \underline{\xi} \right\|$, however $\underline{\xi}$ depends on a time varying $\Delta \underline{A} \underline{x}$. It is not clear how bounds on the state vector are placed. The approach to be tried, at least in a simulation, is to monitor the state vector and record the largest value over the simulation period. The success of this highly iterative approach depends entirely on the assumption that not only is the state vector bounded, but that these bounds are tight. It is apparent from equation 4.25 that an excessively large ρ will amplify $\underline{K}_s$ which in turn which will make observation very unstable. The alternative may be to pick ρ by a trial-and-error approach without directly determining $\underline{\xi}$.

CHAPTER 5

SIMULATIONS

Simulations are a means to analyze the performance of the optimal observer and the robust observer by analyzing their dynamic behavior as well as that of the closed-loop system with each observer in place. Simulations are also a means to provide insight on the effect of each observer parameter. Simulation studies are conducted using the Simulation Module in National Instruments LabVIEW 8.5.

5.1 Study Overview

As noted earlier, a notable aspect of the sliding mode observer under consideration is that it consists of a Kalman filter part and an additional discontinuous state function part. The two parts of the observer are designed separately. A block diagram for the complete system to be simulated is provided in Figure 5.1.

The sliding mode observer simulated consists of two design parameters. Observer design parameters Q_p (which determines $\underline{K}$) and ρ are defined in Chapter 4. Both boundary layer and non-boundary layer versions of the sliding mode observer are simulated. For the non-boundary layer version, ε is simply $\mathrm{sgn}(\underline{y} - \hat{\underline{y}})$.

For the boundary layer version of the observer, ε is

$$\begin{cases} \rho \underline{P}^{-1} \underline{C}^T \mathrm{sgn}(\underline{y} - \hat{\underline{y}}) & \text{if } \begin{array}{l} \left\| \underline{y} - \hat{\underline{y}} \right\| > \lambda \\ \left\| \underline{y} - \hat{\underline{y}} \right\| \leq \lambda \end{array} \end{cases} \qquad (5.1)$$
$$\rho \underline{P}^{-1} \underline{C}^T \dfrac{\underline{y} - \hat{\underline{y}}}{\lambda}$$

where λ is an additional observer design parameter, the boundary layer thickness.

Figure 5.1: State space realization of system for simulation studies.

In simulations, the Kalman gain $\underline{K}_L$ is determined based on the noise covariance matrices

$$\underline{R} = \begin{bmatrix} R_{11} & 0 \\ 0 & R_{22} \end{bmatrix} \tag{5.2}$$

and

$$\underline{Q} = Q_t \begin{bmatrix} 1 & 0 & 0 & 0 \\ 0 & 1 & 0 & 0 \\ 0 & 0 & 1 & 0 \\ 0 & 0 & 0 & 1 \end{bmatrix}. \tag{5.3}$$

Unless otherwise noted, the values of the elements of the covariance matrices reflect those in Table 5.1.

Table 5.1: Noise covariance data for Kalman filter simulations.

R_{11}	3.87e-10
R_{22}	2.59e-4
Q_t	3e-4

All three values are inherited from the experimental test-bed to be discussed in Chapter 6. Covariance of R_{11} reflects a standard deviation of 1.97e-5 meters in the position measurement. Covariance of R_{22} corresponds to a standard deviation of 0.0161 m/s^2 in the acceleration measurement. Covariance of Q_t is based on manual fine tuning of the Kalman filter to provide the best possible estimates on the experimental test-bed.

The feedback gain K_{cl}, based on the method of symmetric root locus, reflects a value of 1.25e6 for τ for all simulations, unless otherwise noted. Appendix A provides the procedure for design of the symmetric root locus. A control input of less than 60N was achieved for all simulations. 61.7N is an approximation for the saturation of the actuator on the experimental test-bed, given a motor gain of 6.17 N/V and maximum control voltage of 10V.

5.2 Performance Study

There are two lumped parameter models simulated in this portion of the study. The only difference between the two models is the output matrix $\underline{C}$. The first model assumes that the outputs are states, with measurements of base position (x_3) and tip position (x_1). *Henceforth, this model will be referred to as the TP model.* The second model assumes a measurement of base position and tip acceleration. *Henceforth, this model will be referred to as the TA model.* The purpose of simulating both models is to compare the effects of the different $\underline{C}$ matrix structures on observer performance.

What variables are changed in the study? In the performance study, the tip mass is the independent variable changed and the first mode is a dependent variable of interest. The other independent variables varied are sliding mode observer parameters ρ, $\underline{Q}_p$, and λ. With parameter variation of 1%, 10%, 30%, and 60%, the observer and controller

51

underestimate the flexibility of the link and overestimate the speed of response. At -1%, -
-10%, -30% and -60%, the opposite is true.

Note that the sliding mode observer parameter Q_p is an arbitrary positive-definite
symmetric matrix. For convenience, Q_p is assumed to have repeated roots. The parameter
will be referred to simply as a scalar Q_p.

Table 5.2: Parameter variation in lumped parameter models during simulation.

Parameter Variation (P.V.) in Tip Mass m_1 (%)	Resulting First Mode (Hz)
0	5.5
60	4.35
30	4.82
10	5.24
-10	5.8
-30	6.57
-60	8.7

How is performance judged in the study? The performance criteria for the
observers is mean squared estimate error of position estimates and velocity estimates,
reported separately. For lumped parameter models, position mean square estimate error is
defined as the norm of the vector

$$\begin{bmatrix} MSE(x_1) \\ MSE(x_3) \end{bmatrix} \tag{5.4}$$

where MSE(x$_1$) and MSE(x$_3$) are the mean square estimate errors of each state estimate
taken over the length of the simulation. Recall x_1 is the tip position and x_3 is the base
position in the simple model.

Similarly, the velocity mean square estimate error for the simple model is defined
as the norm of the vector

$$\begin{bmatrix} MSE(x_2) \\ MSE(x_4) \end{bmatrix}. \qquad\qquad (5.5)$$

Recall x_2 is the tip velocity and x_4 is the base velocity in the simple model.

5.2.1 Without Measurement Noise

For the Kalman filter, fictitious process noise is useful for improving filter estimates when we can't update the filter dynamic model directly. Although a value for process noise covariance Q_t is inherited from the experimental setup, a robustness study of the Kalman filter with Q_t as the varied parameter was undertaken. As Figure 5.2 depicts, the process noise variance Q_t directly determines the robustness of the Kalman filter. The study shows that weighing the measurements much more than the model predictions serves us well in case of limited parameter variation. However, with increasing parameter variation, weighing the measurements too heavily actually produces more estimate error. This is since larger Q_t leads to larger Kalman gain $\underline{K}_L$. In presence of high uncertainty, the larger gain amplifies estimate errors. The lesson is to increase Q_t in moderation. $Q_t = 3e\text{-}4$ is the most robust out of the choices and is used for the rest of the simulations.
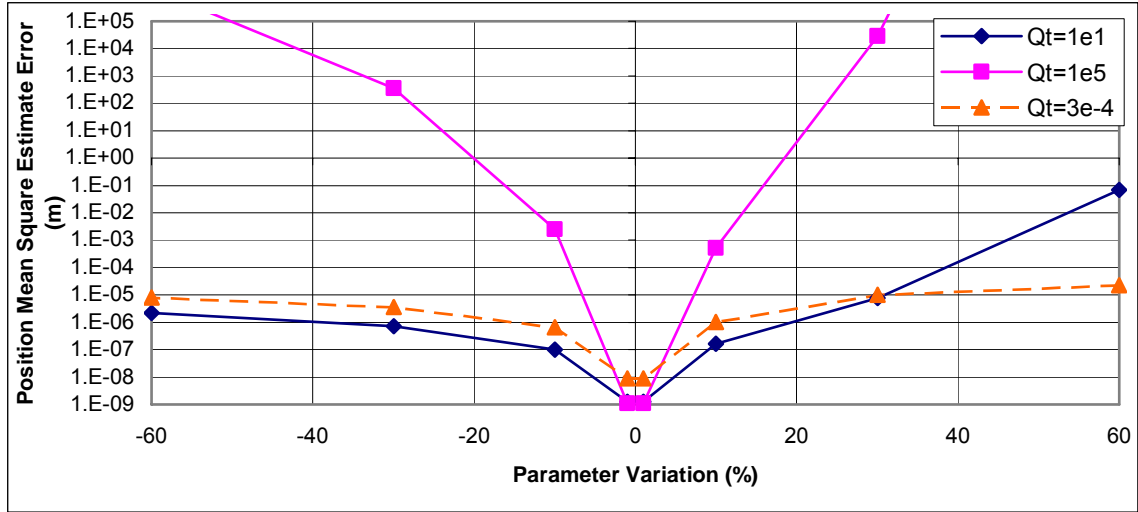
Figure 5.2: Robustness of Kalman filter alone, based on position state estimates of TA model. The figure showcases the "tunability" of the Kalman filter, with regards to robustness, by varying the process noise covariance matrix during filter formulation.

The next series of figures compares the state estimates provided by the boundary layer sliding mode observer (BLSMO) and the Kalman filter (KF) in the presence of 30% parameter variation. In most cases, BLSMO estimates are superior.
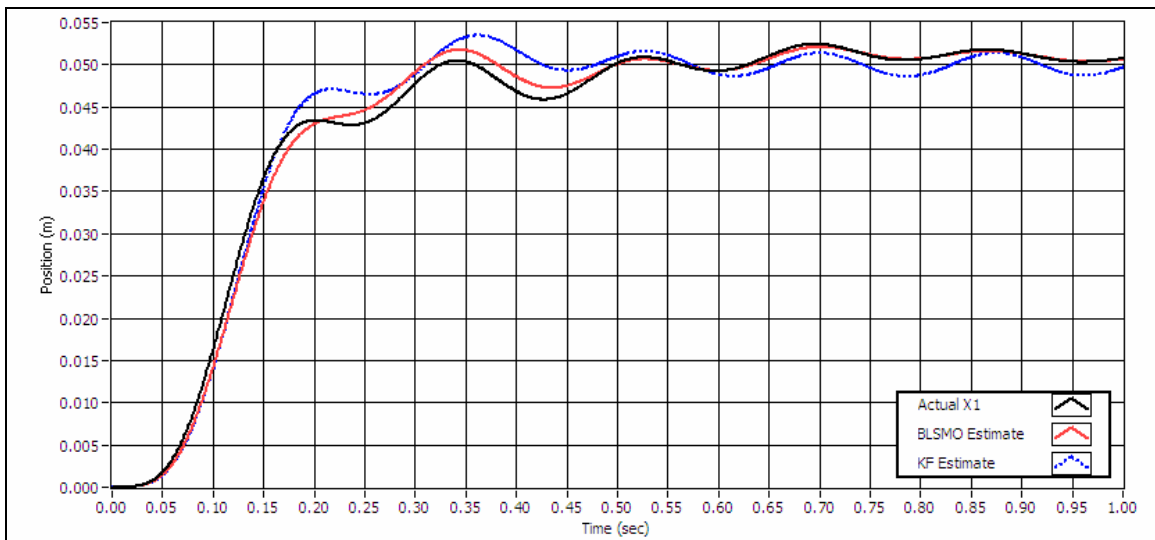
Figure 5.3: X_1 estimate comparison between boundary layer sliding mode observer (Q_p = 2.2e3, ρ = 2.5, λ = 150) and the Kalman filter (Q_t = 3e-4), based on TA model with 30% P.V. The figure highlights the reduced error estimates produced by the BLSMO under parameter uncertainty.
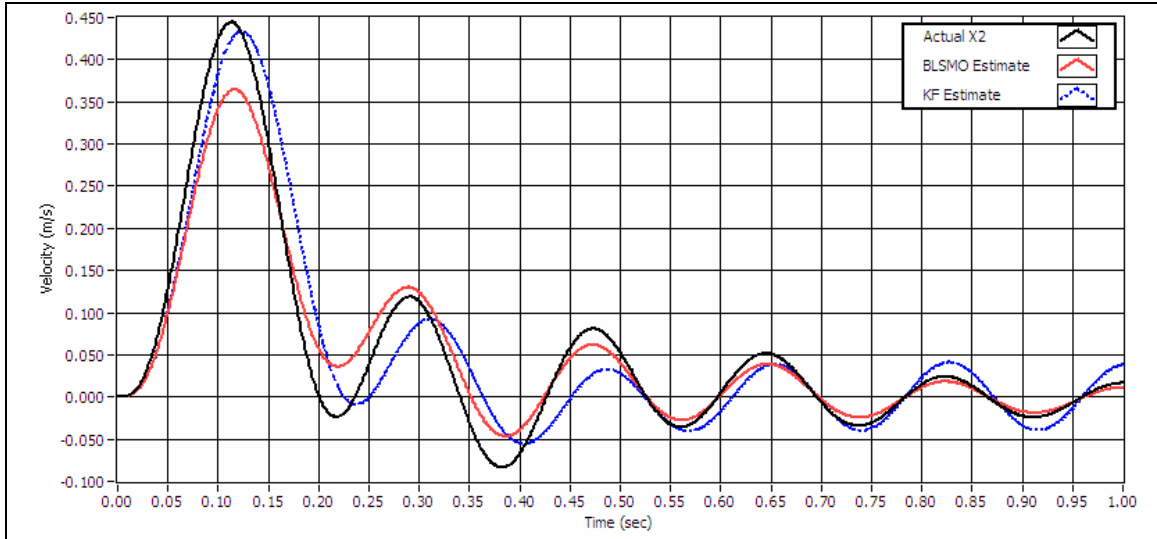
Figure 5.4: X_2 estimate comparison between boundary layer sliding mode observer (Q_p = 2.2e3, ρ = 2.5, λ = 150) and the Kalman filter (Q_t = 3e-4), based on TA model with 30% P.V. The figure highlights the reduced error estimates produced by the BLSMO under parameter uncertainty.
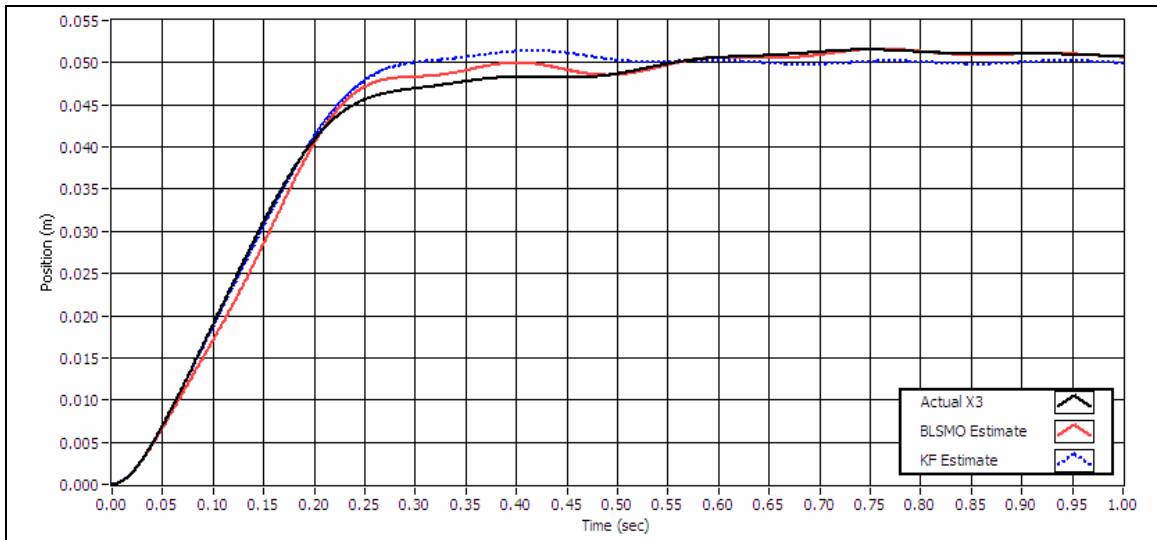
Figure 5.5: X_3 estimate comparison between boundary layer sliding mode observer (Q_p = 2.2e3, ρ = 2.5, λ = 150) and the Kalman filter (Q_t = 3e-4), based on TA model with 30% P.V. The figure highlights the reduced error estimates produced by the BLSMO under parameter uncertainty.
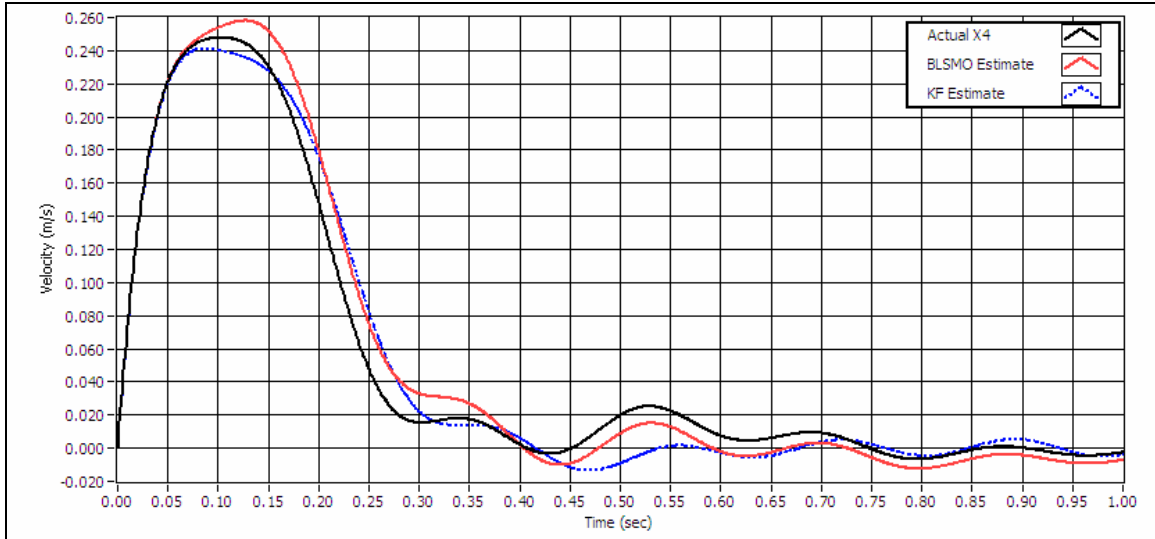
Figure 5.6: X_4 estimate comparison between boundary layer sliding mode observer (Q_p = 2.2e3, ρ = 2.5, λ = 150) and the Kalman filter (Q_t = 3e-4), based on TA model with 30% P.V. The figure highlights the fact that certain state estimate errors may not be reduced by use of the BLSMO.

Figure 5.7 provides an illustration of the error state trajectory chattering about the sliding surface and approaching the origin of error space. Recall that chatter is not an indication of sliding mode behavior. True sliding mode behavior is an idealization, representing an infinitely fast discontinuous state function which means estimate errors have reached zero. Figure 5.8 depicts the same error state trajectory but now under the influence of a boundary layer of thickness 0.005.
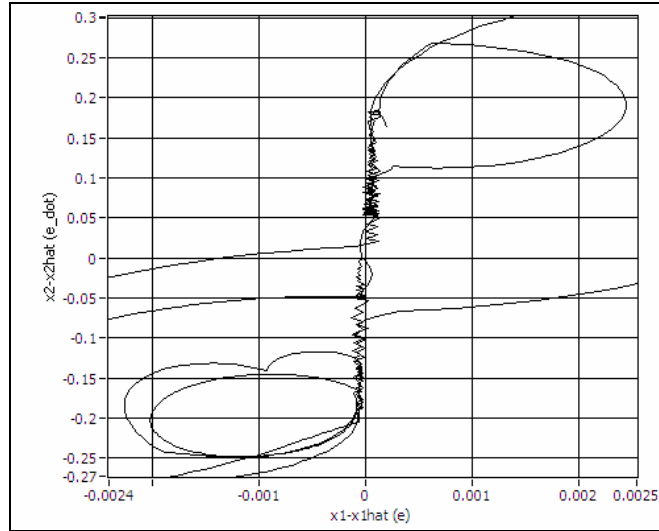
Figure 5.7: Sliding mode behavior in error space for a sliding mode observer ($Q_p = 4$, $\rho = 1$), based on TP model with 45% P.V. The figure illustrates the use of a phase-plane plot to detect sliding mode behavior.
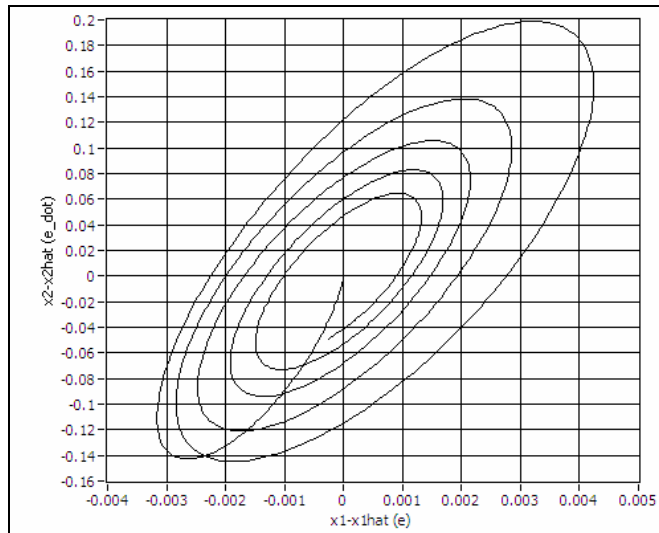
Figure 5.8: Error vector trajectory in error space of a boundary layer sliding mode observer ($Q_p = 4$, $\rho = 1$, $\lambda = 0.005$), based on TP model with 45% P.V. The figure illustrates how traditional sliding mode behavior in error space is overridden by use of a BLSMO.

The Kalman gain $\underline{K}_L$ and the sliding mode gain $\underline{K}_s$ used in the simulation of the TP model with 45% parameter variation are provided in Table 5.3. Note that ρ is a multiplier on $\underline{K}_s$, and thus the total affect of the discontinuous state function on the observer dynamics should not be judged solely on $\underline{K}_s$.

Table 5.3: Kalman gain ($\underline{K}_L$) and Sliding mode gain ($\underline{K}_s$) for TP model with 45% P.V.

$\underline{K}_L$		$\underline{K}_s$	
15.95	3.2e-5	-6.3e-2	1.8e-2
136.9	1.9e-4	-2.0e-3	5.6e-5
16.15	2.4e-5	8.198	-6.3e-2
130.4	1.8e4	-6.7e-3	2.6e-3

The next series of figures compare the performance of the Kalman filter, various sliding mode observers (SMO) and various boundary layer counterparts (BLSMO). A log scale is used for the y-axis in the plots because of the high variability in performance. Both the tip acceleration output model and the tip position output models are used to illustrate the fact that results are similar for both models. The various SMO/BLSMO designs were determined at different parameter variation levels. The best SMO/BLSMO designs at +/- 10% P.V., +/-30% P.V., and +/-60% P.V. are compared in these studies.
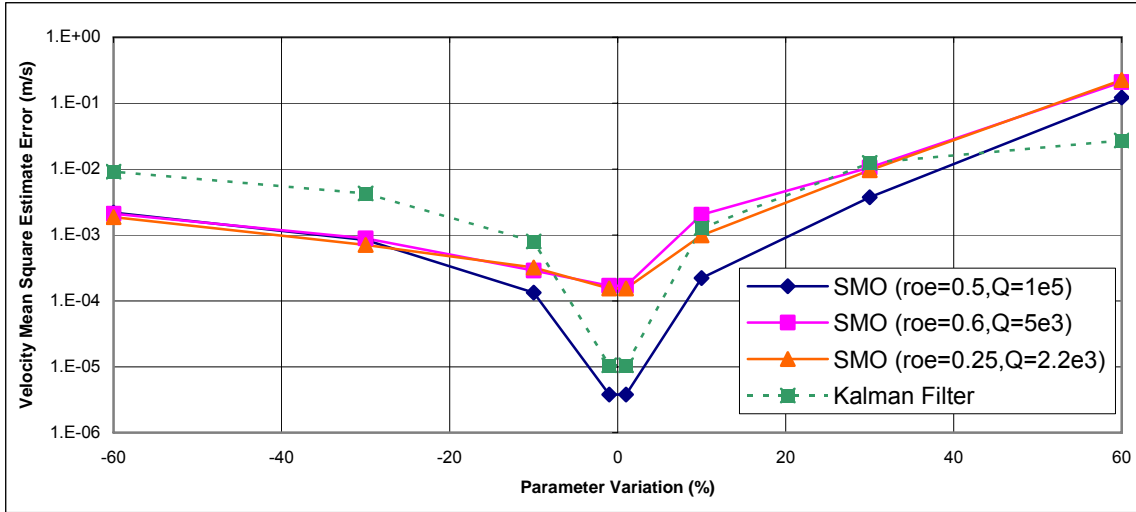
Figure 5.9: Comparison of the robustness to P.V. of various sliding mode observers with the Kalman filter, based on velocity state estimates of TA model. The figure highlights the reduced estimate errors produced by the SMO under parameter uncertainty, in most cases.
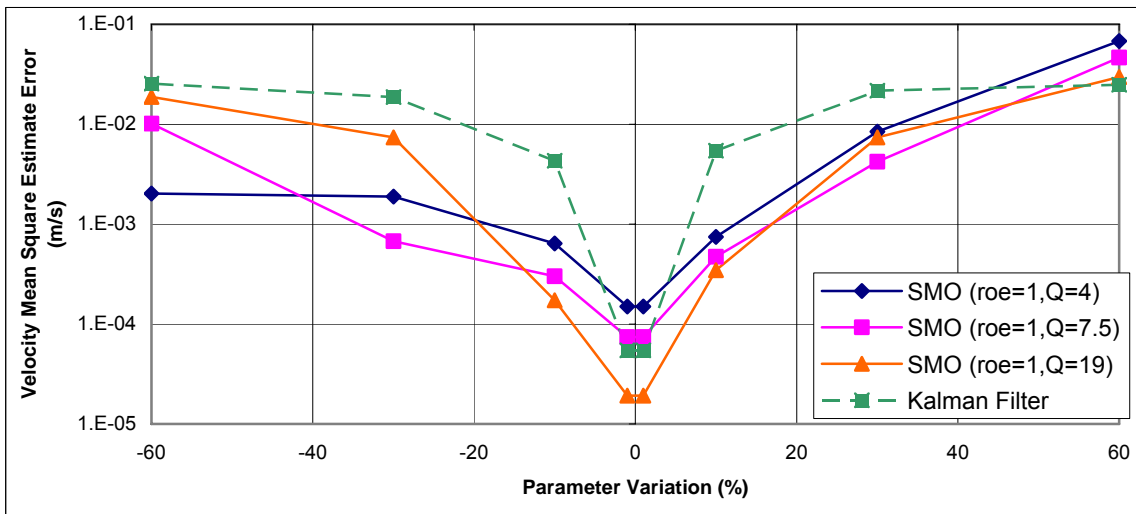
Figure 5.10: Comparison of the robustness to P.V. of various sliding mode observers with the Kalman filter, based on velocity state estimates of TP model. The figure highlights the reduced estimate errors produced by the SMO under parameter uncertainty, in most cases.
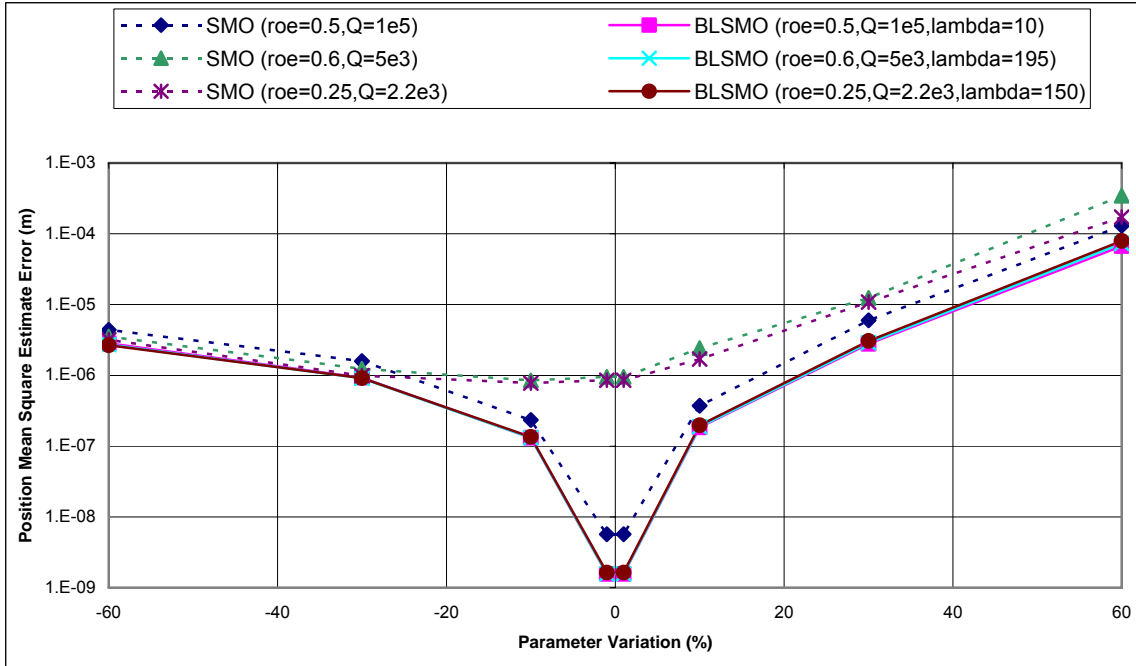
Figure 5.11: Comparison of the robustness to P.V. of various sliding mode observers with their boundary layer counterparts, based on position state estimates of TA model. The figure highlights the superiority of the BLSMO to the SMO under parameter uncertainty, via further reduction of estimate errors produced.
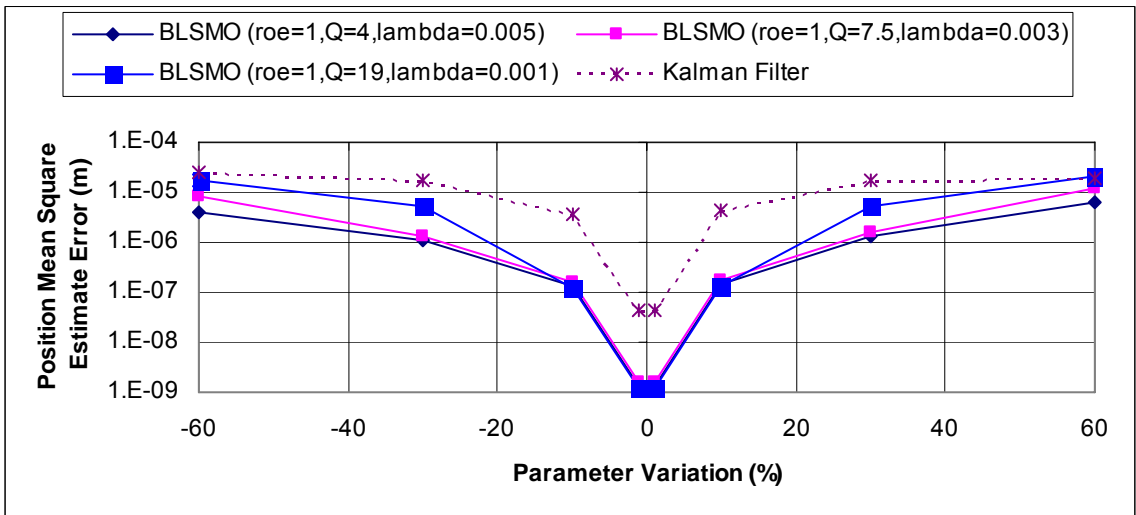
Figure 5.12: Comparison of the robustness to P.V. of various boundary layer sliding mode observers with the Kalman filter, based on position state estimates of TP model. The figure highlights the reduced estimate errors produced by the BLSMO under parameter uncertainty, in most cases.

One observation from the simulations thus far is that while the estimate errors produced by various SMO designs can vary significantly at a given uncertainty level, in general the estimate errors are lower than those produced by the Kalman filter alone. Another observation is that the variation in estimate errors in the case of various BLSMO designs is quite low. In general, the performance of various BLSMO designs converge which should make it far easier to determine optimum BLSMO parameters. It is apparent that the boundary layer has a large effect on the observer. Figures 5.13 and 5.14 depict the effect of the boundary layer on the discontinuous state function.
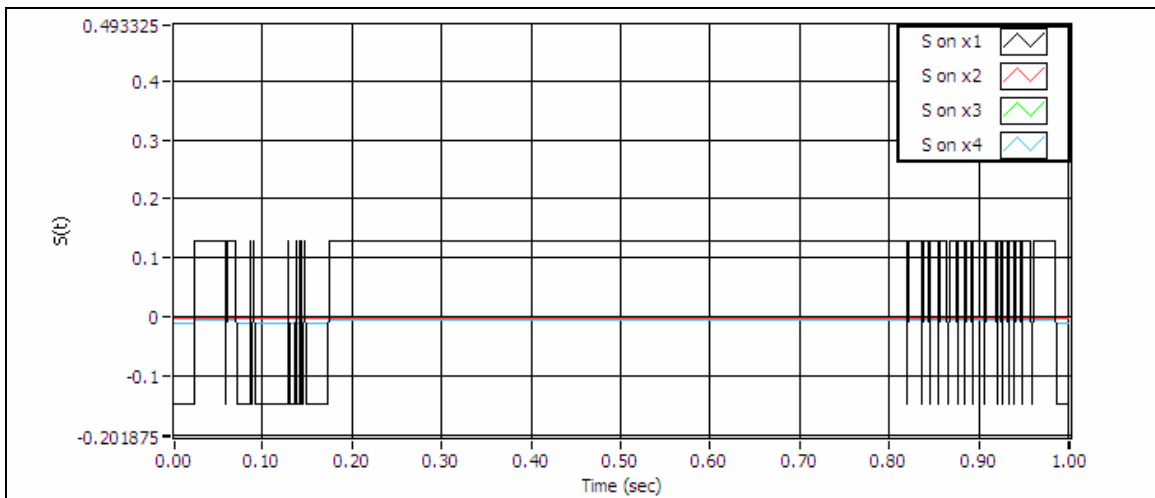
Figure 5.13: Discontinuous state function produced by a sliding mode observer ($Q_p = 4$, $\rho = 1$) based on TP model. The figure illustrates the discontinuous control action injected into the observer dynamics by the sliding mode observer.
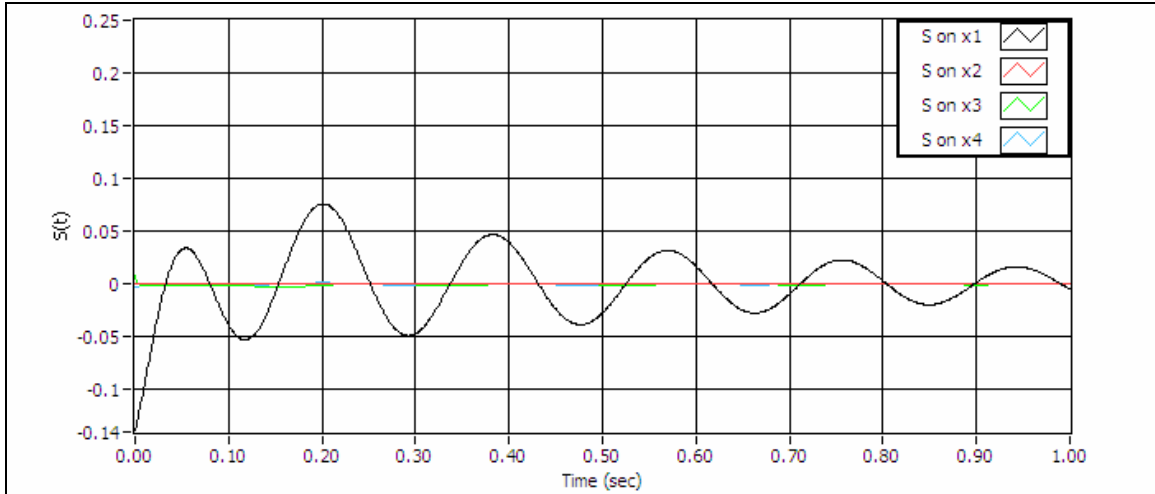
Figure 5.14: Continuous state function produced by a boundary layer sliding mode observer (Q_p = 4, ρ = 1, λ = 0.005) based on TP model. The figure illustrates the smoothed control action injected into the observer dynamics by the boundary layer sliding mode observer.

As boundary layer thickness approaches zero, a BLSMO becomes a SMO. As the thickness is increased, BLSMO estimate errors increase as the state function S(t) becomes smoother. Thus a boundary layer can be detrimental to the performance of the observer. An optimal thickness does exist and is an instance when BLSMO estimates are more accurate than their SMO counterparts.
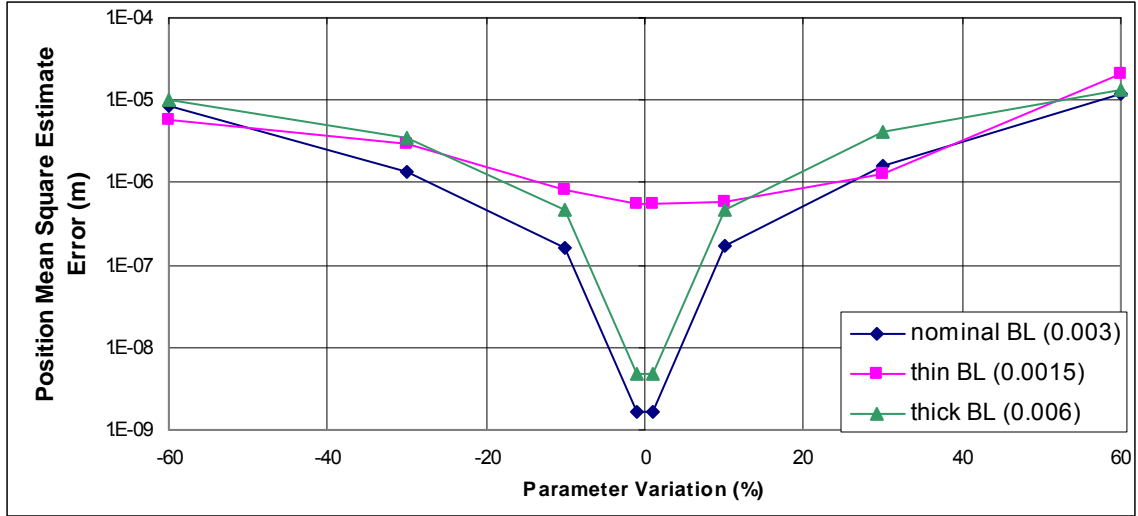
Figure 5.15: Effects of various boundary layer thicknesses on observer robustness to P.V., based on TP model. The figure emphasizes the necessity of using an optimal value of boundary layer thickness in the boundary layer sliding mode observer.

5.2.2 With Measurement Noise

In this portion of the study, in addition to the existing independent variables tip mass m_1, boundary layer sliding mode observer parameters Q_p, ρ, and λ, the Gaussian white noise measurement noise levels are varied. The two additional independent variables are R_{11} and R_{22}, measurement noise covariances.

Table 5.4: Standard deviation of measurements in lumped parameter TA and TP models for simulations with noise.

	Position Measurement σ (m)	Acceleration Measurement σ (m/s^2)
Low Noise	1.97e-5	0.0161
Medium Noise	1.97e-4	0.161
High Noise	1.97e-3	1.61

63
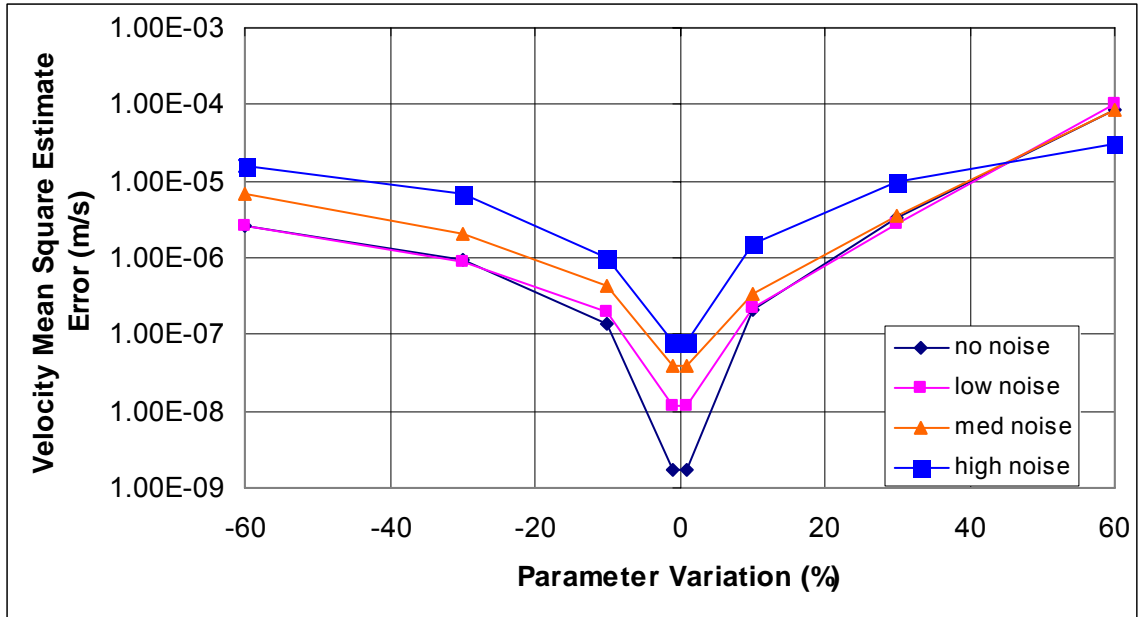
Figure 5.16: Effects of various measurement noise levels on observer (Q_p = 2.2e3, ρ = 0.01, λ = 5) robustness to P.V., based on TA model. The figure illustrates the degrading performance of the BLSMO in presence of Gaussian white measurement noise.
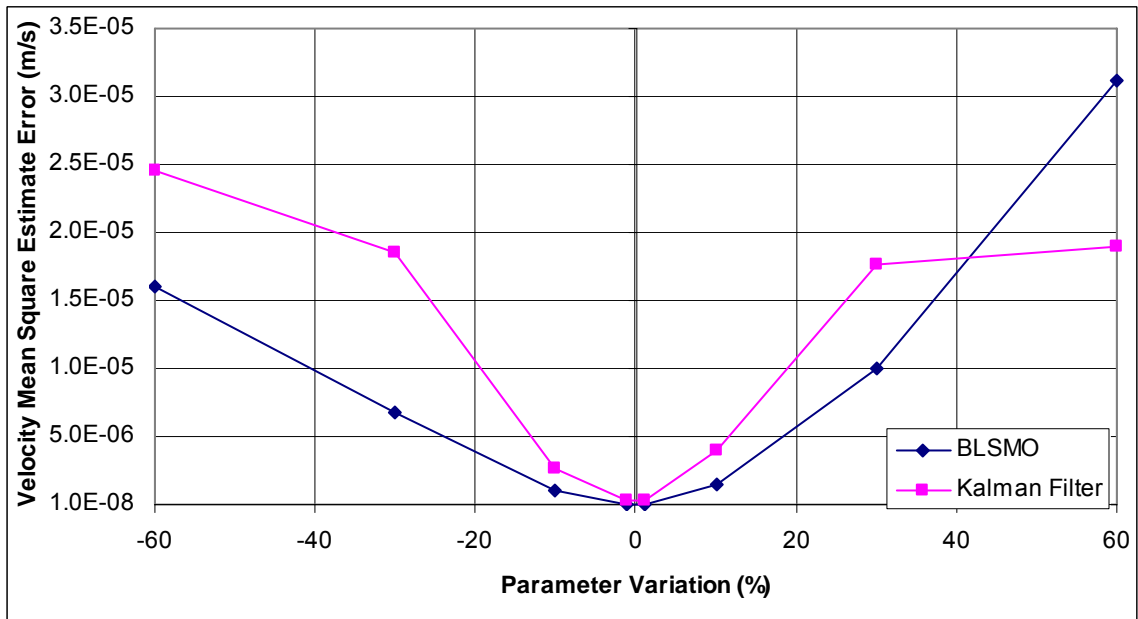
Figure 5.17: Comparison of boundary layer sliding mode observer (Q_p = 2.2e3, ρ = 0.01, λ = 5) to Kalman filter in presence of Gaussian white measurement noise, based on TA model. The figure illustrates the degraded performance of the BLSMO in presence of Gaussian white measurement noise is still higher than that of the Kalman filter.

5.3 Stability Study

A lumped parameter model with different parameters had to be employed for stability studies because the existing models are inherently very stable. Setting tip mass m_1 to ten times larger than base mass m_2 led to a model more suitable for stability studies. The asymptotic and marginal stability of the tip acceleration output of such a model was much more easily manipulated. As a further change, now k and m_1 are varied, allowing for more drastic parameter variation. The outputs of this modified inertia lumped parameter model are base position and tip acceleration.
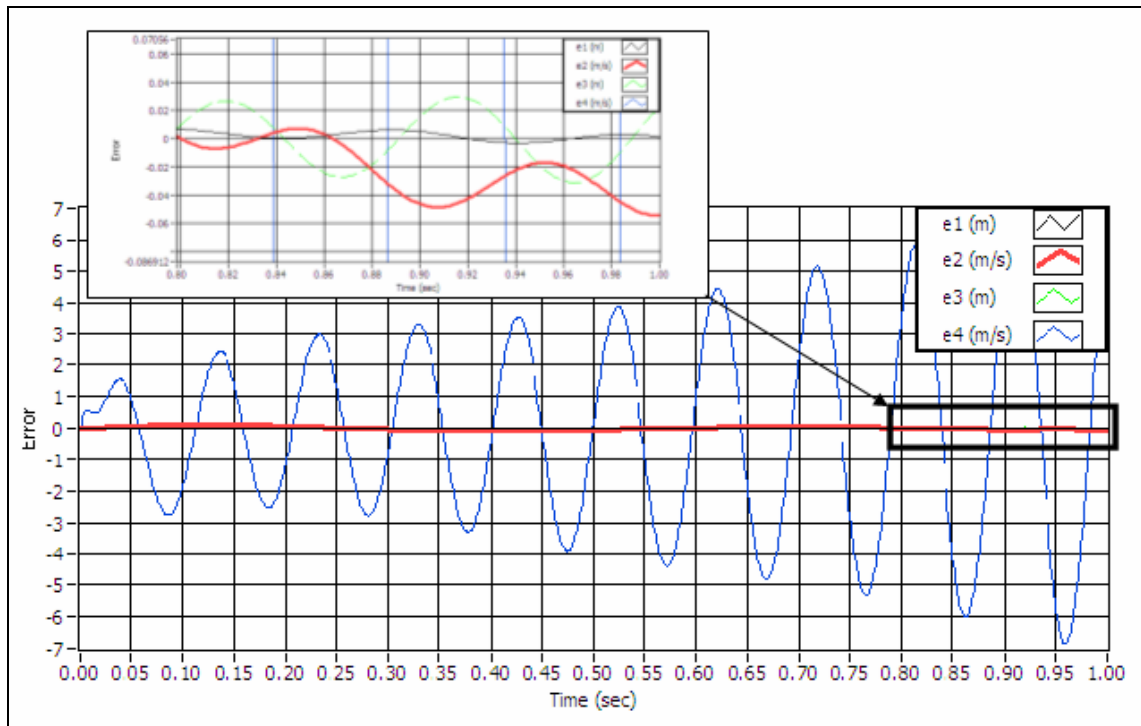
Figure 5.18: Estimate errors with Kalman filter in presence of 25% parameter variation, based on the modified inertia TA model. The figure depicts the unstable error dynamics of the Kalman filter in presence of large parameter variation.
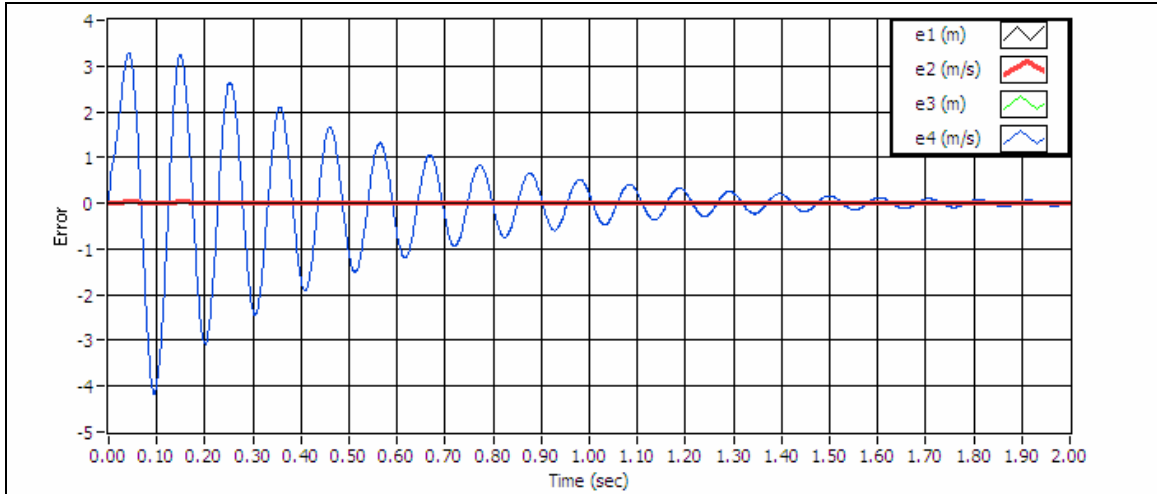
Figure 5.19: Estimate errors with boundary layer sliding mode observer (Q_p = 3.65e6, ρ = 60, λ = 1) in presence of 25% parameter variation, based on the modified inertia TA model. The figure depicts stable error dynamics of the BLSMO under the same conditions in which the Kalman filter error dynamics are unstable.
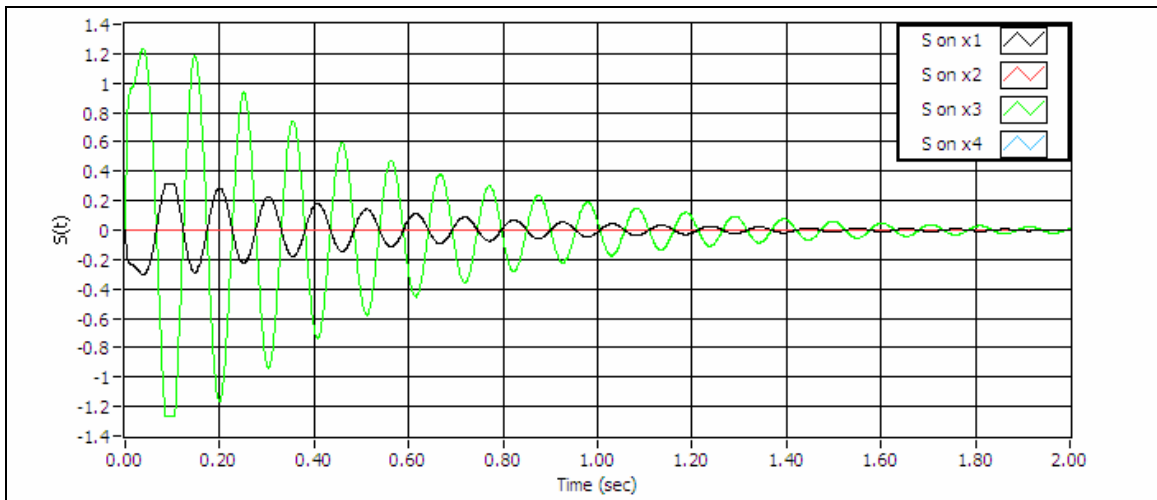
Figure 5.20: Continuous state function produced by boundary layer sliding mode observer (Q_p = 3.65e6, ρ = 60, λ = 1) in presence of 25% parameter variation, based on the modified inertia TA model. The figure shows how the continuous state function approaches zero as estimate errors approach zero, due to the use of a boundary layer.

Table 5.5: Kalman gain ($\underline{K}_L$) and Sliding mode gain ($\underline{K}_s$) for the modified inertia TA model with 25% P.V.

$\underline{K}_L$		$\underline{K}_s$	
8.711	-8.5e3	-2e-5	-5.1e3
103.1	1e-3	-1.4e-7	3e-5
204.6	4.7e-2	1e-4	2e-2
2.2e3	4.613	-3.4e-8	1.8e-5

The stability study simulations indicate that the formerly-discontinuous state functions produced by the boundary layer sliding mode observer have an effect large enough in the presence of large parameter variation to stabilize the observer error dynamics, as intended by design. For the modified lumped parameter model in this study, it was found that the Kalman filter produces unstable estimates at parameter variation of 21% and higher. By comparison, the boundary layer sliding mode observer continues to produce stable estimates up to a parameter variation of 32%.

5.4 Detailed Model and Robust Observer

In the assumed modes method model, the independent variable changed during the study is tip mass. As earlier, the performance criteria is mean squared estimate error of position estimates and velocity estimates, reported separately. In a similar fashion to the lumped parameter model, the position mean square estimate error is composed of position states (modal coordinate positions) and the velocity mean square estimate error is composed of velocity states (modal coordinate velocities) as defined by equation 2.30.

Table 5.6: Parameter variation in AMM model during simulation.

Parameter Variation in Tip Mass (%)	Resulting First Mode (Hz)	Resulting Second Mode (Hz)	Resulting Third Mode (Hz)
0	5.7	49	219.3
45	5.12	47.4	214.3
35	5.24	47.8	214.3

Table 5.6 (continued).			
25	5.36	47.9	216.7
20	5.42	47.9	216.7
15	5.49	48.45	216.7
10	5.55	48.45	216.7
5	5.62	49	219.3
-5	5.75	49.1	219.3
-10	5.88	49.58	221.8
-15	5.95	49.6	221.8

The following figures provide a comparison of the Kalman filter (Q_t = 1e-6) and the boundary layer sliding mode observer (Q_p = 2.5e11, ρ = 5, λ = 37) in presence of parameter variation. The studies do not include the effect of measurement noise. Unlike the lumped parameter model simulations, the assumed mode method model simulations do not indicate a significant performance advantage for the sliding mode observer in presence of uncertainty.
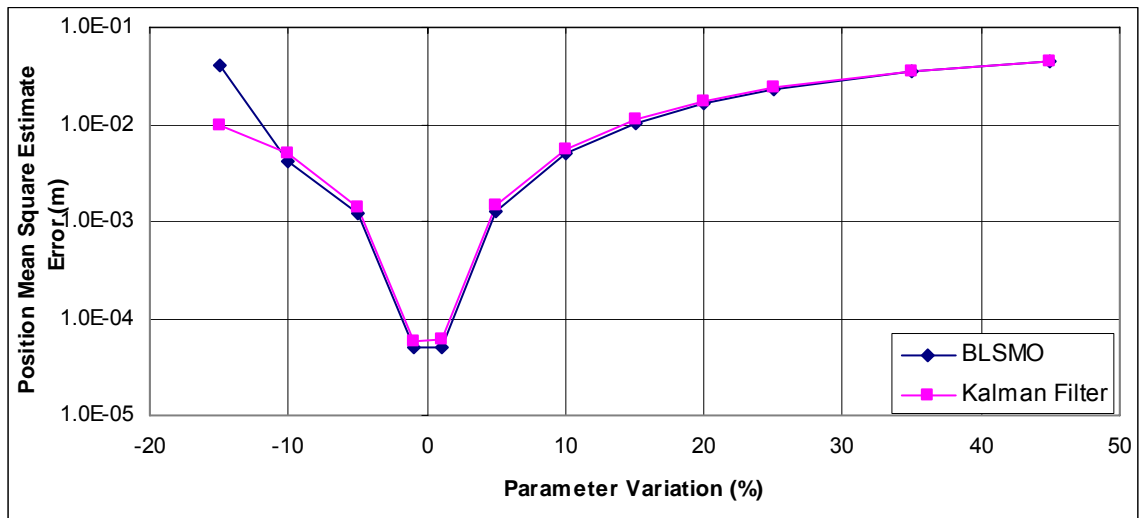
Figure 5.21: Comparison of Kalman filter and boundary layer sliding mode observer (Q_p = 2.5e11, ρ = 5, λ = 37), based on position estimates and the AMM model. The figure shows that according to the AMM model, the boundary layer sliding mode observer performance is no worse or better than the Kalman filter in the presence of uncertainty.
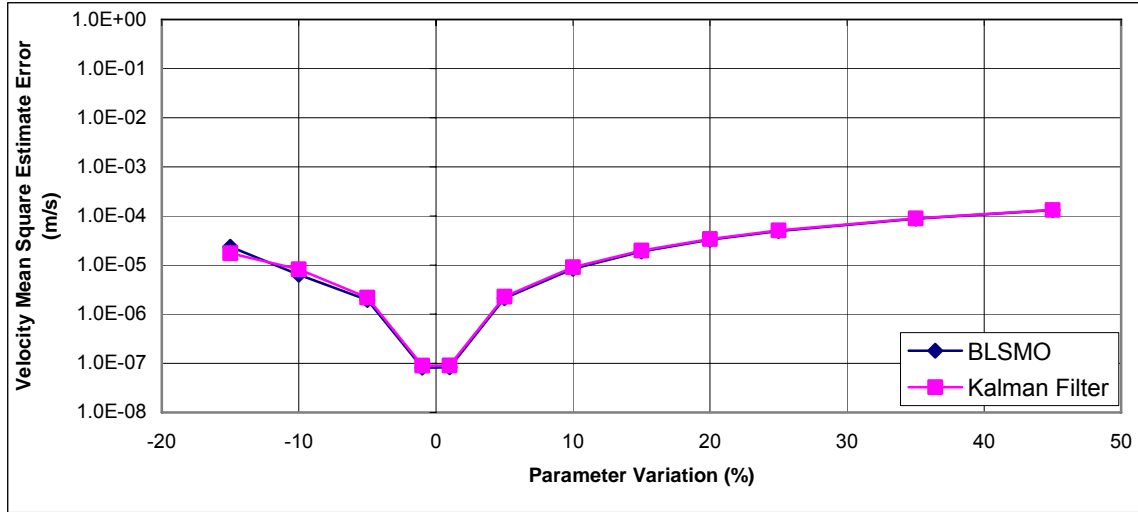
Figure 5.22: Comparison of Kalman filter and boundary layer sliding mode observer (Q_p = 2.5e11, ρ = 5, λ = 37), based on velocity estimates and the AMM model. The figure shows that according to the AMM model, the boundary layer sliding mode observer performance is no worse or better than the Kalman filter in the presence of uncertainty.

Like the lumped parameter model case, stability studies were also undertaken for the assumed modes method model. It was found that around 50% parameter variation, the Kalman filter began producing unstable estimates. Despite repeated attempts, no sliding mode observer or boundary layer sliding mode observer design could be found to stabilize the observer error dynamics in this range of parameter uncertainty.

5.5 Repercussions on Closed-loop Control

Observer dynamics have a clear role to play in closed-loop system response. Fundamentally, the closed-loop system performance and stability is tied to that of the observer. Figure 5.23 shows two closed-loop tip responses, based on the lumped parameter model. Although the initial undershoot expected of non-minimum phase system is not visible in the responses of the lumped parameter models in this section, the existence of non-minimum phase characteristics of these models are indeed verified by a positive zero.

In the presence of 30% parameter variation, the tip is commanded to a set point of 50cm. The simulation demonstrates how improved estimation can lead to better reference tracking of the closed-loop system.
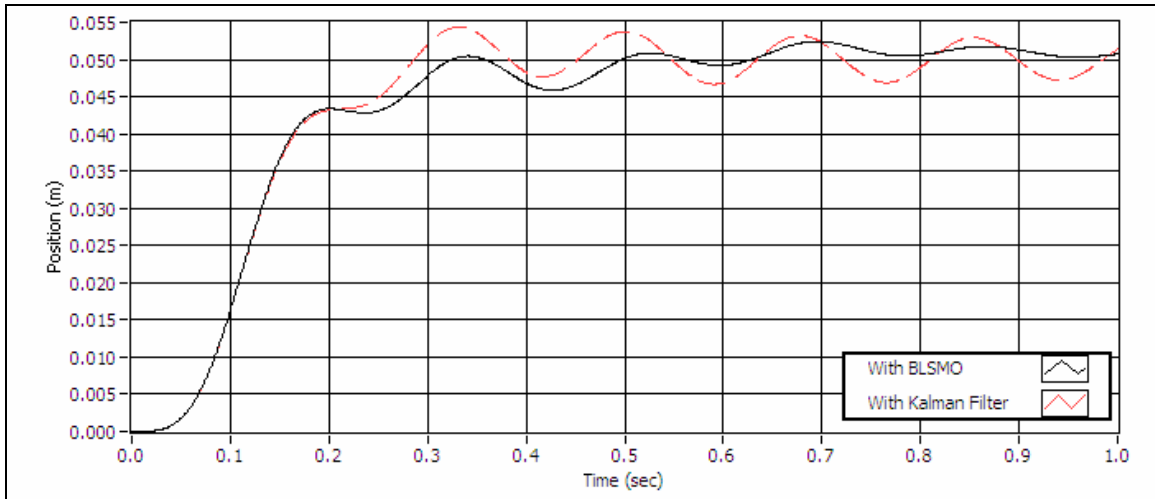
Figure 5.23: In presence of parameter variation of 30%, comparison of closed-loop link tip response with Kalman filter (Q_t = 3e-4) and BLSMO (Q_p = 2e3, ρ = 2.5, λ = 150), based on lumped parameter TA model. The figure shows the commanded tip excitation is noticeably decreased with use of the BLSMO due to improved estimation.

In addition to closed-loop tracking performance, closed-loop stability is obviously impacted by observer performance. The alternative lumped parameter model discussed in section 5.3 is employed again for the stability study here. Figure 5.24 depicts the unstable closed-loop link tip response, when commanded to a set point of 50cm, with use of Kalman filter alone and in the presence of 25% parameter variation. Figure 5.25 shows how under the same uncertainty conditions, a boundary layer sliding mode observer is able to stabilize the closed-loop tip response. It was found that closed-loop stability with use of Kalman filter alone restricted parameter variation to about 21%. With use of the sliding mode observer, this restriction was lifted to 32%.
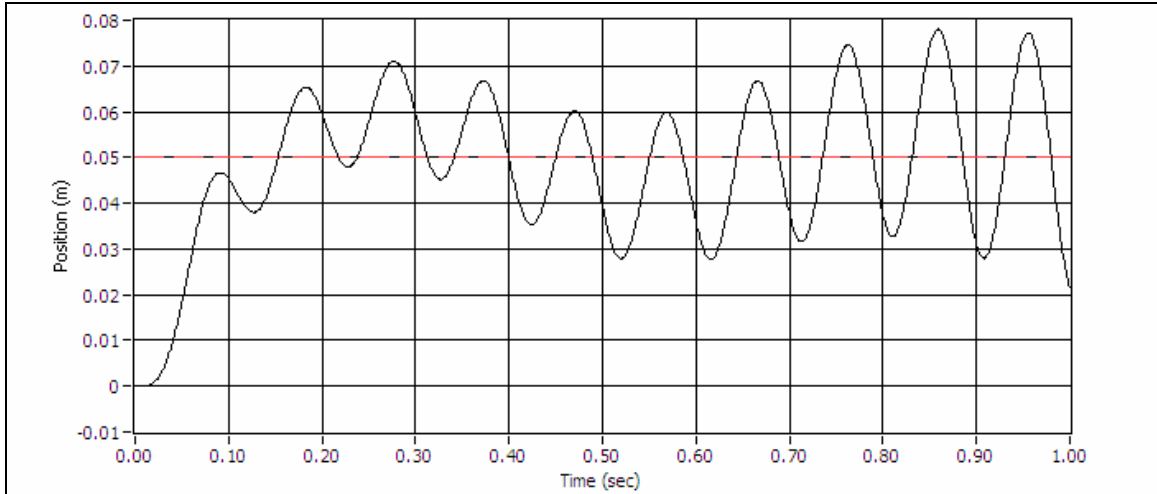
Figure 5.24: Unstable closed-loop link tip response with use of Kalman filter in presence of 25% P.V., based on modified inertia lumped parameter TA model. The figure shows the effect of unstable estimates provided by the Kalman filter on closed-loop stability.
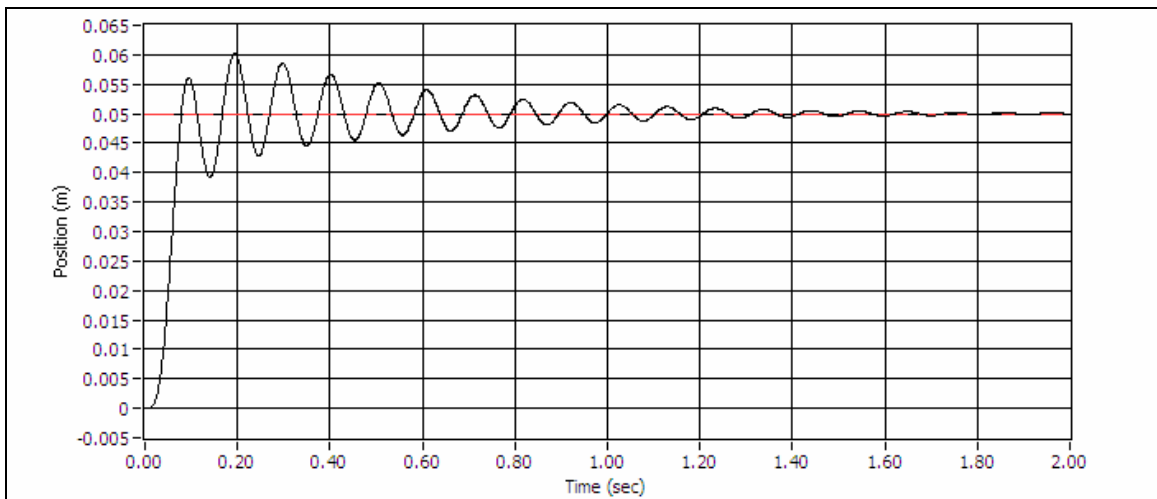
Figure 5.25: Stable closed-loop link tip response with use of boundary layer sliding mode observer (Q_p = 3.65e6, ρ = 60, λ = 1) in presence of 25% P.V., based on modified inertia lumped parameter TA model. The figure showcases the ability of the BLSMO to ensure stable closed-loop control under the same conditions in which the KF is unable to.

71
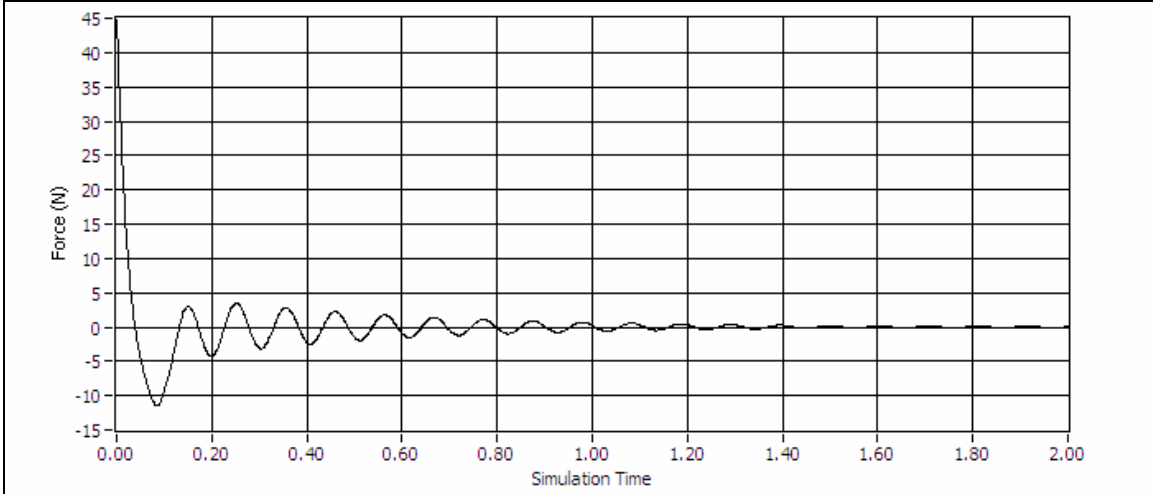
Figure 5.26: Control input for closed-loop system with boundary layer sliding mode observer (Q_p = 3.65e6, ρ = 60, λ = 1) in presence of 25% P.V., based on modified inertia lumped parameter TA model. The figure shows that the control input is kept below pre-assigned hardware saturation levels.

Similarly, for the assumed modes method model, the performance and stability of the closed-loop system was investigated. Due to the disappointing estimation performance of the boundary layer sliding mode observer, as discussed in section 5.4, the closed-loop link tip response cannot be improved with replacement of the Kalman filter with the BLSMO. In addition, the stability of the closed-loop link tip response under significant parameter uncertainties cannot be assured.
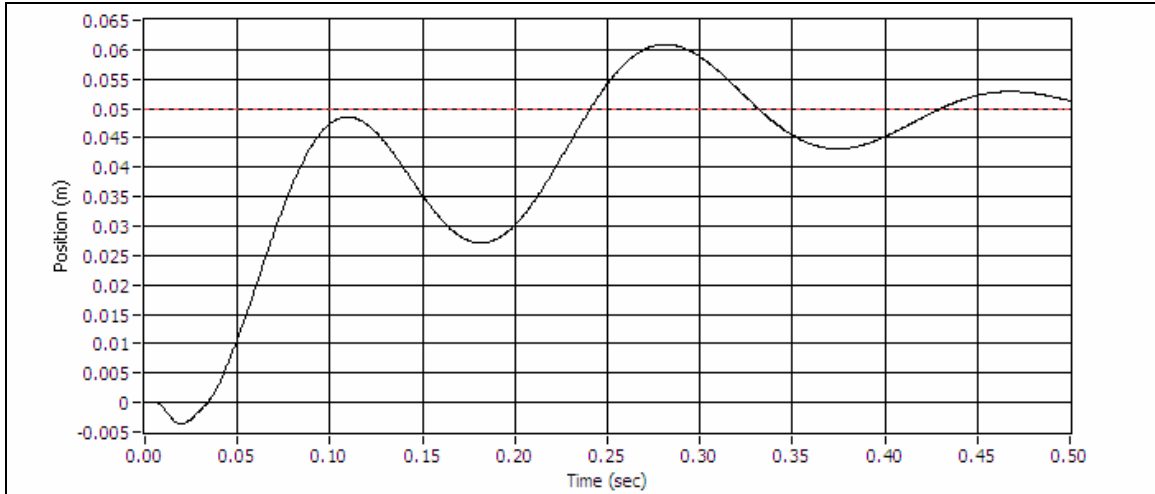
Figure 5.27: In presence of parameter variation of 10%, closed-loop link tip response with BLSMO ($Q_p = 2.5e11$, $\rho = 5$, $\lambda = 37$), based on assumed modes method model. The figure shows that according to the AMM model, there is no improvement in commanded link tip response with use of BLSMO in presence of uncertainty.
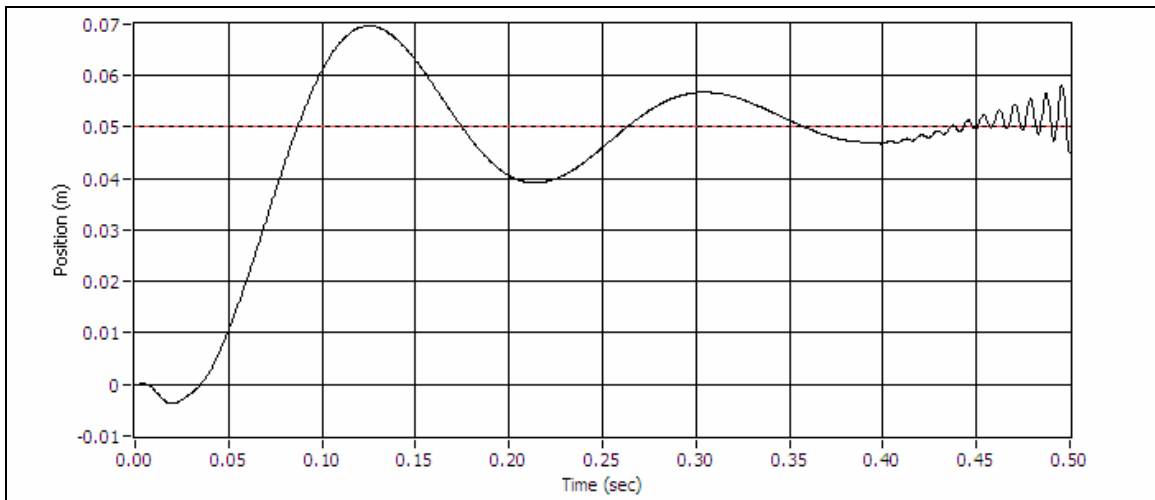
Figure 5.28: In presence of parameter variation of about 50%, unstable closed-loop link tip response with BLSMO ($Q_p = 2.5e11$, $\rho = 5$, $\lambda = 37$), based on assumed modes method model. The figure shows that according to the AMM model, there is no improvement in commanded link tip response with use of BLSMO in presence of uncertainty.

5.6 An Approach for Tuning the Robust Observer

In the course of conducting the numerous simulation studies, an approach for tuning the parameters of the sliding mode observer and the boundary layer sliding mode observer took shape. The approach here was used for developing numerous observer designs based on four different models. The approach is summarized in eight steps provided in Table 5.7.

Table 5.7: An approach for tuning the robust observer (based on the Kalman filter) in simulation.

	Step	**Observe**
1.	Configure observer initial conditions.	
2.	Find Kalman gain $\underline{K}_L$.	Run simulation and record mean square estimate errors (MSE) for later comparison.
3.	Set $\rho = 1$, Select $Q_p > 0$. Start small and increase.	Increase in increments of 1, 10, 100, 1000, so on. In general, the larger the elements of $\underline{C}$, the larger the step size of increment is needed.
4.	Run simulation to observe MSE and repeat step #3 as needed.	The goal is to find a minimum for MSE by tuning only Q_p, by arriving at MSE that is lower than that of Kalman filter alone.
5.	Select $\rho > 0$. May increase or decrease.	ρ has same affect on MSE as tuning Q_p but with more precision. A very large discontinuous state function leads to estimate unstability, thus ρ is upper bounded.
6.	Run simulation to observer MSE and repeat step #5 as needed.	The goal is to further minimize MSE by tuning only ρ. The smaller the step size used for Q_p in step #3, the less the adjustment to ρ is needed. At this point, MSE should be reduced and switching about a sliding surface in error space should be apparent.
7.	Select $\lambda > 0$. Start small and increase.	Only once the pair Q_p and ρ are finalized, should λ be considered. Small value for λ gives more discontinuous control, more estimation chatter.

	Table 5.7 (continued).	
8.	Run simulation to observer MSE and repeat step #7 as needed.	The goal is to further minimize MSE by tuning only λ. Directly minimizing MSE results in indirectly smoothing out estimates.

5.7 Considerations for Future Studies

In the simulations studies conducted, the Kalman filter is designed based on a process noise covariance matrix which penalizes all states equally. There are at least two concerns with this simplified approach which should be corrected in future studies. First, using the lumped parameter model for illustration, there is no process uncertainty in states x_2 and x_4 given the state assignments $x_2 = \dot{x}_1$ and $x_4 = \dot{x}_3$ in equations 2.7 and 2.9. Second, again using the lumped parameter model for illustration, placing equal penalties on position and velocity states and neglecting the difference in units results in a Kalman filter with inferior performance. For these two reasons, each element of the diagonal process noise covariance matrix should reflect both the sources of uncertainty and the units of the states themselves for proper formulation of the Kalman filter.

As an illustration, the process noise covariance matrix

$$\underline{Q}_t = \begin{bmatrix} 0 & 0 & 0 & 0 \\ 0 & 3e-4 & 0 & 0 \\ 0 & 0 & 0 & 0 \\ 0 & 0 & 0 & 3e-4 \end{bmatrix} \tag{5.6}$$

was used in a simulation with process noise and low measurement noise given in Table 5.4. The updated Q_t resulted in a 92.4% decrease in velocity mean square estimate error (from 4.53e-7 to 3.44e-8 m/s) and a 81.2% decrease in position mean square estimate error (from 2.42e-10 to 4.54e-11 m). On a related note, the robust observer design parameter $\underline{Q}_p$, an arbitrary positive-definite symmetric matrix, should be designed with the same consideration for unit consistency in mind.

75

A note must be made in regards to the boundary layer versions of the robust observer. According to equation 4.34, the transition between a discontinuous and a continuous state function depends upon the term $\left\| \underline{y} - \hat{\underline{y}} \right\|$. For models with tip acceleration as output rather than tip position, there is a lack of unit consistency in the term $\left\| \underline{y} - \hat{\underline{y}} \right\|$ since it now consists of a position measurement (m) and an acceleration measurement (m/s^2), which is based on units of time. The author suggests use of proper scaling factors to correct this unit inconsistency in future studies. The units of the measurement have a bearing on when the transition between a discontinuous and a continuous state function occurs as illustrated in Figure 5.29 and 5.30. In the first figure, the BLSMO is operating with a continuous state function. Compare this to the straight line motions in the second figure which are indicative of operation outside the boundary layer.
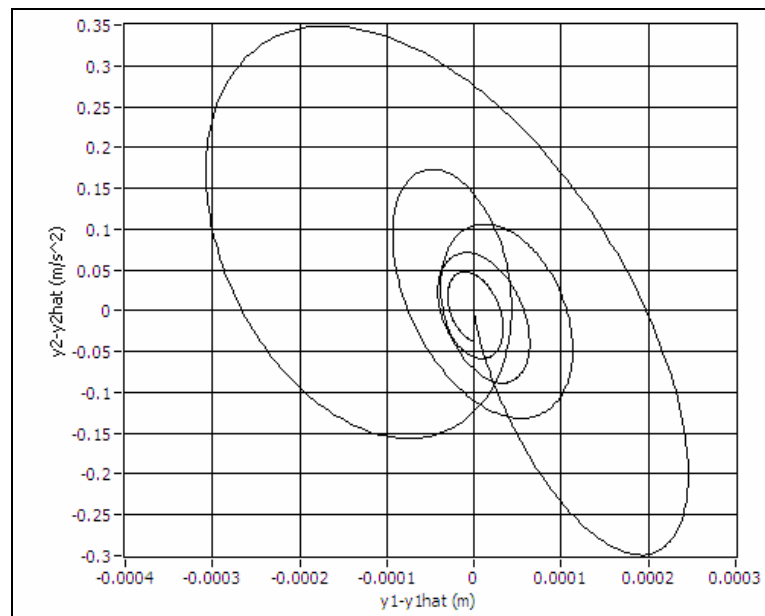
Figure 5.29: Elements of $\left\| \underline{y} - \hat{\underline{y}} \right\|$ in presence of parameter variation of 5%, with BLSMO (Q_p = 1e5, ρ = 0.5, λ = 10) and no scaling factor for acceleration measurement, based on TA model. This figure shows the BLSMO is operating with a continuous state function for all time.
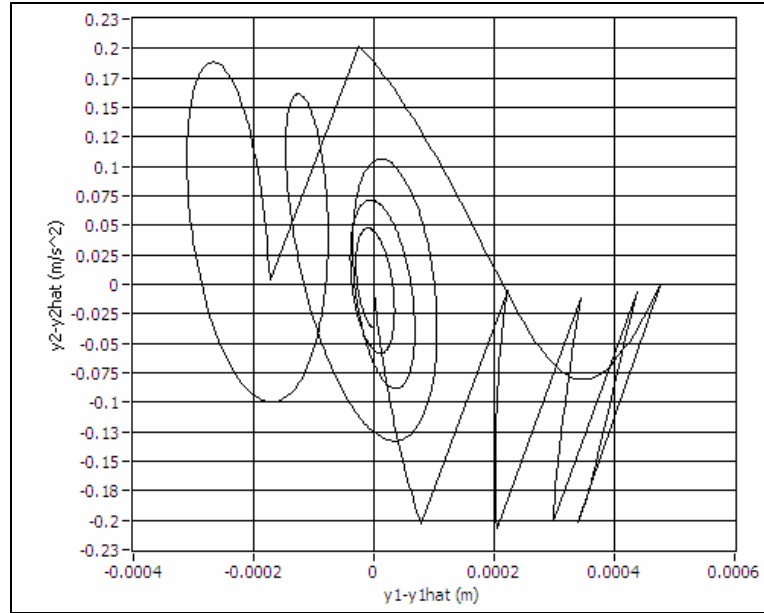
Figure 5.30: Elements of $\lVert \underline{y} - \hat{\underline{y}} \rVert$ in presence of parameter variation of 5%, with BLSMO (Q_p = 1e5, ρ = 0.5, λ = 10) and a scaling factor of 50 for acceleration measurement, based on TA model. This figure shows transitions occurring between a discontinuous and continuous state function due to a hypothetical scaling factor applied to correct unit inconsistency in $\lVert \underline{y} - \hat{\underline{y}} \rVert$.

5.8 Summary

Simulations based on two closely-related lumped parameter models have shown that most state estimate errors produced by the sliding mode observer (SMO) and boundary layer sliding mode observer (BLSMO) in the presence of parameter uncertainty are in fact reduced when compared to estimates from a Kalman filter. The simulation studies have further shown that BLSMO estimates are superior to SMO and that the performance of different BLSMO designs converges. In presence of Gaussian white measurement noise, BLSMO estimates are in fact better than with the Kalman filter alone. Another notable result from simulation is that the structure of the output matrix $\underline{C}$ in the tip acceleration output model did not harm performance of the BLSMO. This is saying that even though there is now uncertainty in $\underline{C}$, which the formulation of the

77

sliding mode observer in Chapter 4 does not consider, the advantages of the BLSMO over the Kalman filter still stand. Finally, simulations showed how improved estimation can lead to better reference tracking of the closed-loop system.

Simulations based on the modified inertia lumped parameter model showed that in situations of high parameter uncertainty where the Kalman filter produces unstable estimates, the BLSMO observer estimates are in fact stable. The parameter variation limit for the Kalman filter is 21%, while the BLSMO continues to produce stable estimates up to parameter variation of 32%. As a result, the BLSMO is able to stabilize the closed-loop tip response.

Simulations based on the assumed modes method proved less fruitful. Simulations reported Kalman filter estimates very close to those of BLSMO. No benefits in terms of closed-loop control with the BLSMO were found. In the lumped parameter models, at least one state is directly output as a measurement and at most three states are observed. In the assumed modes method model, no state is directly output and all eight are observed. Another difference worthy of pointing out is that parameter variation in the assumed modes method model changes the eigenvectors which changes the $\underline{A}$, $\underline{B}$, $\underline{C}$ and $\underline{D}$ system matrices. This is in contrast to the lumped parameter model in which, for example, variation in tip mass affects only $\underline{A}$. A third possible factor is observability. Observability of the lumped parameter models is easily confirmed. Software such as Matlab used to check observability for the assumed modes method model showed a dependence on link parameters. Perhaps the disappointing performance of the BLSMO is explained by one or the combination of these factors.

A few concerns have arisen following the simulations. First, the Kalman filter does not discriminate against use of either the simple or the detailed model. It works with either unlike the sliding mode observer at hand. Second, the anomaly at 60% parameter variation in several of the figures is of concern. The author is not able to explain why it is that the SMO estimates are so often worse than KF at this specific parameter variation.

Two concerns regarding evaluation of uncertainty bounds have also arisen. It was also discovered in the process of obtaining the bounds on uncertainty $\underline{\xi} = (\underline{P}^{-1}\underline{C}^{T})^{-1}(\Delta\underline{A}\underline{x})$, that $(\underline{P}^{-1}\underline{C}^{T})^{-1}$ cannot be evaluated if $\underline{P}^{-1}\underline{C}^{T}$ is non-square. This poses a challenge for the assumed modes method case. Besides that hurdle, the uncertainty upper bound is time varying since it depends upon the state vector. The criteria provided for the lower bound on ρ, given by equation 4.29, proved impossible to satisfy, given the large bounds on the state vector during simulation. It was not used and instead ρ was selected in a trial by error manner.

CHAPTER 6

EXPERIMENTS

Several questions surrounding implementation have arisen. Exactly how are robust observer design parameters initialized? How much of the parameter tuning is trial and error and in what way is optimality of the tuned parameters assured? The sensitivity of the hardware in the physical system to observer design parameters needs investigation. The computational burden imposed by the algorithm must be looked into. Finally, the estimation performance shown by simulations needs verification.

6.1 Experimental Setup

The experimental setup consists of a flexible link with a tip mass of 0.11kg attached to an Anorad D.C. linear motor with a moving mass of 9.6kg on a track with a full range of 1.55m, as depicted in Figure 6.1. The physical properties of the flexible link, including the natural frequencies, can be found in Table 2.1. The motor gain (N/V) is approximated as 6.13 by experimental means as discussed in section 2.2. Based on the range of control signal supplied to the motor servo-amplifier, this indicates motor saturation will occur above a continuous force of about 61.3N. In addition, the motor bandwidth was found experimentally to be 2.2hz.

An accelerometer and a linear encoder provide measurements of tip acceleration and base position, respectively. The PCB piezoelectric accelerometer has a bandwidth of 3hz at a measurement accuracy of +/-10%. The accelerometer signal is low-pass filtered using an RC circuit with a cut-off frequency of 480hz to remove electrical noise. The Anorad encoder provides motor displacement with a resolution of 1μm.

A target PC running National Instruments LabVIEW Real-Time 8.5 operating system is used for acquiring and conditioning sensor signals, state estimation and

computation of control signal, and output of control signal to the linear motor. The control loop operates at a minimum of 1khz, and under certain instances can operate reliably at 2khz. The developed LabVIEW control application also allows the transfer of control and the relaying of status information to a host PC. Figure 6.2 provides a schematic of the hardware involved in the system.
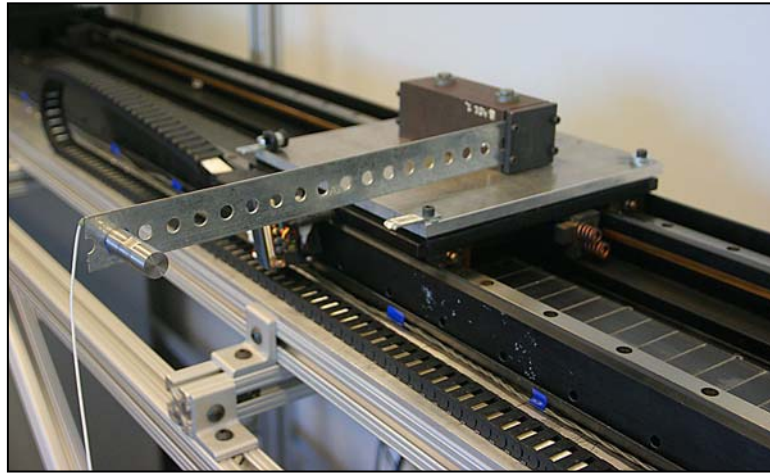
Figure 6.1: Single flexible link propelled by a linear D.C. motor.
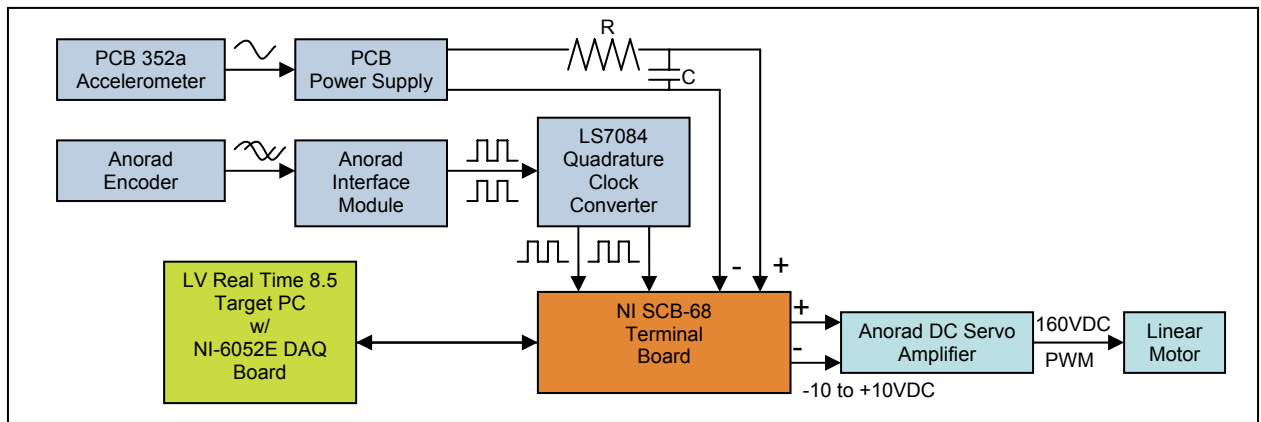
Figure 6.2: Schematic of system hardware.

On the software side of the test-bed, National Instruments LabVIEW 8.5 based application consists of a total of four LabVIEW VIs, two residing on the host PC and two on the target PC.
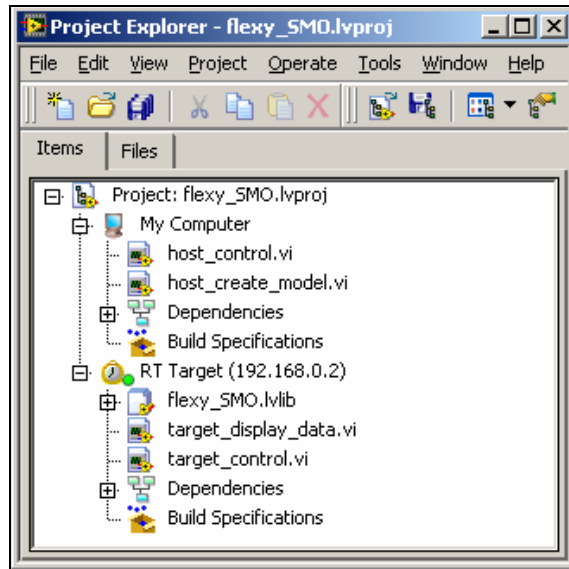
Figure 6.3: LabVIEW Real Time 8.5 application for experimental test-bed.

The "host_create_model" VI on the host PC creates a LabVIEW measurement file which contains the model data in state-space form, state-feedback gain, feed-forward gain, Kalman gain, and sliding mode gain. All of this data is generated off-line in advance and is needed by the observer and controller for online state estimation and control. The measurement file is downloaded to the target PC where it resides and is called at runtime by a VI running on the target PC. The "host_create_model" VI needs to be run only when the developer makes changes to the model, a controller parameter, or an observer parameter. The most common parameters tuned by the developer are available on the Front Panel of the VI for direct input and are summarized in Table 6.1.

Table 6.1: Front Panel inputs for "host_create_model" VI.

Parameter Input on Front Panel	Function of Parameter
Q_t (process noise covariance matrix)	Determines Kalman filter poles.
Q_p (From equation 4.26)	Determines sliding mode gain K.

Table 6.1 (continued).	
τ (From equation A.1)	Determines feedback controller poles.

The "host_control" VI on the host PC communicates directly with the "target_control" VI on the target PC at runtime using network-publised shared variables. The developer uses the Front Panel of this VI to send commands directly at run-time. The inputs supplied by the developer are summarized in Table 6.2. In addition to allowing direct control over hardware at runtime, status information is relayed back to the developer. This information includes the execution time (in seconds), plot of the reference signal being tracked (in cm) and the measured base displacement (in cm). The VI updates at 10hz to minimize overhead and avoid causing jitter in the deterministic portion of the application (the target VIs).

Table 6.2: Front Panel inputs for "host_control" VI.

Parameter Input on Front Panel	Function of Parameter
Closed-Loop Control On/Off	Toggles between closed-loop control and an output of 0V to the motor.
Stop Execution	Stops the target VI "target_LP_closedloop" and saves recorded signal data to a local file on target.
Sliding On/Off	Disconnects the discontinuous state function in the observer. (Essentially switches between a SMO and a Kalman Filter)
Boundary Layer On/Off	Switches between a SMO and BLSMO.
ρ	On-line tuning of sliding mode observer parameter.
λ	On-line tuning of sliding mode observer parameter.

The "target_control" VI performs the most essential functions needed for real-time control. The five core components of this VI include: 1) a "read from measurement file" subVI for initializing model, observer and controller parameters, 2) a critical-priority simulation loop containing the model-based observer and controller for real-time control, 3) a normal-priority timed loop for retrieving signal data using FIFO, 4) "a write to measurement file" subVI for logging data to a local file on the target and 5) network-published shared-variables for transferring control and relaying status information to the host VI "host_control."

The "target_display_data" VI displays recorded signal data including the reference signal, measured and estimated signals and control input (Volts).

6.2 Study Overview

The focus of the study is to investigate questions surrounding observer implementation. Specifically, the study will look at how the sliding mode observer is tuned for a physical system. A few points must be made about the study. The first thing to note is that all of the observers are based on the lumped parameter model in the experiments. Observers based on the assumed modes method model, a better representation of flexible link dynamics, were tuned to provide excellent estimates of tip acceleration. Estimates of base position however predicted an underdamped base response. Under closed-loop control, these underdamped base position estimates led to a persistent phase discrepancy between actual and estimated base position which made tuning of the controller a challenge. The observer based on the lumped parameter model proved far easier to tune and provided stable closed-loop control. With time a precious commodity, the lumped parameter model was selected for all of the following experiments.

The model with tip acceleration as an output is employed. This allowed for the use of the acceleration signal directly without having to integrate to reach tip position. The benefit of this approach is not having to deal with the issue of accelerometer drift.

Since design of the sliding mode observer is split into design of the Kalman filter part and then the discontinuous state function term, the logical approach is to first achieve the best possible base position and tip acceleration estimates with the Kalman filter alone. The rationale is that given reliable estimates of these measurable quantities, we can assume the estimates of unmeasurable states are reliable themselves. The Kalman filter parameters are provided in Table 6.3 and are the same as those used in the simulations.

Table 6.3: Noise covariance data for Kalman filter simulations and experiments.

R_{11}	3.87e-10
R_{22}	2.59e-4
Q_t	3e-4

Covariance of R_{11} reflects a standard deviation of 1.97e-5 meters in the position measurement. Covariance of R_{22} corresponds to a standard deviation of 0.0161 m/s^2 in the acceleration measurement. Covariance of Q_t is based on manual fine tuning of the Kalman filter. The resulting Kalman gain is

$$\underline{K}_L = \begin{bmatrix} 528 & -0.863 \\ 713 & -0.184 \\ 1.08e3 & 0.983 \\ 1.06e3 & 0.965 \end{bmatrix}. \tag{6.1}$$

The feedback gain $\underline{K}_c$, is again based on the method of symmetric root locus, and reflects a value of 0.5e9 for τ for all experiments. The tuned gains

$$\underline{K}_c = \begin{bmatrix} -1.01e4 & 0.056e4 & 3.25e6 & 0.066e4 \end{bmatrix} \tag{6.2}$$

and

$$F = 2.24e4 \qquad\qquad (6.3)$$

provide the best tracking of the reference signal. In all experiments, the tip position is commanded to follow the reference signal. This is done by penalizing state x_1 in the method of symmetric root locus and in design of the feed-forward gain F.

As a finale note, the observer did not receive a truncated input when the actual control signal was saturated. This can easily be fixed by placing a saturation function on the input (N) signal in the LabVIEW simulation loop in "target_control.vi."

6.3 Optimal Observer

A regulator is designed with the Kalman filter providing state estimates and the result is shown in Figure 6.3. Two impulse responses can be seen, with the first showing free vibration and the second showing suppression of the first vibration mode by the regulator in about 1.5 seconds. The next series of figures compare the measured and estimated signals, and it can be seen that very good estimates are being provided by the Kalman filter.
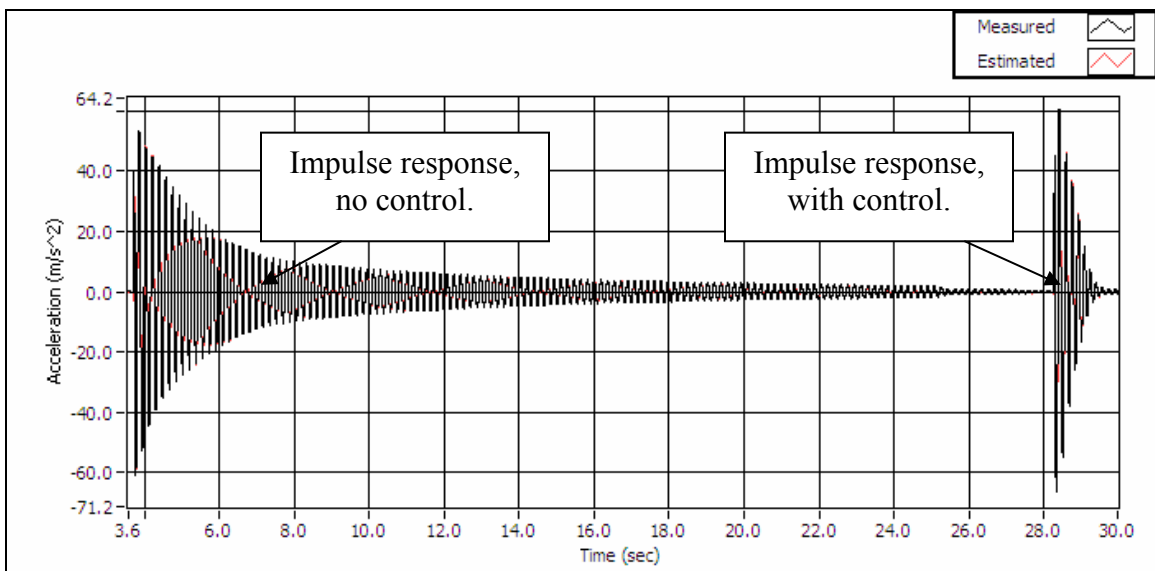
Figure 6.4: Vibration suppression with regulator ($\tau = 0.5e9$) and Kalman filter, at execution rate of 1khz. This figure demonstrates suppression of the first mode with state-feedback control.
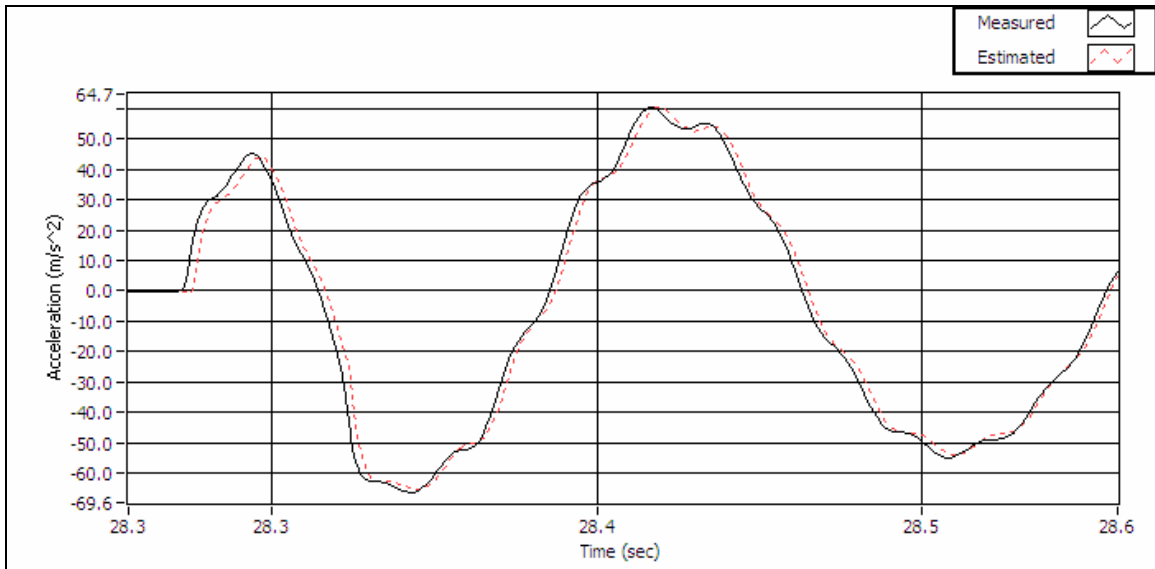
Figure 6.5: Measured and estimated tip acceleration by Kalman filter. This figure shows the estimation accuracy of the Kalman filter alone, with a delay of less than 2ms between measured and estimated signal.
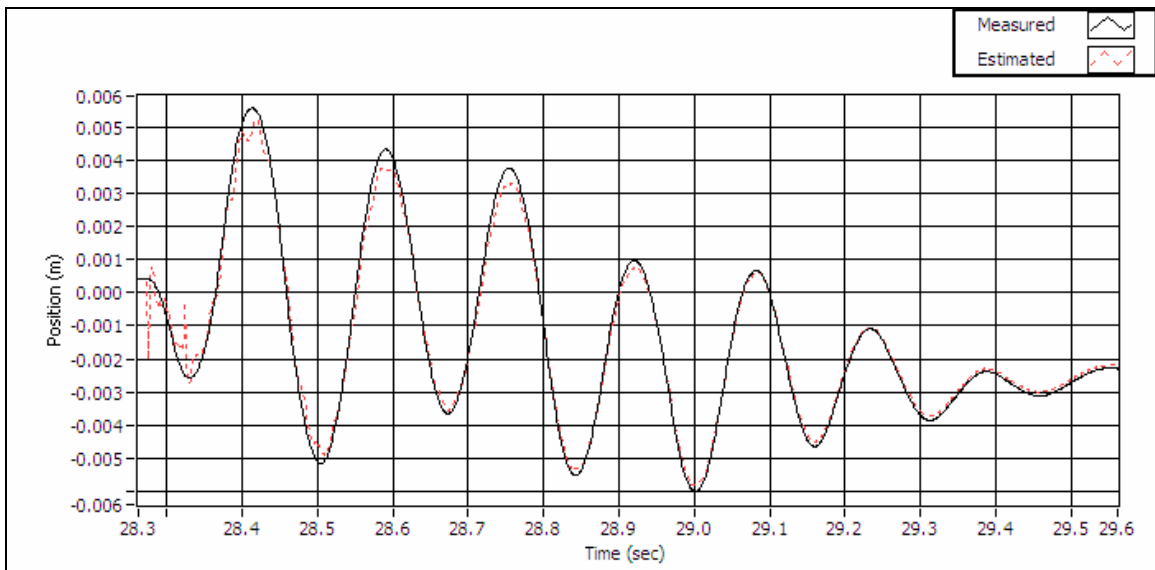
Figure 6.6: Measured and estimated base position by Kalman filter. This figure shows the estimation accuracy of the Kalman filter alone.
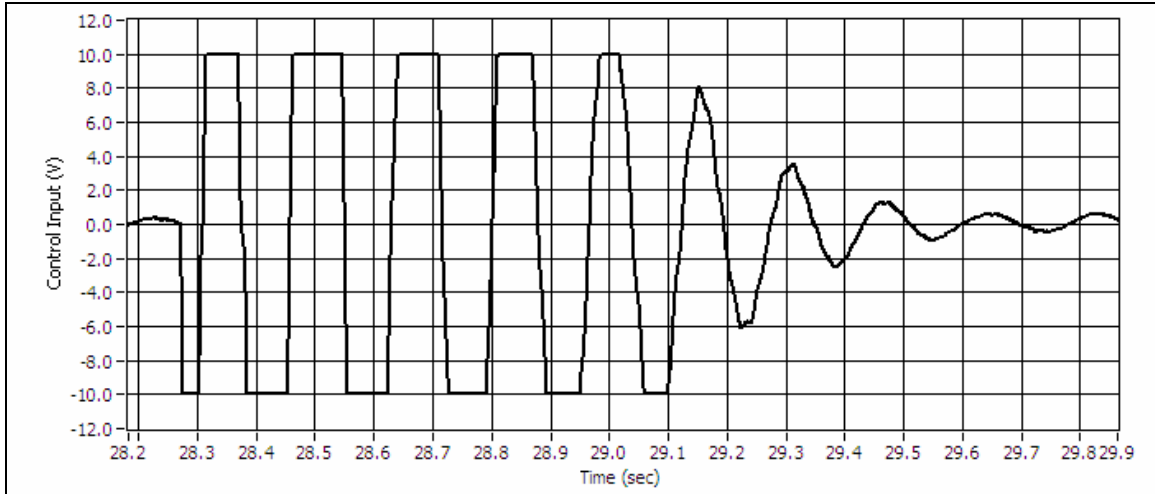
Figure 6.7: Control input (V) during vibration suppression with regulator ($\tau = 0.5e9$) and Kalman filter. This figure shows saturation of the control signal as the controller dampens the first mode, indicating too much feedback gain.

The tuned regulator with Kalman filter combination is also used to track a time varying reference signal. The reference signal is a square wave with peak to peak amplitude of 25cm filtered to remove discontinuities which cause excessive tip excitation and thus motor saturation. Figure 6.7 depicts the base position and Figure 6.8 depicts the tip acceleration during tracking.
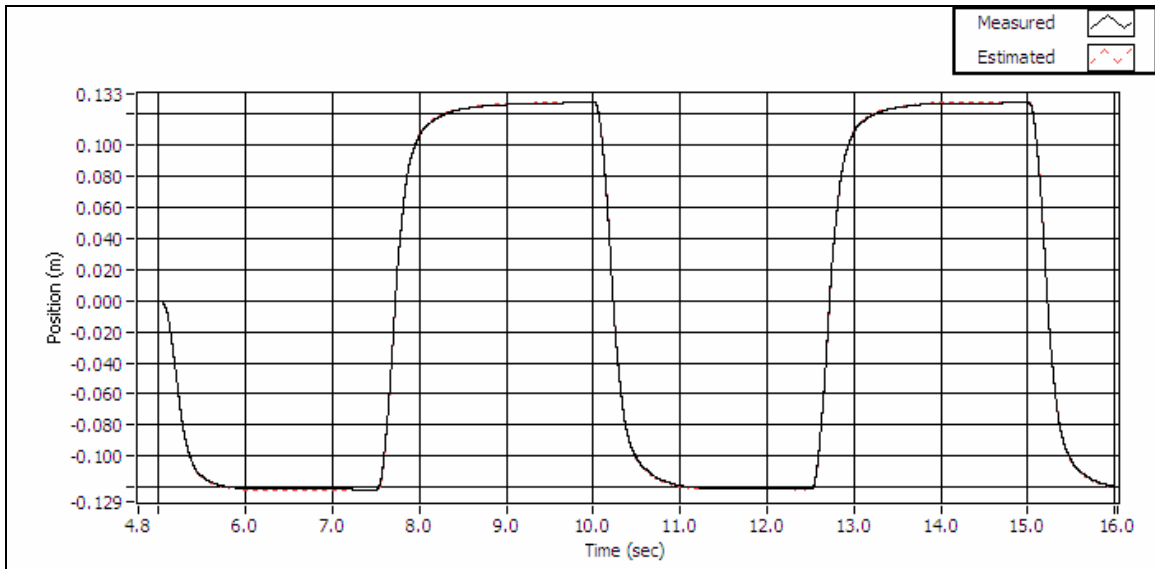
Figure 6.8: Measured and estimated base position during tracking of a reduced-rate square wave with regulator (τ = 0.5e9) and Kalman filter, at execution rate of 1.33khz. This figure shows the tracking capability of the tuned closed-loop system. (Measured and estimated signals almost entirely overlaid)
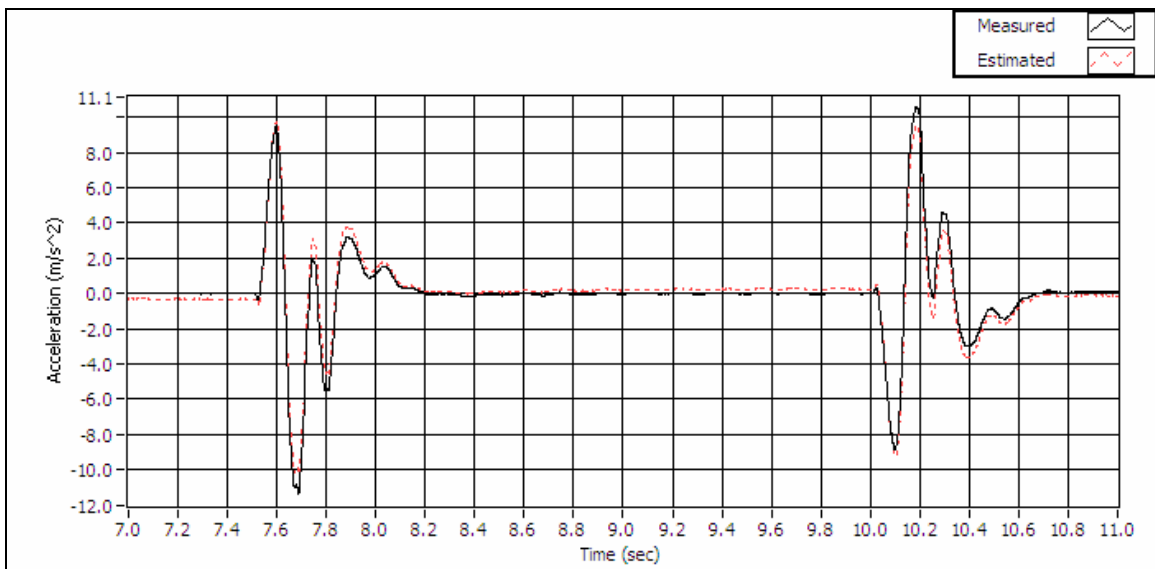
Figure 6.9: Measured and estimated tip acceleration during tracking of a reduced-rate square wave with regulator (τ = 0.5e9) and Kalman filter, at execution rate of 1.33khz. This figure shows maximum tip excitation occurs during rapid motions of the base, all the while the Kalman filter estimates are very accurate.

The next series of figures illustrate the effects of parameter variation on closed-loop control. In the first scenario, illustrated by Figures 6.10 to 6.15, the observer and controller are based on fixed model parameters while the physical tip mass is varied. With an increase in tip mass, the amplitude of tip vibration is noticeably decreased, it takes longer to suppress tip vibration during rapid movement and residual vibrations persist when stationary. With a decrease in tip mass, the magnitude of tip acceleration is noticeably increased, it takes about the same time as with nominal tip mass to suppress tip vibration during rapid movement, and residual vibrations persist when stationary. With up to a 426% increase in tip mass and a 70% decrease in tip mass, the commanded tip position remains asymptotically stable.

In contrast, the parameter variation in the second scenario, illustrated by Figures 6.16-18, does lead to a loss of asymptotic stability. With an increase in link length of 91%, effectively relocating the tip mass from 0.32m to 0.61m along the length of the link, the commanded tip position is at best marginally stable. It should be mentioned that link length is not an actual parameter in the lumped-parameter model. Parameter variation in link length corresponds to parameter variation in link damping and stiffness which are actual model parameters.
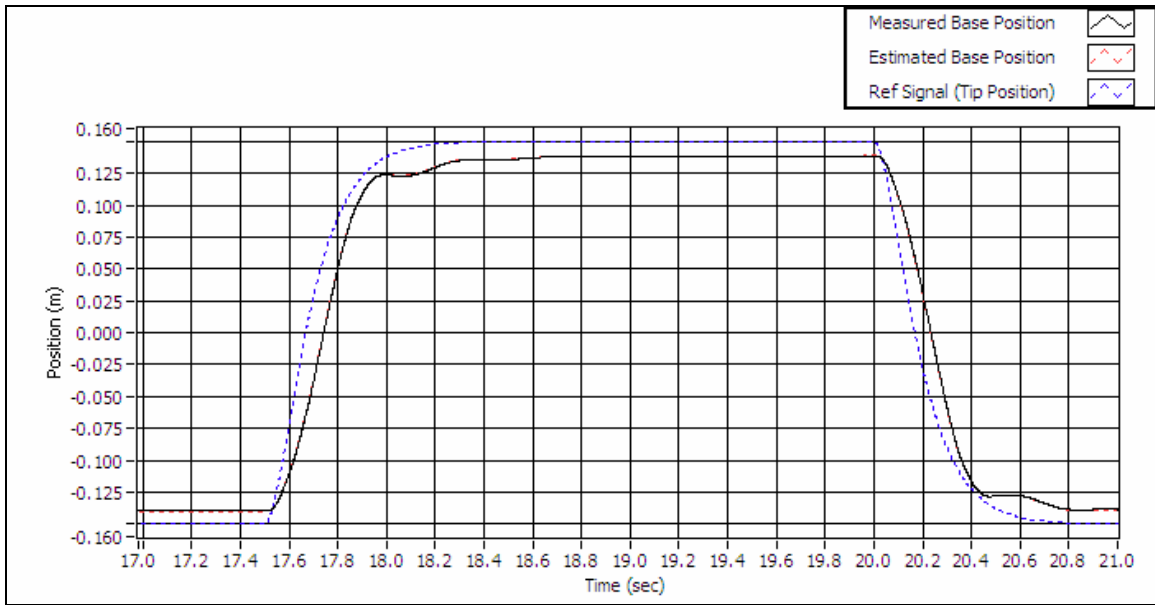
Figure 6.10: With tip mass increased by 426% (from 0.11kg to 0.579kg), measured and estimated base position during tracking of a reduced-rate square wave with regulator (τ = 0.5e9) and Kalman filter, at an execution rate of 1khz. This figure shows reduced tracking capability of the closed-loop system with modeling error in tip mass, however without loss of asymptotic stability. (Measured and estimated signals almost entirely overlaid)
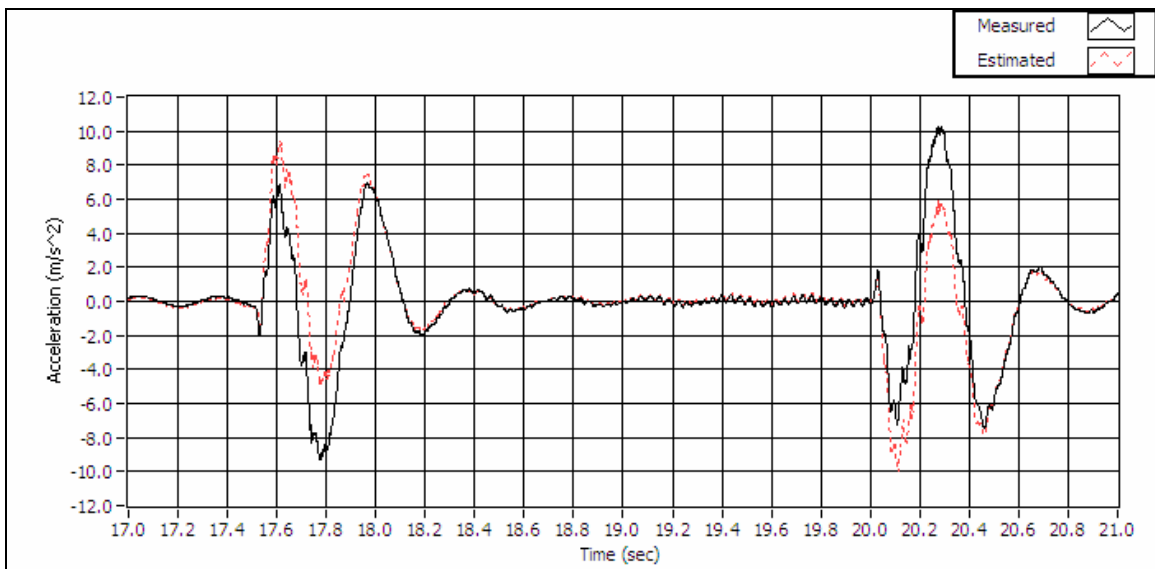
Figure 6.11: With tip mass increased by 426% (from 0.11kg to 0.579kg), measured and estimated tip acceleration during tracking of a reduced-rate square wave with regulator (τ = 0.5e9) and Kalman filter, at an execution rate of 1khz. This figure shows that it now takes longer to suppress tip vibration during rapid movement due to modeling error in tip mass (compare to Figure 6.9).

91
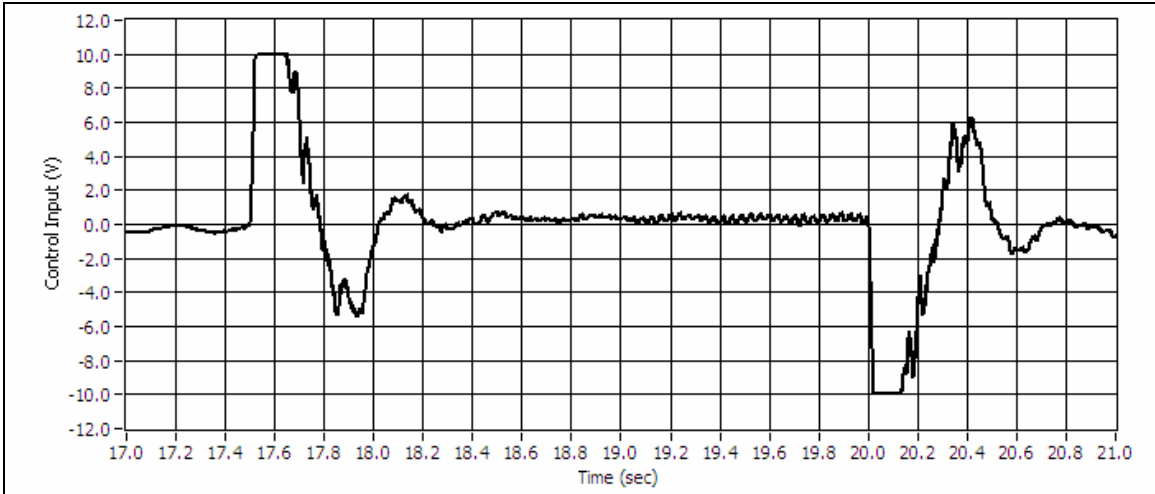
Figure 6.12: With tip mass increased by 426% (from 0.11kg to 0.579kg), corresponding control input during tracking of a reduced-rate square wave with regulator ($\tau = 0.5e9$) and Kalman filter, at an execution rate of 1khz. This figure shows motor saturation occurs during closed-loop control with modeling error in tip mass.
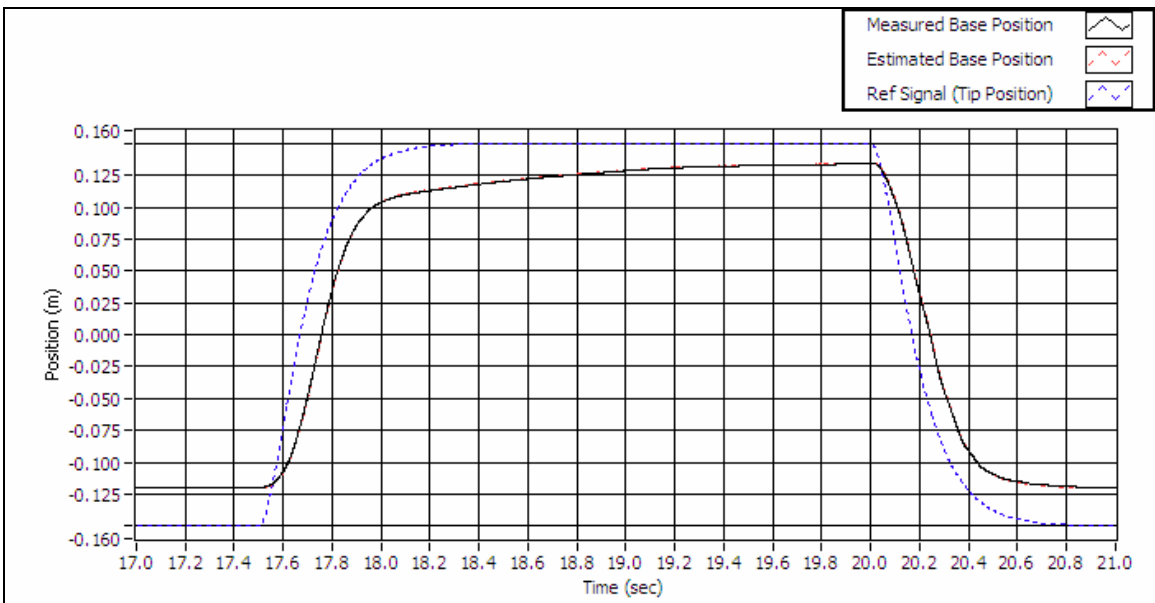
Figure 6.13: With tip mass decreased by 70% (from 0.11kg to 0.033kg), measured and estimated base position during tracking of a reduced-rate square wave with regulator ($\tau = 0.5e9$) and Kalman filter, at an execution rate of 1khz. This figure shows reduced tracking capability of the closed-loop system with significant modeling error in tip mass, however without loss of asymptotic stability. (Measured and estimated signals almost entirely overlaid)
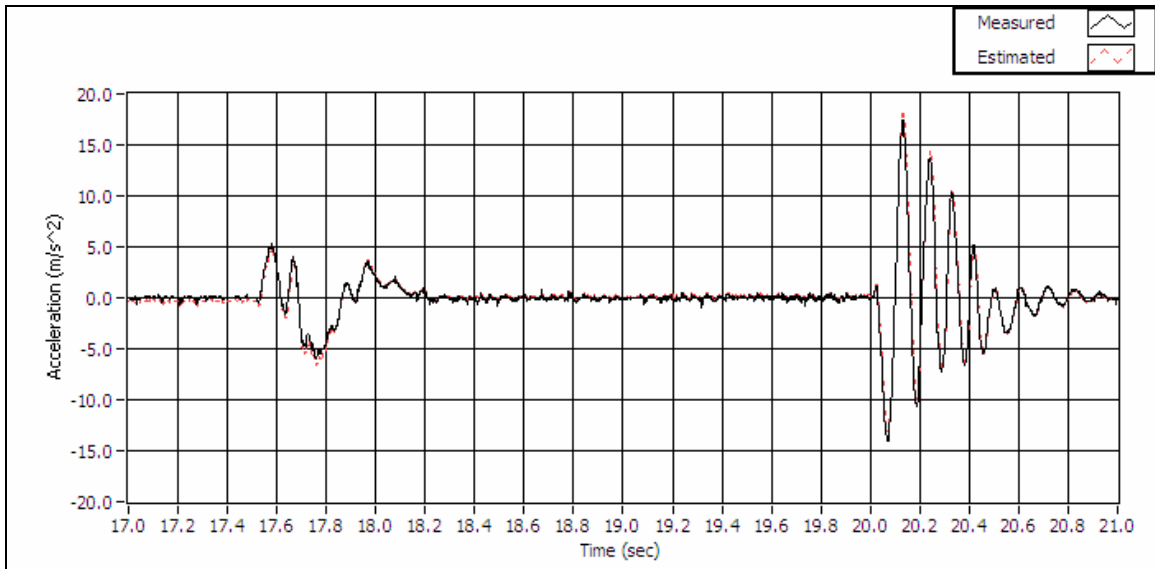
Figure 6.14: With tip mass decreased by 70% (from 0.11kg to 0.033kg), measured and estimated tip acceleration during tracking of a reduced-rate square wave with regulator (τ = 0.5e9) and Kalman filter, at an execution rate of 1khz. This figure shows that in this instance of modeling error in tip mass, it still takes about the same time to suppress tip vibration during rapid movement as with nominal tip mass (compare to Figure 6.9).
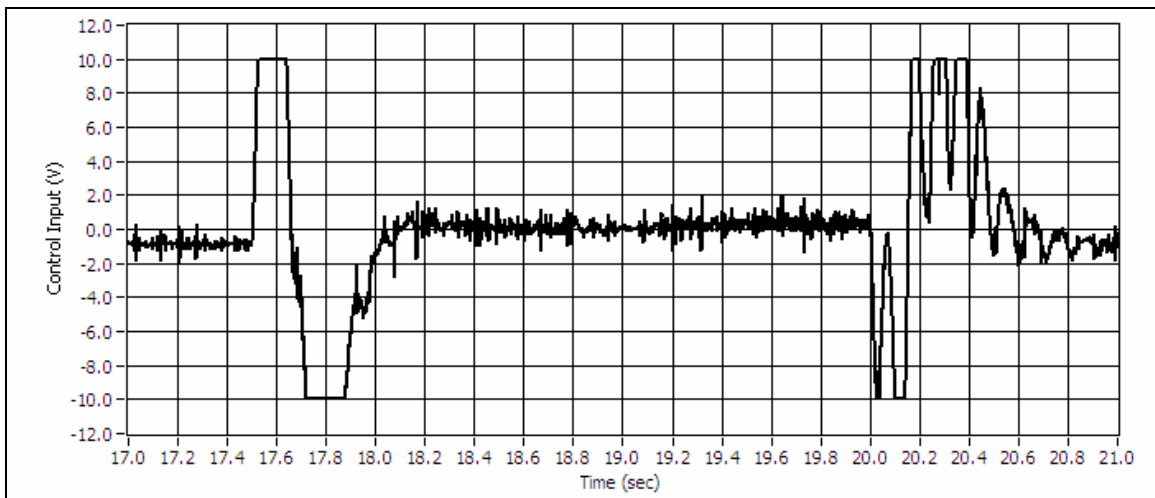
Figure 6.15: With tip mass decreased by 70% (from 0.11kg to 0.033kg), corresponding control input during tracking of a reduced-rate square wave with regulator (τ = 0.5e9) and Kalman filter, at an execution rate of 1khz. This figure shows motor saturation occurs during closed-loop control with decreased parametric variation.
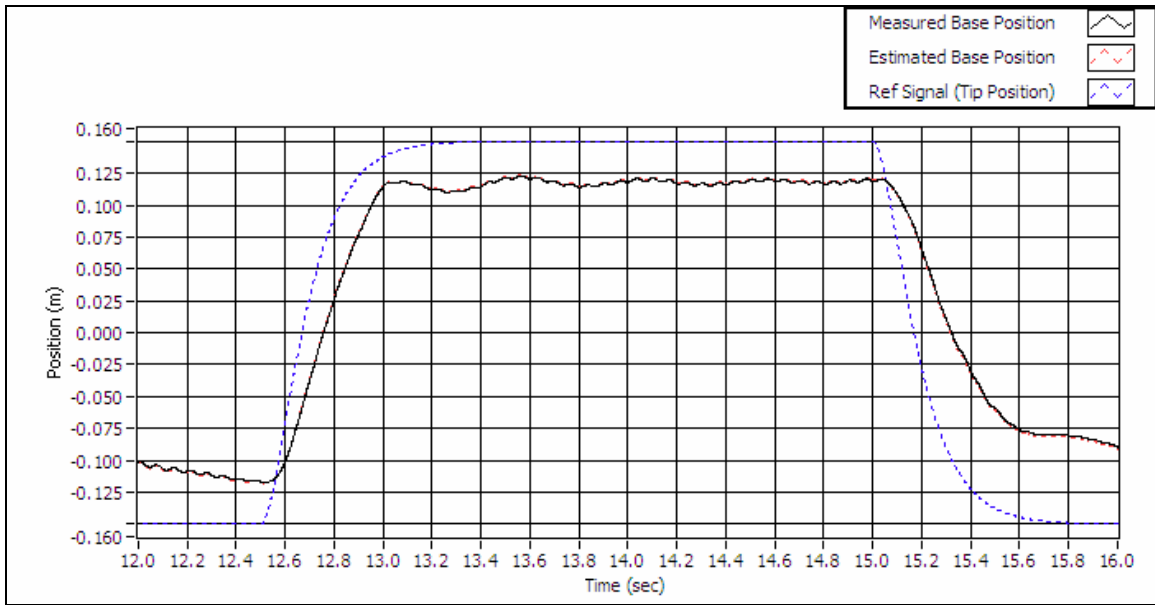
Figure 6.16: With link length increased by 91% (from 0.32m to 0.61m), measured and estimated base position during tracking of a reduced-rate square wave with regulator (τ = 0.5e9) and Kalman filter, at an execution rate of 1khz. This figure shows tracking capability of the closed-loop system is more severely affected with modeling error in link length than in tip mass. (Measured and estimated signals almost entirely overlaid)
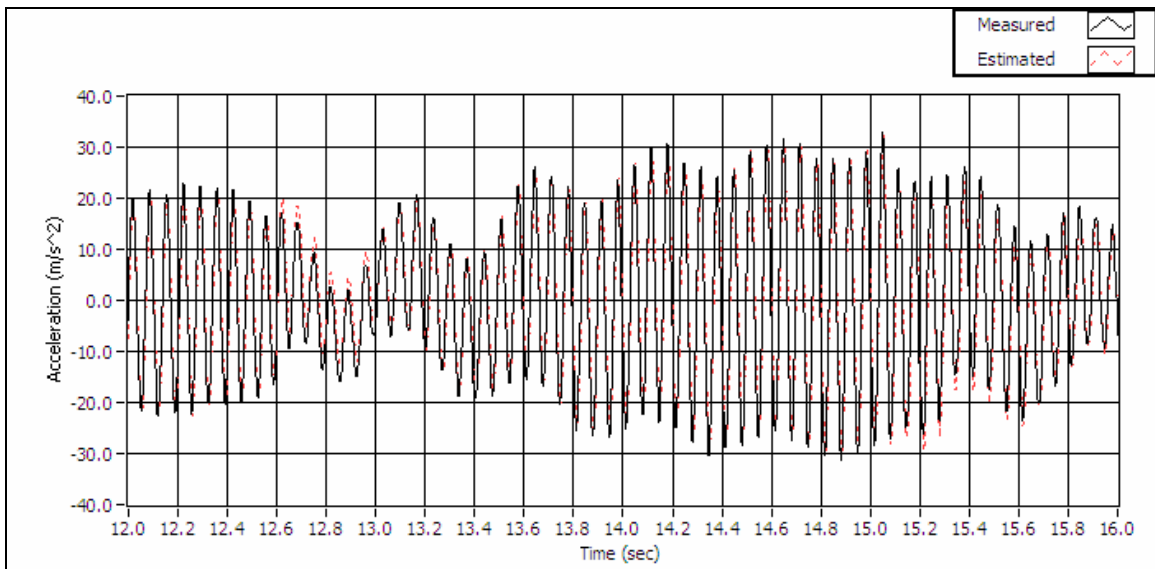
Figure 6.17: With link length increased by 91% (from 0.32m to 0.61m), measured and estimated tip acceleration during tracking of a reduced-rate square wave with regulator (τ = 0.5e9) and Kalman filter, at an execution rate of 1khz. This figure shows the commanded tip position is only marginally stable under closed-loop control with significant modeling error in link length.

94
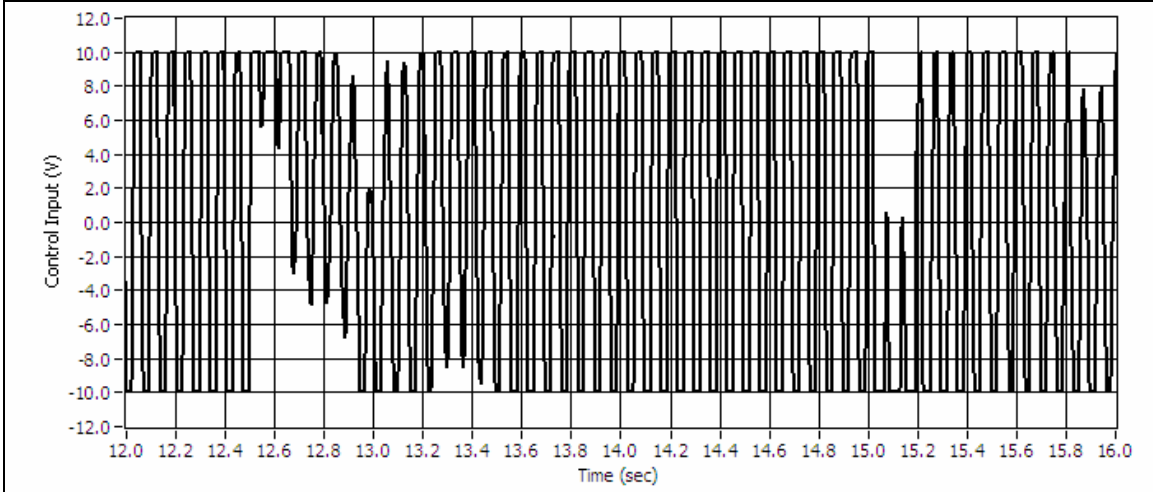
Figure 6.18: With link length increased by 91% (from 0.32m to 0.61m), corresponding control input during tracking of a reduced-rate square wave with regulator ($\tau = 0.5e9$) and Kalman filter, at an execution rate of 1khz. This figure shows severe motor saturation results as closed-loop control unsuccessfully tries to stabilize the commanded tip position with significant modeling error in link length.

6.4 Robust Observer

Given the marginally stable closed-loop system with modeling error in link length as depicted in Figures 6.16 through 18, the goal of robust observer design is to directly improve state estimates and thus indirectly improve tip tracking performance and stability. In an approach similar to simulations, the first sliding mode observer parameter to select is Q_p. Various values for Q_p were investigated. For instance, Q_p of 1.6e3, 8e3, 50e3, and 1.5e7 lead to $\underline{K}_s$ with a largest element of 4.5e3, 893, 143, and 0.48, respectively. The choice for Q_p is indeed arbitrary because the parameter ρ is a multiplier on $\underline{K}_s$ as given by equation 4.25. Since Q_p requires more computation, it is preferable to fix the parameter off-line and vary ρ on-line. The parameter Q_p with value of 1.5e7 is selected and leads to a sliding mode gain

$$K_s = \begin{bmatrix} -1.2e-4 & -0.34 \\ -3.2e-8 & -4.5e-5 \\ 2.8e-4 & 0.48 \\ -1.1e-7 & -1.9e-4 \end{bmatrix}.$$

(6.4)

The next series of figures show that with Q_p fixed as discussed above, values of ρ > 5 produce estimate chatter, showing the influence of the discontinuous state term on the observer dynamics. The addition of the boundary layer filters out the estimate chatter as expected.
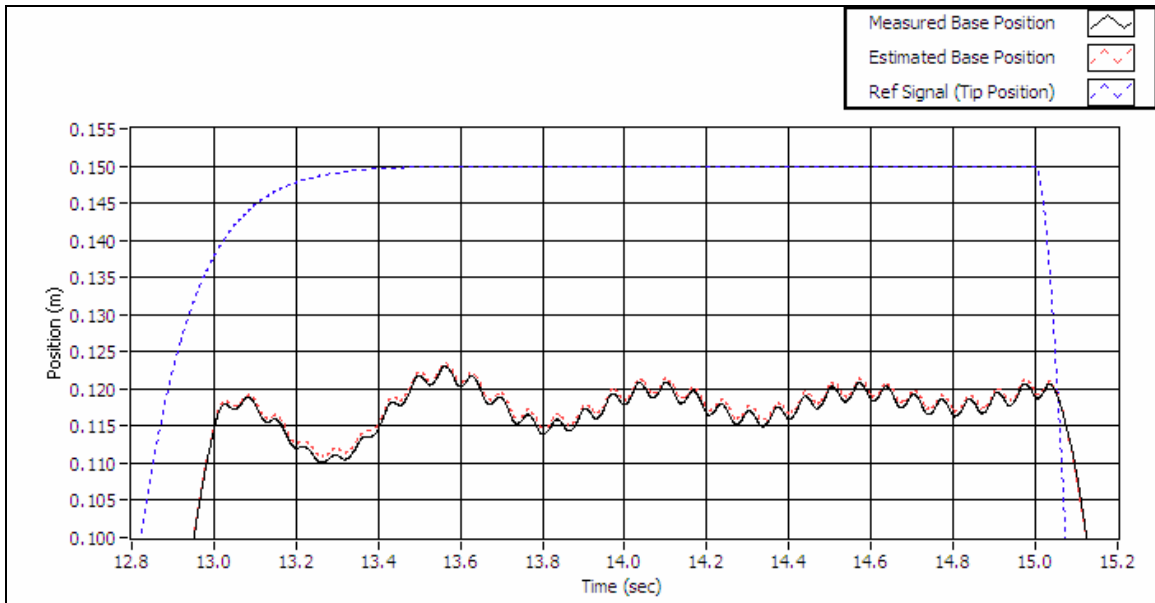
Figure 6.19: With link length increased by 91% (from 0.32m to 0.61m), measured and estimated base position during tracking of a reduced-rate square wave with regulator (τ = 0.5e9) and Kalman filter alone, at an execution rate of 1khz. This figure shows significant excitation in base motion and poor reference tracking due to modeling error in link length but it should be noted that estimates provided by Kalman filter remain accurate.
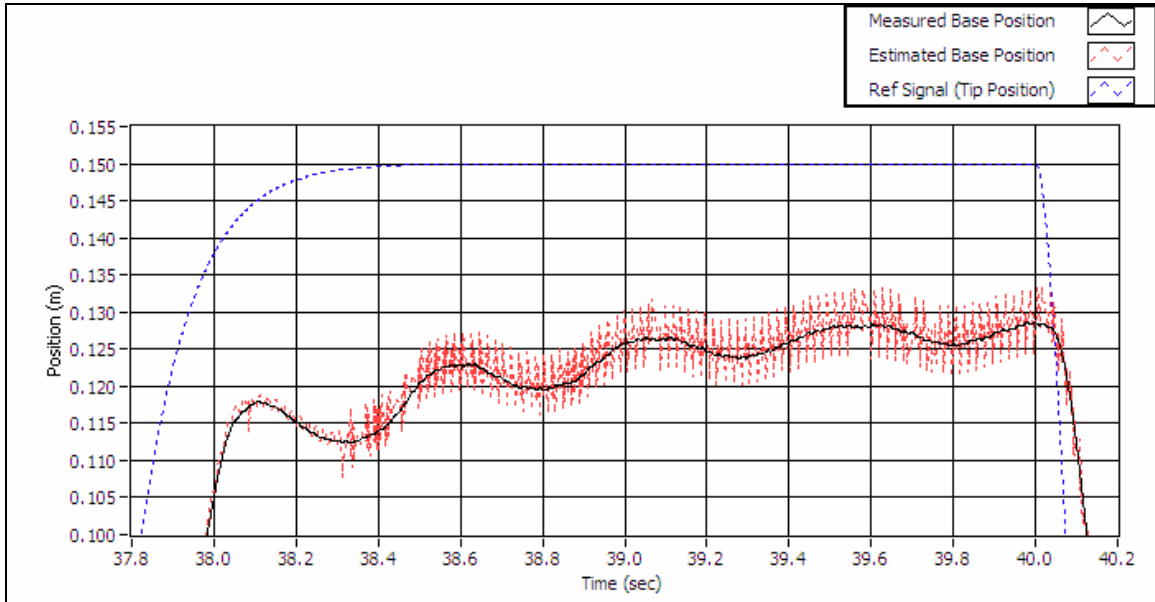
Figure 6.20: With link length increased by 91% (from 0.32m to 0.61m), measured and estimated base position during tracking of a reduced-rate square wave with regulator (τ = 0.5e9) and SMO (Q_p=1.5e7, ρ=10), at an execution rate of 1khz. This figure shows the appearance of estimate chatter as expected, along with a damping effect on the motor.
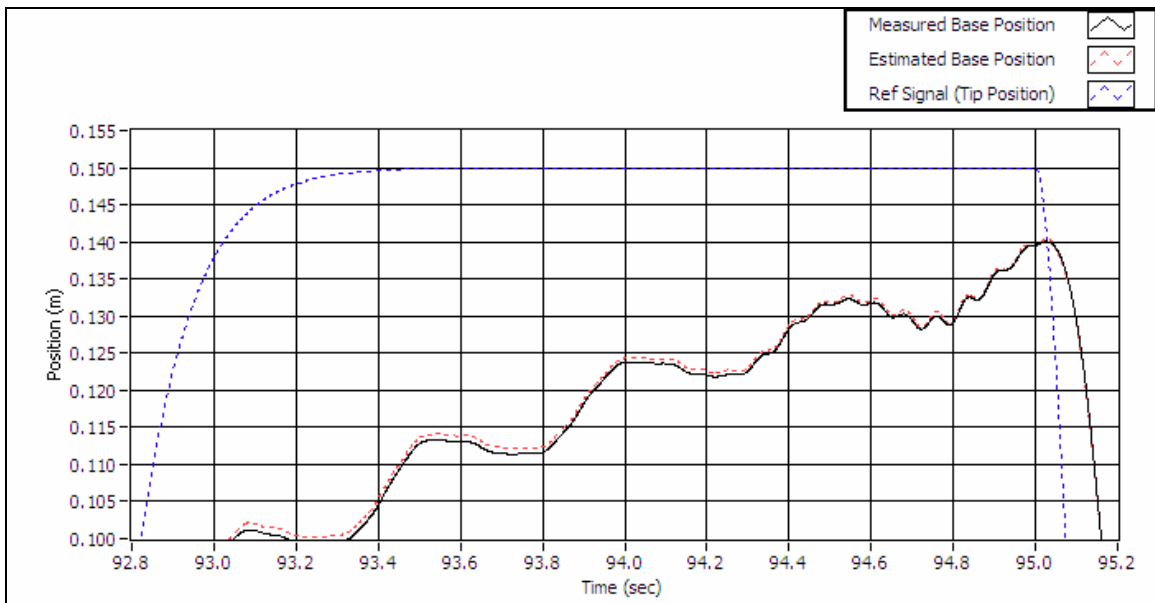
Figure 6.21: With link length increased by 91% (from 0.32m to 0.61m), measured and estimated base position during tracking of a reduced-rate square wave with regulator (τ = 0.5e9) and BLSMO (Q_p=1.5e7, ρ=10, λ=5), at an execution rate of 1khz. This figure shows absence of estimate chatter due to a boundary layer, now along with an even larger damping effect on the motor.

97
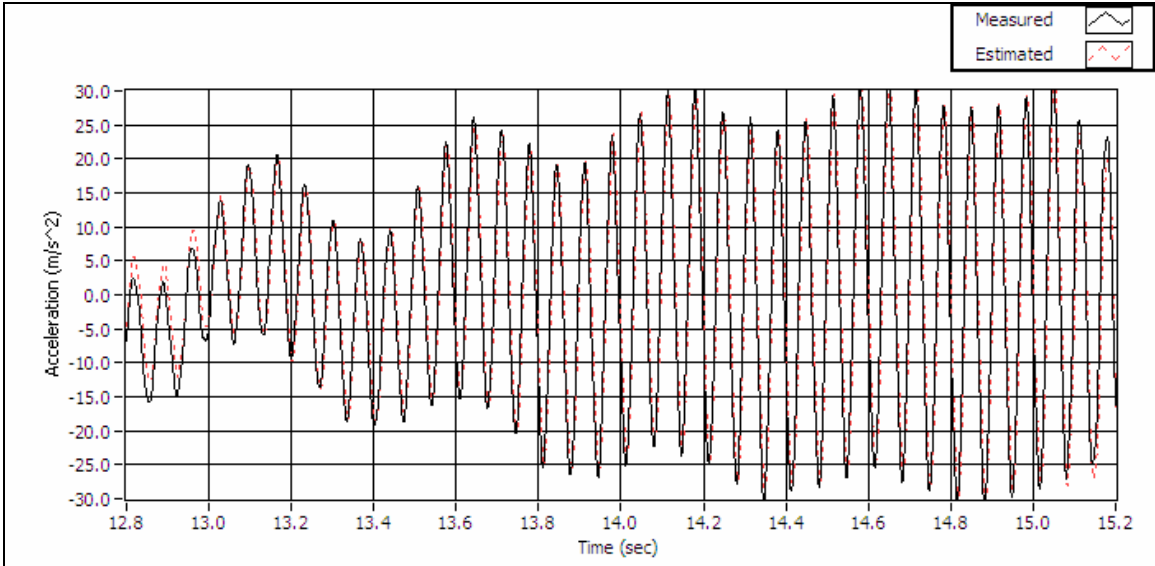
Figure 6.22: With link length increased by 91% (from 0.32m to 0.61m), measured and estimated base position during tracking of a reduced-rate square wave with regulator (τ = 0.5e9) and Kalman filter, at an execution rate of 1khz. This figure shows sustained, high frequency tip oscillations due to modeling error in link length but it should be noted that estimates provided by Kalman filter remain accurate.
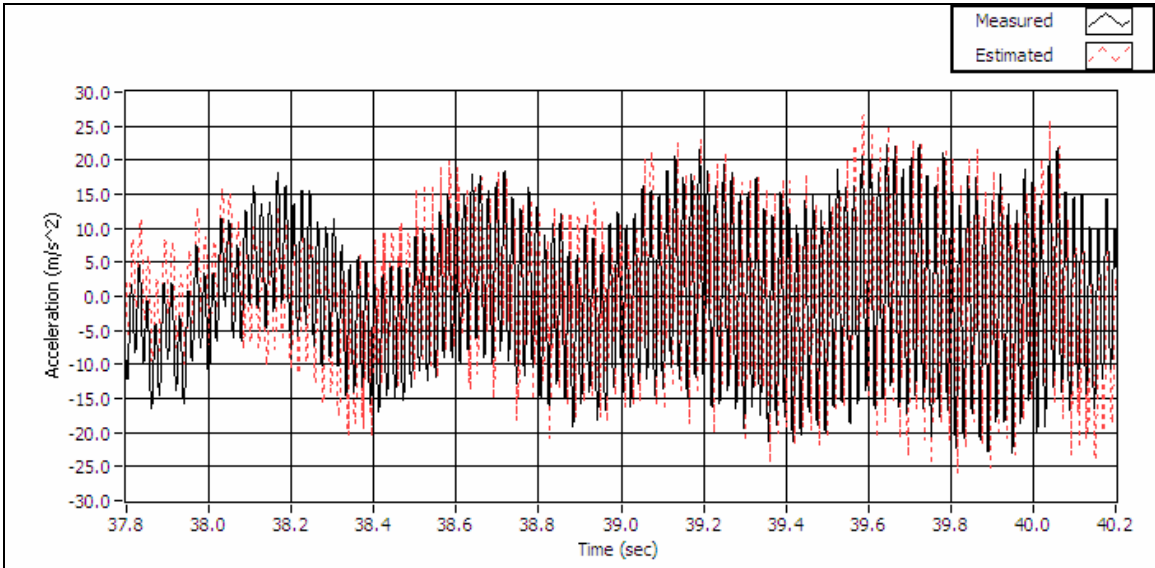
Figure 6.23: With link length increased by 91% (from 0.32m to 0.61m), measured and estimated base position during tracking of a reduced-rate square wave with regulator (τ = 0.5e9) and SMO (Q_p=1.5e7, ρ=10), at an execution rate of 1khz. This figure shows how damping of the base motor due to estimate chatter results in a noticeable decrease in magnitude of tip oscillations. (compare to Figure 6.22)
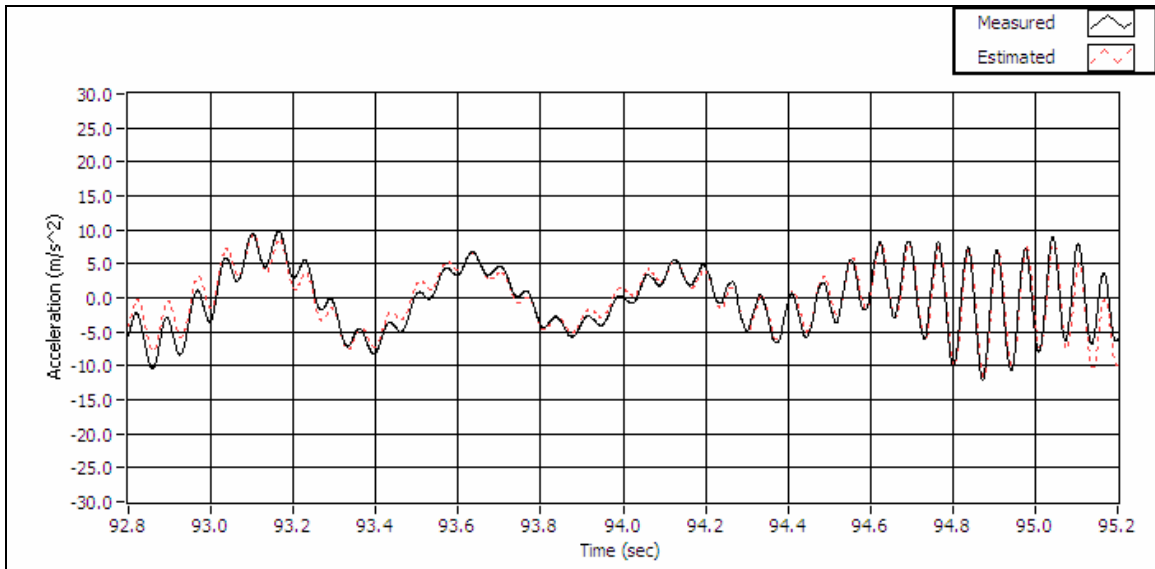
Figure 6.24: With link length increased by 91% (from 0.32m to 0.61m), measured and estimated base position during tracking of a reduced-rate square wave with regulator (τ = 0.5e9) and BLSMO (Q_p=1.5e7, ρ=10, λ=5), at an execution rate of 1khz. This figure shows how damping of the base motor resulting from use of a BLSMO results in a noticeable decrease in tip oscillations. (compare to Figure 6.22)
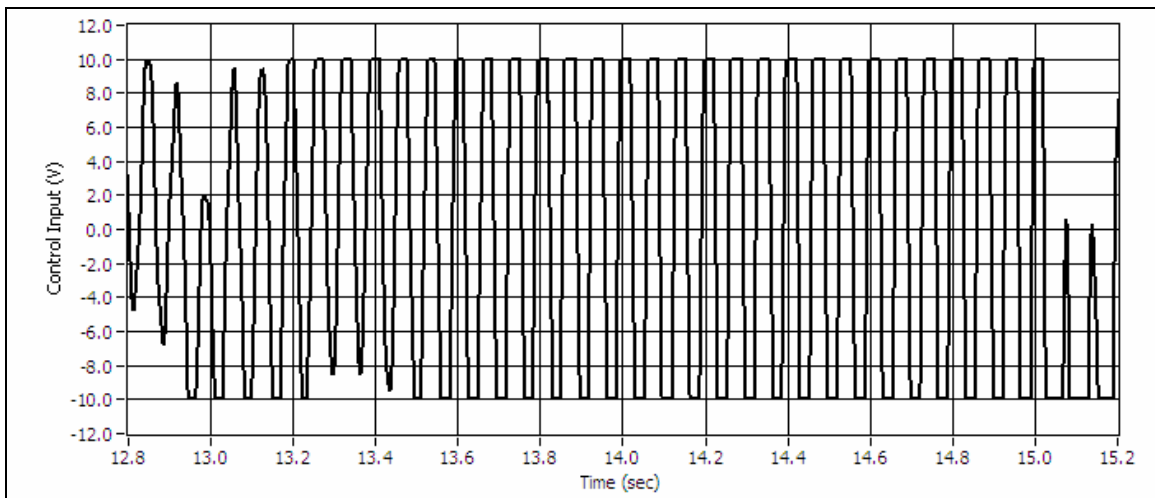
Figure 6.25: With link length increased by 91% (from 0.32m to 0.61m), measured and estimated base position during tracking of a reduced-rate square wave with regulator (τ = 0.5e9) and Kalman filter, at an execution rate of 1khz. This figure shows severe control input saturation in the presence of modeling error in link length and is one indication that loss of asymptotic stability may be due largely to a poor controller rather than poor estimates.
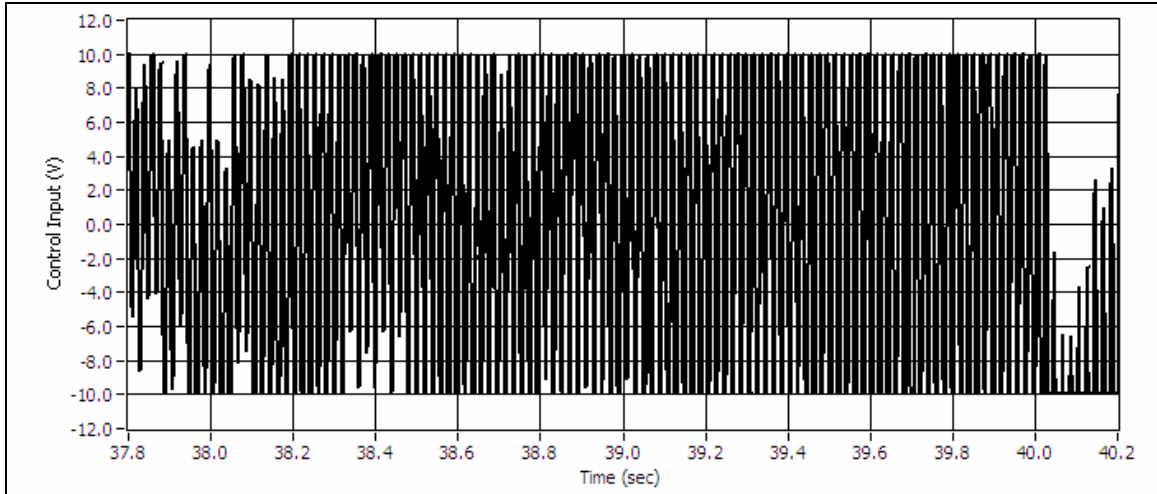
Figure 6.26: With link length increased by 91% (from 0.32m to 0.61m), measured and estimated base position during tracking of a reduced-rate square wave with regulator (τ = 0.5e9) and SMO (Q_p=1.5e7, ρ=10), at an execution rate of 1khz. This figure highlights the increased control activity due to estimate chatter.
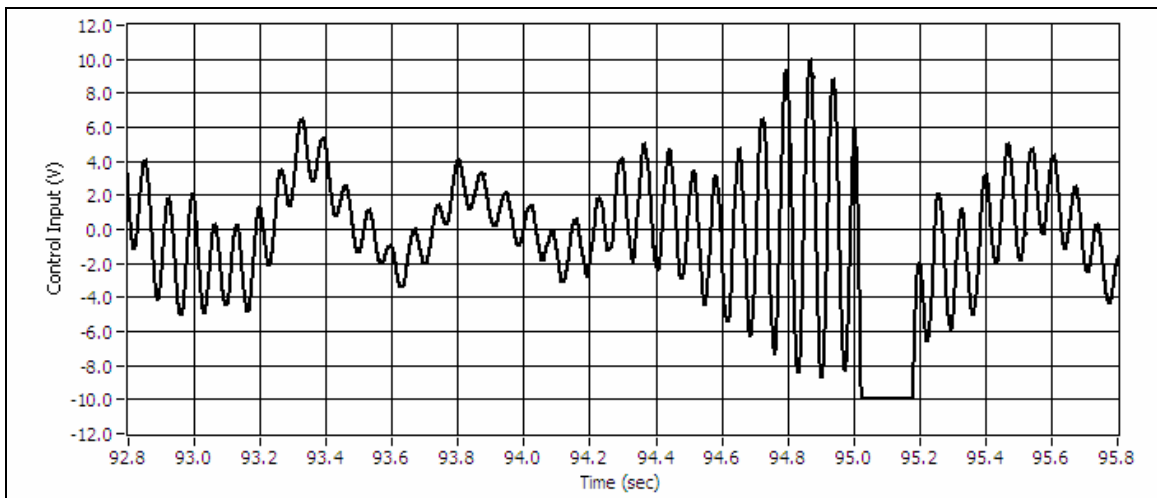
Figure 6.27: With link length increased by 91% (from 0.32m to 0.61m), measured and estimated base position during tracking of a reduced-rate square wave with regulator (τ = 0.5e9) and BLSMO (Q_p=1.5e7, ρ=10, λ=5), at an execution rate of 1khz. This figure highlights a dramatic decrease in control activity from removal of estimate chatter.

100
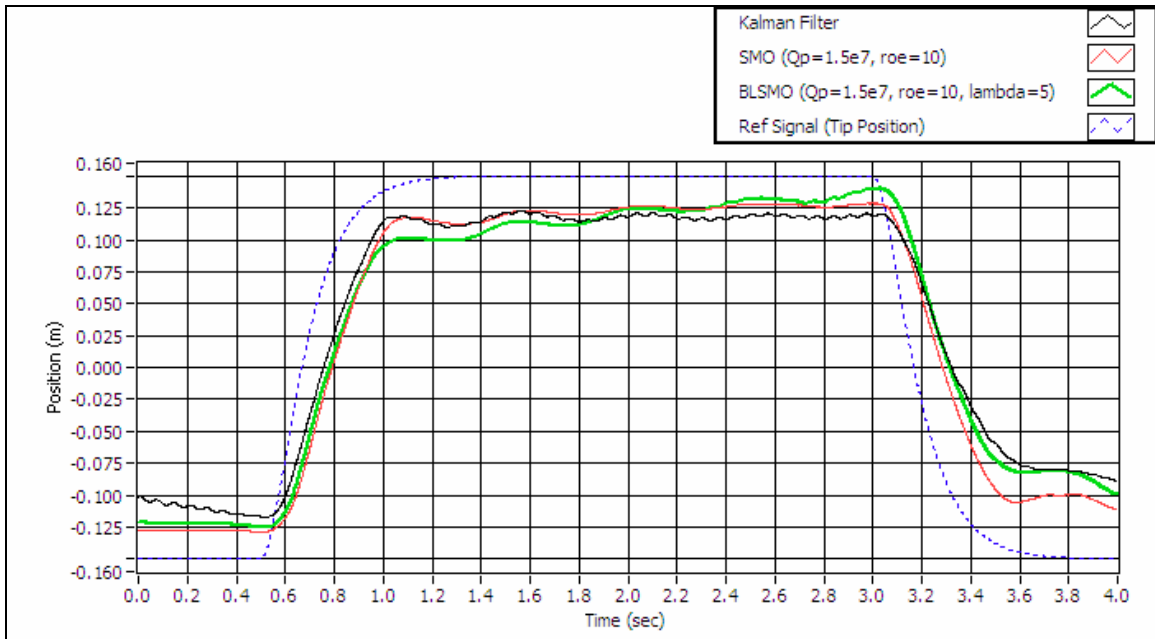
Figure 6.28: With link length increased by 91% (from 0.32m to 0.61m), measured and estimated base position during tracking of a reduced-rate square wave with regulator (τ = 0.5e9) and various observers at an execution rate of 1khz. This figure shows how use of SMO and BLSMO affects closed-loop performance.
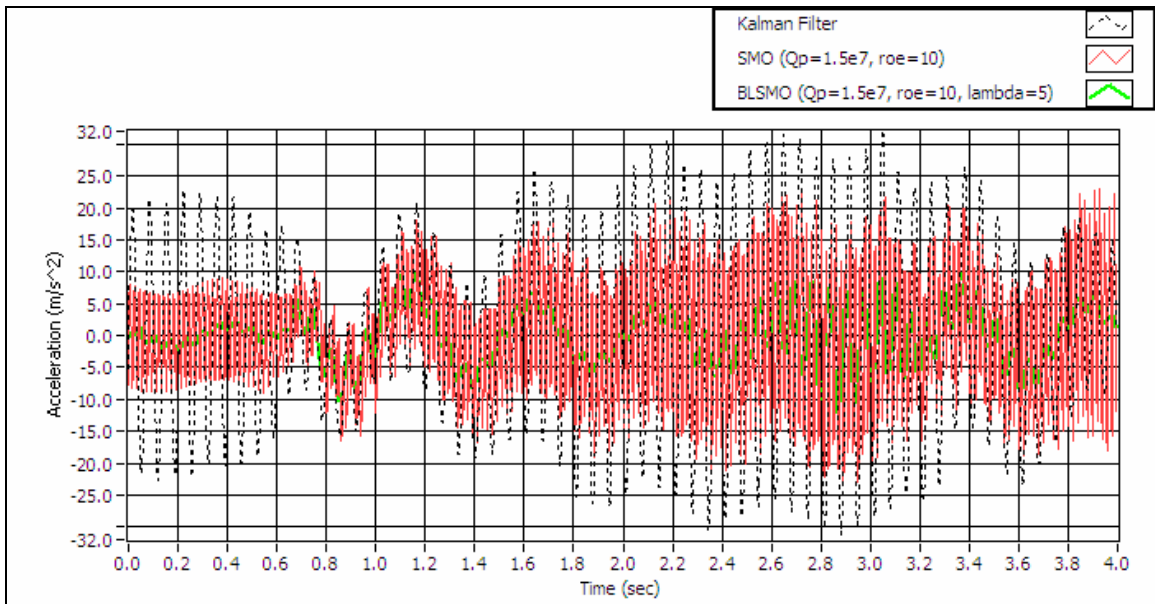
Figure 6.29: With link length increased by 91% (from 0.32m to 0.61m), measured and estimated tip acceleration during tracking of a reduced-rate square wave with regulator (τ = 0.5e9) and various observers at an execution rate of 1khz. This figure shows how use of SMO and BLSMO affects closed-loop performance.

Figures 6.19 through 6.24 have shown that replacing the Kalman filter with a SMO or BLSMO has damping effects on closed-loop performance. For the SMO, it appears that this damping of link base and tip motions is due to estimate chatter as seen in Figure 6.20. For the BLSMO, the damping appears to be due to damping in state estimates themselves which leads to damping of the control signal as seen in Figure 6.27 (recall the control action $u = Fr - \underline{K}_c \hat{\underline{x}}$ where $\underline{K}_c$ as given by equation 6.2 is fairly large). Experiments show as boundary layer thickness decreases, the damping effect increases and tip vibrations are further suppressed while reference tracking degrades.

A notable observation from the study is that estimates provided by the Kalman filter in the presence of the rather significant parameter variation at hand remain accurate. This leads to the conclusion that marginal stability of the closed-loop system at the case in hand may be attributed largely to the degraded performance of the controller due to modeling error rather than degraded performance of the observer.

6.5 Implementation Challenges and Recommendations

It was discovered that the large gains (1,2) and (3,2) in the sliding mode gain $\underline{K}_s$ given in equation 6.4 in combination with $\rho > 50$ cause excessively large estimate corrections which in certain circumstances can lead to spikes in the control signal and thus erratic closed-loop control. The sequence of events can be seen in Figure 6.30. Close investigation reveals the problem begins with an excessively large correction on $\hat{x}_1$ and $\hat{x}_3$ by the discontinuous state function $\underline{K}_s(\text{sgn}(\underline{y} - \hat{\underline{y}}))$ in the observer dynamic equation. In the same time-step, this abrupt change leads to an abrupt change in $\hat{y}_2$, the tip estimate, because of the relatively large elements (2,1) and (2,3) of

$$\underline{C} = \begin{bmatrix} 0 & 0 & 1 & 0 \\ -1.195e3 & -0.391 & 1.195e3 & -0.391 \end{bmatrix}. \tag{6.5}$$

t	r	y1	u	y2	yhat1	yhat2	xhat1	xhat2	xhat3	xhat4
22.673	0.004804	-0.189299	78.5	-4.44188	-0.191162	-4.40095	-0.188653	-15.5629	-0.191162	19.1529
22.674	0.005722	-0.188673	78.5	-4.50676	-0.190538	-4.45457	-0.187987	-15.5685	-0.190538	19.1699
22.675	0.006636	-0.188044	78.5	-4.66108	-0.189936	-4.53711	-0.18732	-15.5742	-0.189936	19.1869
22.676	0.007547	-0.187407	78.5	-4.79009	-0.18925	-4.51465	-0.186657	-15.58	-0.18925	19.204
22.677	0.008453	-0.186761	78.5	-4.93692	-0.141817	88.5724	-0.217155	-15.574	-0.141817	19.2122
22.678	0.009356	-0.186112	78.5	-5.02875	-0.152325	78.1474	-0.21893	-15.5364	-0.152325	19.1591
22.679	0.010254	-0.185455	78.5	-5.03439	-0.159448	69.5327	-0.21884	-15.4965	-0.159448	19.112
22.68	0.011149	-0.184789	78.5	-4.99444	-0.164375	62.5849	-0.217951	-15.4557	-0.164375	19.0715
22.681	0.01204	-0.184116	78.5	-4.79666	-0.167794	57.1134	-0.21679	-15.4145	-0.167794	19.0333

Figure 6.30: Example #1 of discontinuity in estimates. This figure depicts the sequence of events that leads to estimate spikes which lead to erratic closed-loop control.

The meaning of all of this is that this phenomena places an upper bound on the parameter ρ which may be hindering observer tuning. Simulations showed that due to the discontinuous nature of the sliding mode terms in the observer dynamics, unlike the Kalman gain, increasing the sliding mode gain eventually destabilizes error dynamics. However, the upper bound placed on ρ by this phenomena is a premature upper bound which may be hindering the sliding mode behavior.

A similar phenomena occurs in the implementation of boundary layer versions of the sliding mode observer. It was discovered that small boundary layer widths, $\lambda < 1$, leads to a spike in the control signal as shown in Figure 6.31. In a similar fashion as earlier, the sequence of events is traced to excessive corrections to state estimates by the discontinuous state function. Discontinuity in estimates in conjunction with the large gains 1.01e4 and 3.25e6 in $\underline{K}_c$, given by equation 6.2, lead to control signal spikes.

t	r	y1	u	y2	yhat1	yhat2	xhat1	xhat2	xhat3	xhat4
23.188	0.147569	0.129029	8.15552	0.352176	0.130422	1.69121	0.128673	3.25724	0.130422	-2.24092
23.189	0.147591	0.129081	8.25649	0.331768	0.130468	1.65878	0.128747	3.25794	0.130468	-2.24245
23.19	0.147612	0.129129	8.62489	0.293737	0.130511	1.62247	0.128821	3.25861	0.130511	-2.24395
23.191	0.147632	0.129177	8.57797	0.279705	0.130571	1.61049	0.128891	3.25925	0.130571	-2.24537
23.192	0.147653	0.129225	-78.5	0.252617	0.130605	1.55824	0.128969	3.25987	0.130605	-2.24683
23.193	0.147673	0.12927	78.5	0.218764	0.131911	4.37158	0.127921	3.26083	0.131911	-2.2502
23.194	0.147694	0.129314	78.5	0.21137	0.127306	-6.18932	0.132155	3.25903	0.127306	-2.24188
23.195	0.147714	0.129362	78.5	0.167104	0.12691	-9.19299	0.134269	3.25455	0.12691	-2.22765
23.196	0.147734	0.12941	70.6087	0.156345	0.127894	-8.84281	0.134957	3.24653	0.127894	-2.20796

Figure 6.31: Example #2 of discontinuity in estimates. This figure depicts the sequence of events that leads to estimate spikes which lead to erratic closed-loop control.
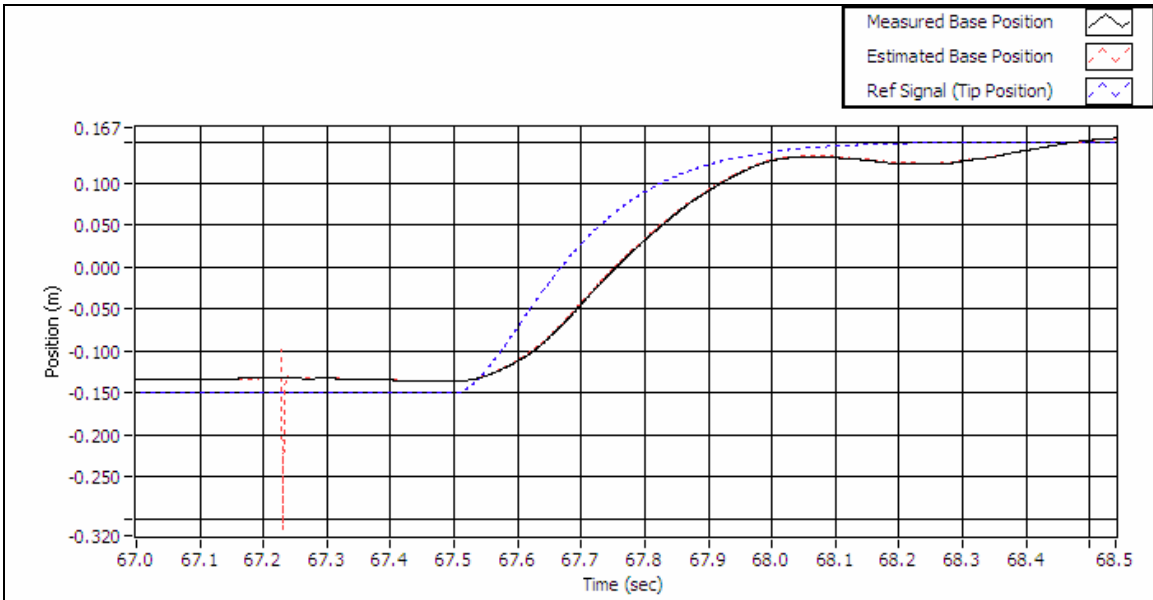
Figure 6.32: With link length increased by 91% (from 0.32m to 0.61m), measured and estimated base position during tracking of a reduced-rate square wave with regulator ($\tau = 0.5e9$) and BLSMO ($Q_p=1.5e7$, $\rho=10$, $\lambda=1$), at an execution rate of 1khz. This figure shows a discontinuity in state estimates.

A third implementation challenge is estimate chatter leading to control signal chatter as is apparent in Figure 6.26. During experiments, the high control activity caused the motor to overheat causing insulation around the motor coil to expand. Precautions must be taken when tuning a robust observer on a real system.

With consideration of these limitations, the general approach used in tuning the three observer parameters is outlined in Table 6.4. The six steps outlines a basic sequence and show that there exists a structure to the process of tuning the robust observer. There are obvious dependencies between the parameters of the sliding mode observer, and these have become clearer to the author only after simulations and physical experiments. For instance, it is most convenient to fix the parameter Q_p off-line since it requires significant computation and then tune the parameter ρ on-line. The application of the observer to a physical system has provided further insight into how the dynamics of the observer are governed by each parameter as well as how the model structure can influence the behavior of the robust observer. For instance, when implementing the observer on a physical system, it becomes especially important to consider the size of estimate corrections, since excessively large estimate corrections can lead to an erratic control signal. The structure of the output matrix $\underline{C}$ can amplify any drastic corrections in state estimates and create a domino effect which eventually affects the performance of the closed-loop system.

Table 6.4: An approach for tuning the robust observer (based on a Kalman filter) on the experimental setup.

	Step	Observations
1.	Find the Kalman gain $\underline{K}_L$.	
2.	Select the arbitrary positive-definite symmetric Q_p.	Assume Q_p has repeated roots for convenience. The limitation of this approach is that selection of Q_p will then only affect $\lVert \underline{K}_s \rVert$. That is, the designer will only have control over $\underline{K}_s$ as a whole, not the individual gains.
3.	Find $\underline{A}$-$\underline{K}_L\underline{C}$ and solve the Lyapunov matrix equation for a unique positive-definite symmetric $\underline{P}$.	Use computer solvers to solve the Lyapunov matrix equation.
4.	Find $\underline{K}_s = \underline{P}^{-1}\underline{C}^T$	$\underline{K}_s$ is fixed off-line.

		Table 6.4 (continued).
5.	Select ρ. Start small and increase.	Take into consideration the gains in $\underline{K}_s$ and the units of states to be estimated. In this way, you can avoid large values for ρ which gives unreasonably large corrections to state estimates. Smaller ρ reduces amount of estimate correction, however keep in mind that for sliding to occur, $\rho \geq \left\| \underline{\xi} \right\|$ (refer to chapter 4). This parameter is most conveniently tuned online.
6.	Select λ. Start large and decrease.	Estimate chatter is removed. Decreasing λ has an increasing damping effect on closed-loop system performance. This parameter is most conveniently tuned online.

CHAPTER 7

CONCLUSIONS AND RECOMMENDATIONS

7.1 Conclusions

This work presents the development and design of a robust nonlinear observer for general linear systems with model uncertainty in the form of parametric uncertainty. Two observer design approaches are reviewed, the variable structure systems theory approach and the Lyapunov approach. The challenges and limitations of each approach are discussed. The variable structure systems theory approach poses more significant challenges, such as the difficulty in determining sliding mode gains when model measurement outputs are a combination of multiple states. The Lyapunov approach is adopted for observer design and robustness studies based on simulations of a non-minimum phase closed-loop control system with model inaccuracy are undertaken.

For the most part, simulations verify the robustness properties of the sliding mode observer touted by other works. Most state estimates produced by the robust observer in the presence of parameter uncertainty are in fact reduced when compared to estimates from a Kalman filter, both with and without measurement noise. Estimates provided by boundary layer versions of the robust observer are found to be superior to observers lacking the boundary layer. In addition, performance of various boundary layer robust observer designs is found to converge, indicating an ease of finding the optimal observer parameters. Simulations show how improved estimation can lead to better reference tracking in the closed-loop system, with reduced tip excitation during motion, under conditions of "mild" uncertainty. In conditions of "severe" uncertainty, the loss of asymptotic and marginal stability with use of the Kalman filter occurs at a parameter

variation of 21%. With use of the robust observer, it is found that the closed-loop system remains asymptotically stable with a parameter variation up to 32%.

Some concerns about the design of the robust observer have surfaced during simulation. Simulations show that with use of the detailed system model, based on the assumed modes method, no benefits in terms of improved performance or improved stability of closed-loop control with the robust observer are found. A few possible factors for this result are discussed in Chapter 5. Another notable concern is the difficulty in selecting the robust observer design parameter ρ based on the upper bound on time varying uncertainty. The author is unable to calculate the lower bound on ρ based on uncertainty and instead uses a trial-and-error approach which seems effective although inefficient.

Experiments are conducted on a physical system consisting of a single flexible link with non-collocation of actuators and sensors. The robust observer is successfully implemented in the National Instruments LabVIEW programming environment at control loop rates exceeding 1khz. The focus of experiments is on investigating questions regarding robust observer implementation. Specifically, the approach used for initializing certain observer design parameters off-line and tuning others on-line at run-time and the effects of the design parameters on the observer dynamics as well as on the physical system are discussed.

On the physical system, it is found that one of the three parameters can be fixed off-line and is indeed arbitrary. The other two parameters are tuned on-line in a trial and error manner. The physical system was found to be very sensitive to changes in observer parameters, indicating that care should be taken when tuning on-line when actual hardware is involved. Robust estimation performance shown by simulations could not be verified with experiments due to the limitations imposed on observer parameters. Specifically, the structure of the output matrix $\underline{C}$ in combination with large sliding mode gain $\underline{K}_s$ and large feedback gain $\underline{K}_c$ leads to discontinuities in the estimates themselves

which in turn affect the control signal. Operating within the restricted bounds on observer parameters, experiments do show that replacing the Kalman filter with a SMO or BLSMO has clear damping effects on closed-loop performance.

So what is the final word on the robust observer? Optimality may imply "best" estimates but that does not translate into a "best" observer. If we consider useful criteria for judging the worth of an observer to be accuracy, robustness, ease of design and ease of implementation, then the sliding mode observer scores high based on simulations. Choosing an appropriate suboptimal design for the observer is one approach for reducing the sensitivity to model uncertainty. Simulations of the sliding mode observer show an alternative, in that optimality is not sacrificed for robustness. Optimality of the estimates provided by the robust observer does not suffer in conditions of low uncertainty with proper design. In the worse case scenario, since the observer design can be based on the Kalman filter, the observer can easily revert to one that functions as a Kalman filter alone by switching off the discontinuous control function, including in real-time. The observer also scores high due to robustness to parameter uncertainty and relative ease of tuning the three key observer design parameters, that is, once the designer understands the effects of each parameter on observer dynamics.

Having said that, the sliding mode observer does not score as high based on experimental results. The sliding mode observer proved more difficult to implement on the physical system than the Kalman filter. First, tuning of two of the three parameters on a physical system is done by trial and error and seems too much of an art than a science. Second, estimate chatter can negatively affect the control signal and cause harm to hardware. Notable qualities of the sliding mode observer are that it can be implemented at fast control rates, can be tuned on-line, and the sliding mode part of the observer can be easily switched off resulting in just a steady-state Kalman filter.

7.2 Contributions

The main contribution of this thesis work is a comprehensive study of robustness of closed-loop control with a robust nonlinear observer and an optimal observer to parametric uncertainty. The simulation study includes various levels of parameter variation, multiple linear system models, multiple robust observer designs, and the effect of measurement noise. The study of closed-loop control of a non-collocated system with non-minimum phase behavior is a significant aspect of this contribution.

This work outlines the approaches used in tuning the observer designs in both simulations and on a physical system. The outline summarizes the basic sequence of steps involved and emphasizes that there is a structure to the process which can be repeated by others to replicate and improve on this work. A National Instruments LabVIEW application has been created that gives the designer the ability to tune robust observer parameters at run-time, including the capability of switching between an optimal observer and the robust observer on the fly. The intuitive nature of the LabVIEW programming environment coupled with a well documented VI makes it arguably easier for others to continue this work.

7.3 Recommendations for Future Work

The first obvious recommendation is to modify the measurement model by changing the structure of the output matrix $\underline{C}$. Tip position should replace the tip acceleration output from the model. Measured tip acceleration will then have to be integrated to reach tip position or the position measured directly. If acceleration is to be integrated, the issue that must be resolved is accelerometer drift.

The second recommendation is to design the Kalman filter by not penalizing all states equally in the process noise covariance matrix. Each element of the diagonal matrix should reflect both the sources of uncertainty and the units of the states themselves. This suggestion also applies to the design of the observer design parameter $\underline{Q}_p$ in the

Lyapunov based observer design approach applied in this work. The recommendation is to weight elements of $\underline{Q}_p$, the input into the matrix Lyapunov equation, individually instead of assuming $\underline{Q}_p$ has repeated roots. This will also give the designer the ability to change the mix of gains in the sliding mode gain $\underline{K}_s$. The advantages of this alternative approach needs to be studied.

The third recommendation is to revisit the variable structure systems theory approach. The pole placement approach to sliding mode gain selection has now become an attractive aspect of that approach. It gives more control over individual gains which may prove very useful, although still cumbersome. This work showed that the approach identified by Chalhoub is manageable for lumped parameter models in which states are direct outputs of the system. The author recommends against adapting this approach for the assumed modes method model for the reasons discussed in Chapter 4.

How can direct tip position measurements help in improving control? Position measurements obtained using a vision system can supplement the tip acceleration and base position measurements already considered by the observer. This does pose a design challenge since the Lyapunov approach to robust observer design is based on the output matrix $\underline{C}$. In the case of multi-rate sensors, the structure of $\underline{C}$ may be time-varying and the implications of this need to be studied.

APPENDIX A

METHOD OF SYMMETRIC ROOT LOCUS

The method of symmetric root locus allows the designer to tune a single parameter, τ in the performance index

$$J = \int_0^\infty [\tau y^2(t) + u^2(t)]dt \tag{A.1}$$

where $y^2(t)$ and $u^2(t)$ are tracking error and control effort, respectively. Note that it is up to the designer to define the output matrix $\underline{C}$ of the state-space system which will determine the states to be penalized for the purpose of minimizing error. Then, the stable roots of the root locus equation (those in the left half plane)

$$1 + \tau \frac{N(-s)N(s)}{D(-s)D(s)} = 0 \tag{A.2}$$

are to be the closed-loop poles placed by the control gain K in the control law

$$u = -\underline{K}\underline{x} \tag{A.3}$$

A complete overview of the procedure is provide by Kailath [16].

APPENDIX B

INTRODUCING THE NON-ZERO REFERENCE

The feed-forward gain used in this work is determined by computing the steady state values of the state and control input that will result in zero output error. This is accomplished by finding the matrices $\underline{N}_x$ and $\underline{N}_u$ in

$$x_{ss} = N_x r_{ss} \tag{B.1}$$

and

$$u_{ss} = N_u r_{ss} \tag{B.2}$$

such that

$$y_{ss} = r_{ss}. \tag{B.3}$$

Franklin provides the matrix equation

$$\begin{bmatrix} \underline{N}_x \\ \underline{N}_u \end{bmatrix} = \begin{bmatrix} \underline{A} & \underline{B} \\ \underline{C} & \underline{D} \end{bmatrix}^{-1} \begin{bmatrix} 0 \\ 1 \end{bmatrix} \tag{B.4}$$

for determining $\underline{N}_x$ and $\underline{N}_u$ [17].

The feedforward gain $\underline{N}$ can then be determined from

$$\underline{N} = \underline{N}_u + \underline{K}\underline{N}_x \tag{B.5}$$

where $\underline{K}$ is the feedback gain.

APPENDIX C

VERIFICATION BY TRANSFER MATRIX METHOD

The transfer matrix relates the variables

$$
\begin{bmatrix} -W \\ \psi \\ M \\ V \end{bmatrix} = \begin{bmatrix} -displacement \\ angle \\ moment \\ shear\_force \end{bmatrix}
\tag{C.1}
$$

at the guided end to the free end of the link. For a single link with these boundary conditions and in flexure only with a point mass at the free end, the relationship between the two ends is given as

$$
\begin{bmatrix} -W \\ 0 \\ M \\ 0 \end{bmatrix}_0 = BR \begin{bmatrix} -W \\ \psi \\ 0 \\ 0 \end{bmatrix}_1
\tag{C.2}
$$

where B is the beam transfer matrix and R is the rigid mass transfer matrix. B and R matrices are based on parameters of the flexible link and are provided by Book [2]. This yields

$$
\begin{bmatrix} TM_{21} & TM_{22} \\ TM_{41} & TM_{42} \end{bmatrix} \begin{bmatrix} -W \\ \psi \end{bmatrix} = \begin{bmatrix} 0 \\ 0 \end{bmatrix}
\tag{C.3}
$$

where TM_{ij} are elements of BR. The eigenvalues (modes) are the values of the frequency variable ω obtained from

$$
\det \begin{bmatrix} TM_{21} & TM_{22} \\ TM_{41} & TM_{42} \end{bmatrix} = 0 .
\tag{C.4}
$$

114

Table C.1: Comparison of undamped modes predicted by assumed modes method and transfer matrix method.

	Assumed Modes Method	Transfer Matrix Method	% Difference
Flexible Mode #1 (rad/s)	57	49	16.3
Flexible Mode #2 (rad/s)	342	326	4.9
Flexible Mode #3 (rad/s)	1387	869	59.6

The following Matlab code plots the frequency variable ω. The intersections with the x-axis are the flexible undamped modes predicted by the transfer matrix method:

```
clear all ; close all ; clc ;
% Transfer matrix coefficients
w=sym('w');
E=2.0500e+011;
I=(1/12)*0.0399*0.0024^3;
L=0.4800;
mu=9.8375e+003*0.0399*0.0024;
m=0.5;
h=0.4800;
Lm=0.4800;
beta=( ((w^2)*(L^4)*mu)/(E*I) )^(1/4);
c0=(cosh(beta)+cos(beta))/2;
c1=(sinh(beta)+sin(beta))/(2*beta);
c2=(cosh(beta)-cos(beta))/(2*(beta^2));
c3=(sinh(beta)-sin(beta))/(2*(beta^3));
a=(L^2)/(E*I);

%Transfer matrix
B=[c0 -L*c1 a*c2 -a*L*c3;-((beta)^4)*(c3/L) c0 (a*c1)/L a*c2;((beta)^4)*(c2/a) -
((beta)^4)*((L*c3)/a) c0 -L*c1;-((beta)^4)*(c1/(a*L)) ((beta)^4)*(c2/a) -
((beta)^4)*(c3/L) c0];
```

```
R=[1 -Lm 0 0;0 1 0 0;m*(w^2)*(Lm-h) (-h*Lm+h^2)*(w^2)*m+I*(w^2) 1 -Lm;-
m*(w^2) h*m*(w^2) 0 1];
TM=B*R;
TMBC=[TM(2,1) TM(2,2);TM(4,1) TM(4,2)];


%Plot determinant
dt=det(TMBC);
tf=400;
t=[0;.01;tf];
ezplot(dt,t);
hold;
plot(t,t*0);
axis([0,tf,-10,10]);
```

APPENDIX D

VSS THEORY APPROACH EXAMPLE

To illustrate the ad-hoc nature of the variable structure systems theory approach for design of sliding mode gain $\underline{K}$, the following example is provided. Given the lumped parameter model

$$\underline{\dot{x}} = \begin{bmatrix} x_2 \\ f_2(x_1, x_2, x_3, x_4) \\ x_4 \\ f_4(x_1, x_2, x_3, x_4, u) \end{bmatrix} \tag{D.1}$$

with a single measurement, the flexible link tip position, given by

$$\underline{y} = \begin{bmatrix} 1 & 0 & 0 & 0 \end{bmatrix} \underline{x}, \tag{D.2}$$

then the observer state equations are given by

$$\dot{\hat{x}}_1 = \hat{x}_2 - L_1 \tilde{x}_1 - k_1 \operatorname{sgn}(\tilde{x}_1) \tag{D.3}$$

$$\dot{\hat{x}}_2 = \hat{f}_2 - L_2 \tilde{x}_1 - k_2 \operatorname{sgn}(\tilde{x}_1) \tag{D.4}$$

$$\dot{\hat{x}}_3 = \hat{x}_4 - L_3 \tilde{x}_1 - k_3 \operatorname{sgn}(\tilde{x}_1) \tag{D.5}$$

$$\dot{\hat{x}}_4 = \hat{f}_2 - L_4 \tilde{x}_1 - k_4 \operatorname{sgn}(\tilde{x}_1) \tag{D.6}$$

with the unknown gain matrices

$$\underline{L} = \begin{bmatrix} L_1 \\ L_2 \\ L_3 \\ L_4 \end{bmatrix} \tag{D.7}$$

and

$$\underline{K} = \begin{bmatrix} k_1 \\ k_2 \\ k_3 \\ k_4 \end{bmatrix}. \tag{D.8}$$

Design of the Kalman gain $\underline{L}$ is carried out first in the usual manner. The following procedure is used to determine the sliding mode gain $\underline{K}$.

The sliding surface is given by

$$s = \hat{x}_1 - x_1. \tag{D.9}$$

The rate of change of estimate error is given by

$$\dot{s}_1 = \dot{\hat{x}}_1 - \dot{x}_1 \tag{D.10}$$

$$= \hat{x}_2 - L_1\tilde{x}_1 - k_1 \operatorname{sgn}(\tilde{x}_1) - x_2 \tag{D.11}$$

$$= \tilde{x}_2 - L_1\tilde{x}_1 - k_1 \operatorname{sgn}(\tilde{x}_1). \tag{D.12}$$

Evaluating the sliding condition to generate a constraint equation on $\underline{K}$,

$$s_i \dot{s}_i \le -\eta |s_i| \tag{D.13}$$

gives

$$\tilde{x}_1(\tilde{x}_2 - L_1\tilde{x}_1 - k_1 \operatorname{sgn}(\tilde{x}_1)) \le -\eta |\tilde{x}_1| \tag{D.14}$$

which is reduced to

$$k_1 \operatorname{sgn}(\tilde{x}_1) \ge \frac{\eta |\tilde{x}_1|}{\tilde{x}_1} + \tilde{x}_2 - L_1\tilde{x}_1. \tag{D.15}$$

Since

$$\frac{|\tilde{x}_1|}{\tilde{x}_1} = \operatorname{sgn}(\tilde{x}_1) \tag{D.16}$$

and

$$\frac{\tilde{x}_1}{\operatorname{sgn}(\tilde{x}_1)} = |\tilde{x}_1|, \tag{D.17}$$

$$k_1 \geq \eta + \frac{\tilde{x}_2}{\text{sgn}(\tilde{x}_1)} - L_1 |\tilde{x}_1|. \tag{D.18}$$

Note that η is a user defined parameter. To generate more constraint equations on $\underline{K}$, the reduced order observer error dynamics

$$\dot{\underline{\tilde{x}}} = (\underline{I} - \underline{K}(\underline{C}\underline{K})^{-1}\underline{C})\Delta\underline{f} \tag{D.19}$$

are evaluated and give

$$\dot{\underline{\tilde{x}}} = \begin{bmatrix} 0 & 0 & 0 & 0 \\ -\dfrac{k_2}{k_1} & 1 & 0 & 0 \\ -\dfrac{k_3}{k_1} & 0 & 1 & 0 \\ -\dfrac{k_4}{k_1} & 0 & 0 & 1 \end{bmatrix} \begin{bmatrix} \tilde{x}_2 \\ \Delta f_2 \\ \tilde{x}_4 \\ \Delta f_4 \end{bmatrix} \tag{D.20}$$

which can be rewritten into a homogenous part and a perturbation part as

$$\dot{\underline{\tilde{x}}} = \begin{bmatrix} 0 & 0 & 0 & 0 \\ 0 & -\dfrac{k_2}{k_1} & 0 & 0 \\ 0 & -\dfrac{k_3}{k_1} & 0 & 1 \\ 0 & -\dfrac{k_4}{k_1} & 0 & 0 \end{bmatrix} \begin{bmatrix} \tilde{x}_1 \\ \tilde{x}_2 \\ \tilde{x}_3 \\ \tilde{x}_4 \end{bmatrix} + \begin{bmatrix} 0 & 0 \\ 1 & 0 \\ 0 & 0 \\ 0 & 1 \end{bmatrix} \begin{bmatrix} \Delta f_2 \\ \Delta f_4 \end{bmatrix}, \tag{D.21}$$

where Δf_2 and Δf_4 are perturbations due to parameter uncertainty given by

$$\Delta f_2 = \hat{f}_2 - f_2 \tag{D.22}$$

and

$$\Delta f_4 = \hat{f}_4 - f_4. \tag{D.23}$$

Since k_1 must be positive, the constraint is modified to

$$k_1 \geq \eta + |\tilde{x}_2| + |L_1\tilde{x}_1|. \tag{D.24}$$

119

With k_1 assured positive, k_2 must be positive to ensure asymptotically stable dynamics of the homogeneous part. When each row of the reduced order observer error dynamics is expanded, the following three constraint equations result:

$$k_2 = k_1 \frac{\Delta f_2}{\tilde{x}_2} \tag{D.25}$$

$$k_3 = k_1 \frac{\tilde{x}_4}{\tilde{x}_2} \tag{D.26}$$

$$k_4 = k_1 \frac{\Delta f_4}{\tilde{x}_2} . \tag{D.27}$$

With four constraint equations available and four unknown gains to determine. $\underline{K}$ can now be fully determined. That is, after upper bounds not only on the perturbation terms Δf_2 and Δf_4 but also on $\tilde{x}_2$ and $\tilde{x}_4$ are selected by the designer. Note that k_3 and k_4 may be set to zero and stable observer dynamics are still assured.

APPENDIX E

DERIVATION OF A.M.M. MODEL

The first three flexible modes and the rigid body mode will be modeled. The four independent and continuously differentiable basis functions suggested by Ginsberg [12] are

$$\psi_1(x) = 1 \tag{E.1}$$

$$\psi_2(x) = \cos\left(\frac{\pi x}{2L}\right) \tag{E.2}$$

$$\psi_3(x) = \cos\left(\frac{\pi x}{L}\right) \tag{E.3}$$

$$\psi_4(x) = \cos\left(\frac{3\pi x}{2L}\right) \tag{E.4}$$

where x is the location along the link and L is the link length.

The distributed parameter model considers the state of displacements, forces, moments and stresses at the ends of the link, known as boundary conditions. Zero slope at the guided end is represented by the boundary condition, for i = 1 to 4,

$$\psi_i{}'(0) = 0 . \tag{E.5}$$

Note that the last three basis functions satisfy the boundary condition above. They vanish at the location on the link where it does not deflect. Since rigid body motion is possible for this motion system, the first basis function satisfying free-free boundary conditions for the link must be included. The Ritz series representation of displacement w, velocity $\dot{w}$ and acceleration $\ddot{w}$ is given by

$$w(x,t) = \sum_{i=1}^{N} q_i(t)\psi_i(x) \tag{E.6}$$

$$\dot{w}(x,t) = \sum_{i=1}^{N} \dot{q}_i(t)\psi_i(x) \qquad \text{(E.7)}$$

$$\ddot{w}(x,t) = \sum_{i=1}^{N} \ddot{q}_i(t)\psi_i(x) \qquad \text{(E.8)}$$

where q are generalized coordinates.

The kinetic energy of the link and the lumped tip mass is

$$T = \frac{1}{2}\int_0^L \rho A \dot{w}^2 dx + \frac{1}{2}\sum m\dot{w}(x_m,t)^2 \qquad \text{(E.9)}$$

$$= \frac{1}{2}\sum_{i=1}^{4}\sum_{j=1}^{4} \dot{q}_i \dot{q}_j m_{ij} \qquad \text{(E.10)}$$

where L is the length of the link, ρ is the density, A is the cross sectional area, m is the lumped tip mass and w is displacement. x_m is the location of the tip mass. Note the tip mass moves in unison with the link. m_{ij} is given by

$$\int_0^L \rho A \psi_i(x)\psi_j(x)dx + m\psi_i(x_m)\psi_j(x_m). \qquad \text{(E.11)}$$

The potential energy of the link, also known as strain energy, is found by integrating over the link length as

$$V = \frac{1}{2}\int_0^L EI\ddot{w}^2 dx \qquad \text{(E.12)}$$

$$= \frac{1}{2}\sum_{i=1}^{4}\sum_{j=1}^{4} q_i q_j k_{ij} \qquad \text{(E.13)}$$

where E is Young's modulus and I is the cross-sectional area moment of inertia. k_{ij} is given by

$$\int_0^L EI\ddot{\psi}_i(x)\ddot{\psi}_j(x)dx. \qquad \text{(E.14)}$$

The power dissipated due to the viscoelastic effect and the external discrete damper is

$$P_{dis} = \int_0^L \gamma EI \left(\frac{\partial^2 \dot{w}}{\partial x^2} \right)^2 dx + \sum c(\dot{w}(x_c,t))^2 \qquad \text{(E.15)}$$

$$= \sum_{i=1}^4 \sum_{j=1}^4 C_{ij} \dot{q}_i \dot{q}_j \qquad \text{(E.16)}$$

where γ is the loss factor and c is the damping coefficient of the discrete damper located at x_c. The viscoelastic effect refers to energy dissipated under deformation of a purely elastic material. Hence it is the consideration of structural damping in the model. C_{ij} is given by

$$\int_0^L \gamma EI \ddot{\psi}_i(x) \ddot{\psi}_j(x) dx + c\psi_i(x_c)\psi_j(x_c). \qquad \text{(E.17)}$$

The power input to the link by the concentrated transverse force F is

$$P_{in} = \sum F\dot{w}(x_F,t) \qquad \text{(E.18)}$$

$$= \sum_{i=1}^4 Q_i \dot{q}_i \qquad \text{(E.19)}$$

where F is applied at location x_F. Q_i is given by

$$F\psi_i(x_F). \qquad \text{(E.20)}$$

By substituting the basis functions into the expressions for T, V, P_{dis}, and P_{in}, we obtain

$$m_{ij} = \int_0^L \rho A \cos\left(\frac{(i-1)\pi x}{2L} \right) \cos\left(\frac{(j-1)\pi x}{2L} \right) dx + m \cos\left(\frac{(i-1)\pi}{2} \right) \cos\left(\frac{(j-1)\pi}{2} \right) \qquad \text{(E.21)}$$

$$k_{ij} = \int_0^L EI \left[\cos\left(\frac{(i-1)\pi x}{2L} \right) \right]'' \left[\cos\left(\frac{(j-1)\pi x}{2L} \right) \right]'' dx \qquad \text{(E.22)}$$

$$c_{ij} = \int_0^L \gamma EI \left[\cos\left(\frac{(i-1)\pi x}{2L} \right) \right]'' \left[\cos\left(\frac{(j-1)\pi x}{2L} \right) \right]'' dx + c \qquad \text{(E.23)}$$

123

and

$$Q_i = F \cos\left(\frac{(i-1)\pi x_F}{2L}\right).$$

(E.24)

The integrals were evaluated analytically and verified by the math software Maple.

$$\underline{M} = \rho A L \begin{bmatrix} 1 & \dfrac{2}{\pi} & 0 & \dfrac{-2}{3\pi} \\ \dfrac{2}{\pi} & \dfrac{1}{2} & \dfrac{2}{3\pi} & 0 \\ 0 & \dfrac{2}{3\pi} & \dfrac{1}{2} & \dfrac{6}{5\pi} \\ \dfrac{-2}{3\pi} & 0 & \dfrac{6}{5\pi} & \dfrac{1}{2} \end{bmatrix} + m \begin{bmatrix} 1 & 0 & -1 & 0 \\ 0 & 0 & 0 & 0 \\ -1 & 0 & 1 & 0 \\ 0 & 0 & 0 & 0 \end{bmatrix}$$

(E.25)

$$\underline{K} = \frac{EI}{L^3} \begin{bmatrix} 0 & 0 & 0 & 0 \\ 0 & \dfrac{\pi^4}{32} & \dfrac{\pi^3}{6} & 0 \\ 0 & \dfrac{\pi^3}{6} & \dfrac{\pi^4}{2} & \dfrac{27\pi^3}{10} \\ 0 & 0 & \dfrac{27\pi^3}{10} & \dfrac{81\pi^4}{32} \end{bmatrix}$$

(E.26)

$$\underline{C} = \gamma \underline{K} + c \begin{bmatrix} 1 & 1 & 1 & 1 \\ 1 & 1 & 1 & 1 \\ 1 & 1 & 1 & 1 \\ 1 & 1 & 1 & 1 \end{bmatrix}$$

(E.27)

The 4x4 matrix of ones in equation 2.22 results from evaluating the trigonometric basis functions at the location of the dashpot along the beam, at x=0. The viscoelastic effect for most materials is negligible in the presence of external dashpots. The generalized forces are

$$\underline{Q} = F \begin{bmatrix} 1 \\ 1 \\ 1 \\ 1 \end{bmatrix}.$$

(E.28)

The equations of motion are

$$\underline{M}\ddot{\underline{q}} + \underline{C}\dot{\underline{q}} + \underline{K}\underline{q} = \underline{Q} \tag{E.29}$$

where q are generalized coordinates, M is the inertia matrix, C is the damping matrix, K is the stiffness matrix and Q are the generalized forces. Proceeding to modal analysis, the general eigenvalue problem leads to the eigenvalues (vibration modes) and eigenvectors (mode shapes). For obtaining free vibration modes, we only need the inertia and stiffness matrices.

Solving the general eigenvalue problem

$$\left(\underline{K} - \lambda \underline{M}\right)\underline{\phi} = \underline{0} \tag{E.30}$$

leads to the eigenvalues

$$\omega = \sqrt{\frac{EI}{\rho A L^4}}\sqrt{\lambda} . \tag{E.31}$$

In this work, Matlab was used to solve the general eigenvalue problem. The normalized eigenvectors

$$\underline{\Phi} = \frac{\underline{\phi}}{\left(\underline{\phi}^T \underline{M}\, \underline{\phi}\right)^{\frac{1}{2}}} \tag{E.32}$$

are used to convert the equations of motion from generalized coordinates q to modal coordinates η by decoupling the modes as

$$\underline{q} = \underline{\Phi}\,\underline{\eta} . \tag{E.33}$$

The decoupled equations of motion

$$\ddot{\underline{\eta}} = \underline{\Phi}^T \underline{Q} - \underline{\Phi}^T \underline{C}\underline{\Phi}\,\dot{\underline{\eta}} - [diag(\omega^2)]\underline{\eta} \tag{E.34}$$

may now be written in state space form.

$$\begin{bmatrix} x_1 \\ x_2 \\ x_3 \\ x_4 \\ x_5 \\ x_6 \\ x_7 \\ x_8 \end{bmatrix} = \begin{bmatrix} \eta_1 \\ \eta_2 \\ \eta_3 \\ \eta_4 \\ \dot{\eta}_1 \\ \dot{\eta}_2 \\ \dot{\eta}_3 \\ \dot{\eta}_4 \end{bmatrix} \tag{E.35}$$

$$\underline{\dot{x}} = \underline{A}\underline{x} + \underline{B}\underline{u} \tag{E.36}$$

The modal coordinates in conjunction with the basis functions are used to evaluate displacement at the base of the link and the acceleration at the link tip, at instants of interest.

$$\underline{y} = \begin{bmatrix} w(x=0,t) \\ \ddot{w}(x=L,t) \end{bmatrix} = \underline{\psi}(x)\Phi\underline{\eta} = \underline{C}x + \underline{D}\underline{u} \tag{E.37}$$

APPENDIX F

LABVIEW CODE FOR SIMULATIONS

Figure F.1: Complete block diagram for simulation.
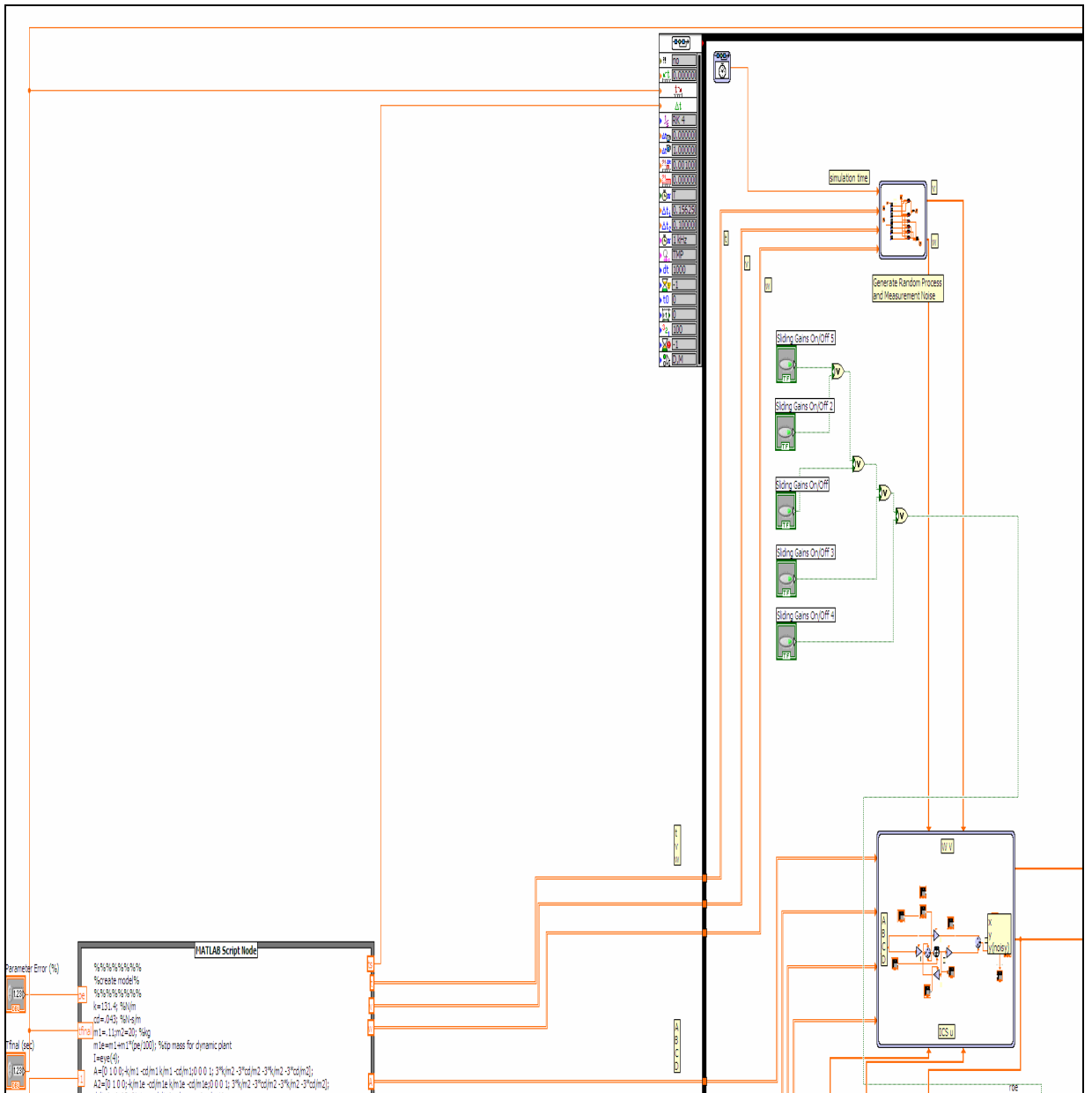
Figure F.2: Top-left of block diagram for simulation.
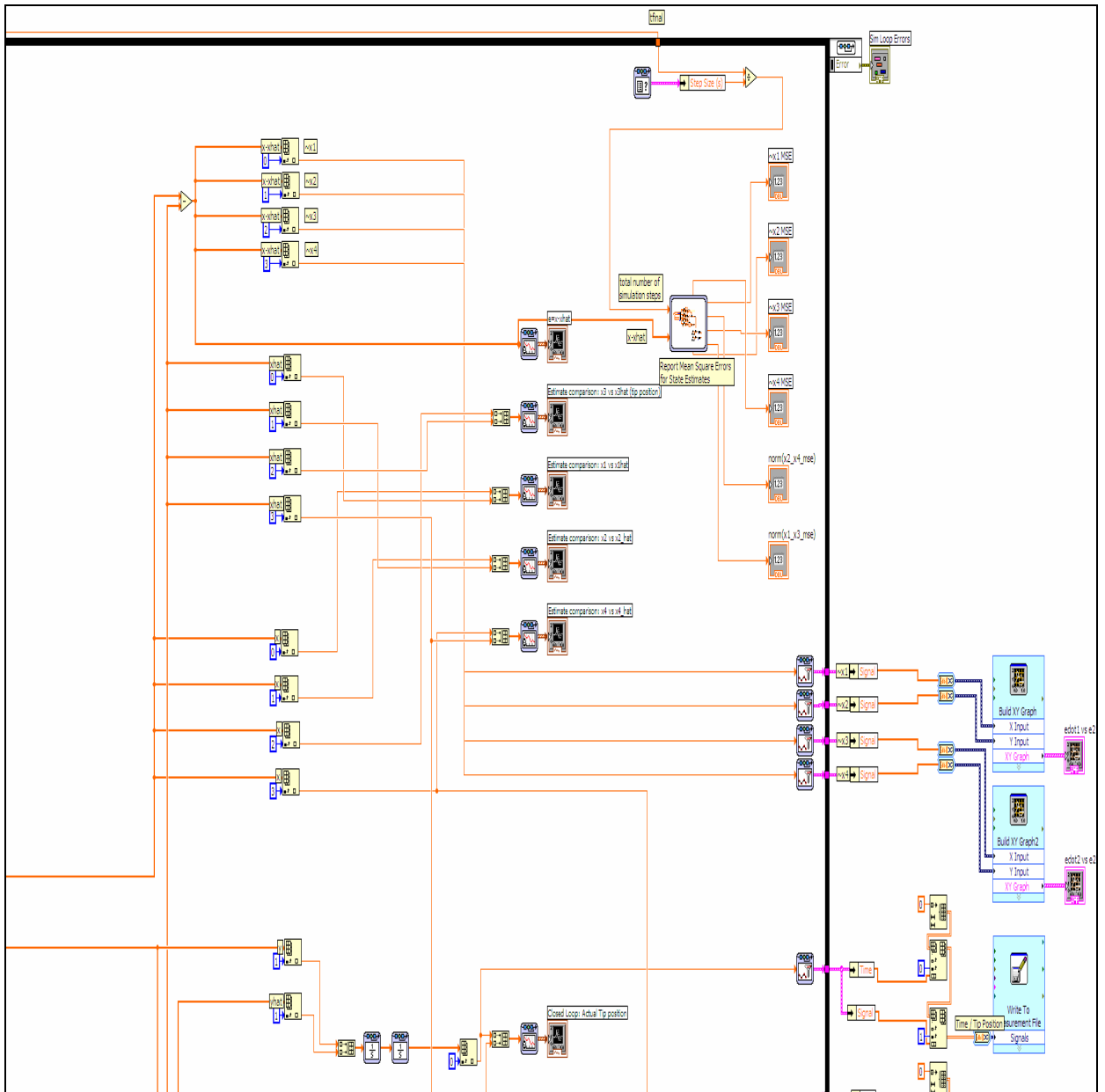
Figure F.3: Top-right of block diagram for simulation.

Figure F.4: Bottom-left of block diagram for simulation.
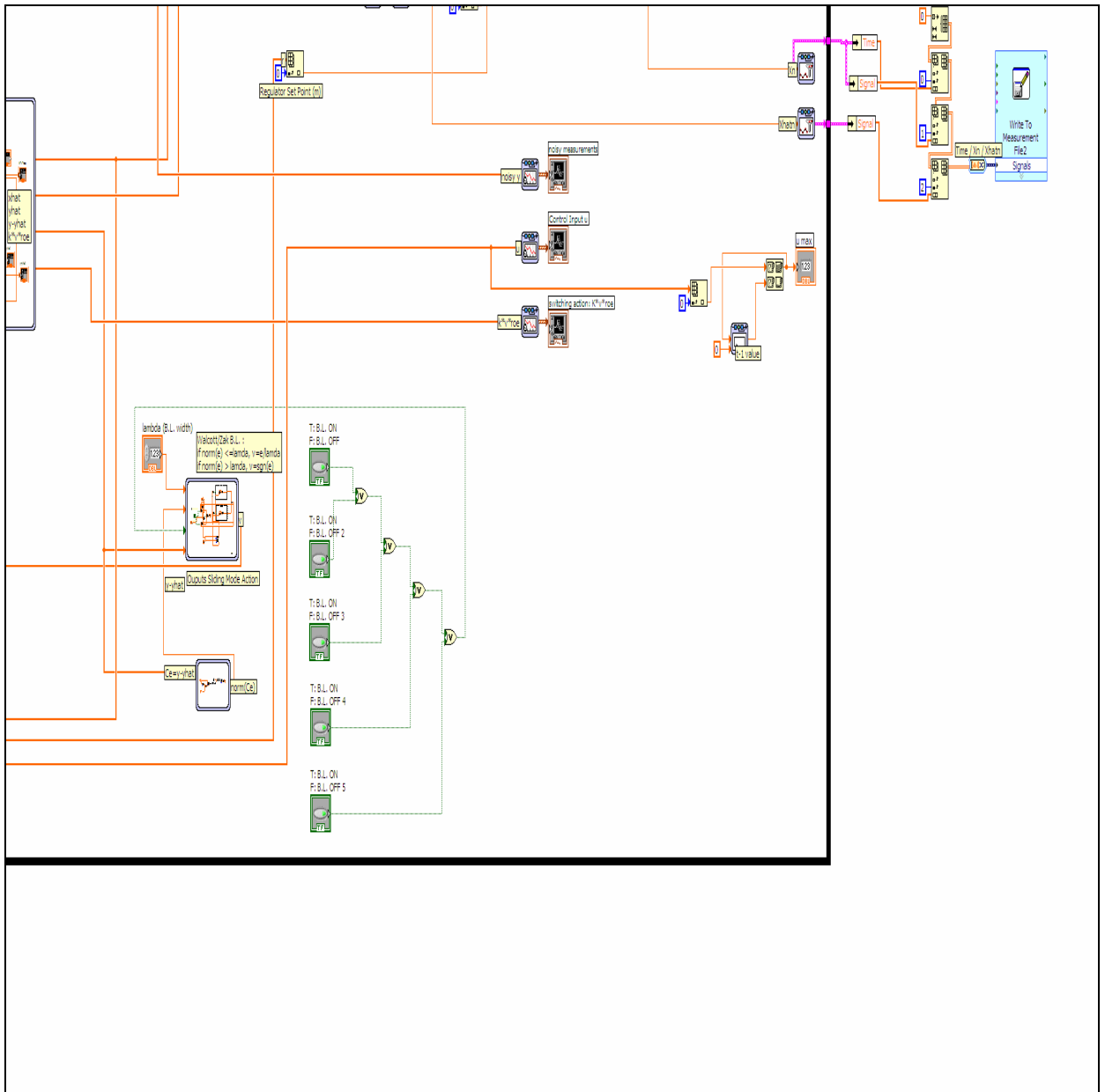
Figure F.5: Bottom-right of block diagram for simulation.

Contents of Matlab Script Node for lumped parameter model:

```
% Create model
k=131.4; %N/m
cd=.043; %N-s/m
m1=.11;m2=20; %kg
m1e=m1+m1*(pe/100); %tip mass for dynamic plant
I=eye(4);
A=[0 1 0 0;-k/m1 -cd/m1 k/m1 -cd/m1;0 0 0 1; 3*k/m2 -3*cd/m2 -3*k/m2 -3*cd/m2];
A2=[0 1 0 0;-k/m1e -cd/m1e k/m1e -cd/m1e;0 0 0 1; 3*k/m2 -3*cd/m2 -3*k/m2 -
3*cd/m2];
```

```matlab
deltaA=A-A2; %given: deltaA+observerA=plantA
B=[0; 0; 0; 3/m2];
%C=[0 0 1 0;1 0 0 0]; %output base position and tip position
%C=[0 0 1 0;0 1 0 0]; %output base position and tip velocity
C=[0 0 1 0;-k/m1 -cd/m1 k/m1 -cd/m1]; %output base position and tip accel
C2=[0 0 1 0;-k/m1e -cd/m1e k/m1e -cd/m1e]; %output base position and tip accel
D=[0;0];
plant=ss(A,B,C,D);
plantd=ss(A2,B,C2,D);
ts=.001;
t=[0:ts:tfinal]';

% Generate measurement noise
R1=3.87e-10; %st.dev squared
R2=2.59e-4; %st.dev squared
R=[R1 0;0 R2];
Q=3e-4; %inherited from regulator tuning on test-bed
[junk2,KFL,junk1,junk] = kalman(plantd,Q,R); %Kalman filter based on A2
v1=sqrt(R1)*randn(length(t),1);
v2=sqrt(R2)*randn(length(t),1);
v=0*[v1 v2];
w1=sqrt(Q)*randn(length(t),1);
w2=sqrt(Q)*randn(length(t),1);
w3=sqrt(Q)*randn(length(t),1);
w4=sqrt(Q)*randn(length(t),1);
w=0*[w1 w2 w3 w4];

% Solve matrix lyapunov equation
Q11=i1; %weight y1 and y2
Q33=Q11;
Q22=i1; %weight ydot1 and ydot2
Q44=Q22;
Q2=diag([Q11 Q22 Q33 Q44],0); %Q2 is pos def sym matrix
P=lyap(A2-KFL*C2,Q2);
P_eig=eig(P);
K=inv(P)*C2'; %sliding mode gain based on A2

% Closed loop gain
Csrl=[1 0 0 0]; %penalize only the tip position
Dsrl=0;
[num,den]=ss2tf(A2,B,Csrl,Dsrl); %open-loop TF
systf=tf(num,den);
[nrows,ncols]=size(den);
flipsign=ones(nrows,ncols);
for i=0:ncols-1
    flipsign(ncols-i)=(-1)^(ncols-i);
```

```
end
num2=flipsign.*num;
den2=flipsign.*den;
srl=systf*tf(num2,den2); %new open-loop TF for SRL
[clp,junk]=rlocus(srl,rho); %find closed loop poles for SRL
stable_clp=clp(find((clp)<0)); %isolate stable closed loop poles
KCL=acker(A2,B,[stable_clp]); %shortcut for pole placement

% Feedforward gain
H=[A2 B; 1 0 0 0 0];
J=[zeros(1,4) 1]; %set reference point for tip pos
N1=inv(H)*J';
Nx=[N1(1,1);N1(2,1);N1(3,1);N1(4,1)];
Nu=[N1(5,1)];
Nbar=[Nu+KCL*Nx];
F=Nbar;
```

Contents of Matlab Script Node for assumed modes method model:

```
% Create model
m=0.25; %kg
p=9.8375e+003; %kg/m^3
h=0.0024;
b=0.0399;
A=b*h; %xsection height*base in m
E=2.0500e+011; %Pa or N/m^2
I=(1/12)*b*h^3; %m^4
L=0.4800; %m
c=35; %motor damping (N-s/m) found by matlab optimization
LF=1e-6; %arbitrary loss factor
mhat=p*A*L*[1+m 2/pi -m -2/(3*pi); 2/pi .5 2/(3*pi) 0; -m 2/(3*pi) .5+m 6/(5*pi); -
2/(3*pi) 0 6/(5*pi) .5];
khat=((E*I)/(L^3))*[0 0 0 0; 0 (pi^4)/32 (pi^3)/6 0;0 (pi^3)/6 (pi^4)/2 (27*pi^3)/10;0 0
(27*pi^3)/10 (81*pi^4)/32];
chat=LF*khat+c*ones(4,4); %damping due to viscoelastic effect + motor damping
[phi,W2]=eig(khat,mhat);
[wn,isort]=sort(sqrt(diag(W2)));
phi=phi(:,isort);
scale=phi.'*mhat*phi; %check: scale is always I!!
PHI=phi*inv(sqrt(scale)); %normalize evectors
PHI=real(PHI);

m2=m+(pe/100)*m;
p=9.8375e+003; %kg/m^3
h=0.0024;
b=0.0399;
```

```matlab
A=b*h; %xsection height*base in m
E=2.0500e+011; %Pa or N/m^2
I=(1/12)*b*h^3; %m^4
L2=L-(pe/100)*L; %m
c=35; %motor damping (N-s/m) found by matlab optimization
LF=1e-6; %arbitrary loss factor
mhat2=p*A*L2*[1+m2 2/pi -m2 -2/(3*pi); 2/pi .5 2/(3*pi) 0; -m2 2/(3*pi) .5+m2
6/(5*pi); -2/(3*pi) 0 6/(5*pi) .5];
khat2=((E*I)/(L2^3))*[0 0 0 0; 0 (pi^4)/32 (pi^3)/6 0;0 (pi^3)/6 (pi^4)/2 (27*pi^3)/10;0 0
(27*pi^3)/10 (81*pi^4)/32];
chat2=LF*khat2+c*ones(4,4); %damping due to viscoelastic effect + motor damping
[phi2,W22]=eig(khat2,mhat2);
[wn2,isort2]=sort(sqrt(diag(W22)));
phi2=phi2(:,isort2);
scale2=phi2.'*mhat2*phi2; %check: scale is always I!!
PHI2=phi2*inv(sqrt(scale2)); %normalize evectors
PHI2=real(PHI2);%normalized evectors for dyn. Plant
%transform to modal coordinates:
Q=[1 1 1 1]';
cnew=PHI'*chat*PHI;
cnew2=PHI2'*chat2*PHI2;

A=[zeros(4) eye(4);-diag(wn)^2 -cnew];
A2=[zeros(4) eye(4);-diag(wn2)^2 -cnew2];
deltaA=A-A2;
B=[0; 0; 0; 0; PHI'*Q];
B2=[0; 0; 0; 0; PHI2'*Q];
C=[[1 1 1 1]*PHI 0 0 0 0;[1 0 -1 0]*PHI*-diag(wn)^2 [1 0 -1 0]*PHI*-cnew]; %output
base position and tip accel
C2=[[1 1 1 1]*PHI2 0 0 0 0;[1 0 -1 0]*PHI2*-diag(wn2)^2 [1 0 -1 0]*PHI2*-cnew2];
%output base position and tip accel
D=[0;[1 0 -1 0]*PHI*PHI'*Q];
D2=[0;[1 0 -1 0]*PHI2*PHI2'*Q];
plant=ss(A,B,C,D);
plantd=ss(A2,B2,C2,D2);
ts=.0005;
t=[0:ts:tfinal]';

% Generate measurement noise
R1=3.87e-10;
R2=2.59e-4;
R=[R1 0;0 R2];
Q=1e-6;
[junk2,KFL,junk1,junk] = kalman(plantd,Q,R); %based on A2, B2, C2, D2
v1 = sqrt(R1)*randn(length(t),1);
v2=sqrt(R2)*randn(length(t),1);
```

```matlab
v=0*[v1 v2];
w1=sqrt(Q)*randn(length(t),1);
w2=sqrt(Q)*randn(length(t),1);
w3=sqrt(Q)*randn(length(t),1);
w4=sqrt(Q)*randn(length(t),1);
w5=sqrt(Q)*randn(length(t),1);
w6=sqrt(Q)*randn(length(t),1);
w7=sqrt(Q)*randn(length(t),1);
w8=sqrt(Q)*randn(length(t),1);
w=0*[w1 w2 w3 w4 w5 w6 w7 w8];

% Solve matrix lyapunov equation
Q11=i1; %weight y1 and y2
Q22=i1;
Q33=i1;
Q44=i1;
Q55=i1b;
Q66=i1b;
Q77=i1b;
Q88=i1b;
Q2=diag([Q11 Q22 Q33 Q44 Q55 Q66 Q77 Q88],0); %Q2 is pos def sym matix
P=lyap(A2-KFL*C2,Q2);
P_eig=eig(P);
K=inv(P)*C2';

% Close loop gain:
Csrl=[[1 0 -1 0]*PHI2 0 0 0 0]; %penalize only the tip position
Dsrl=0;
[num,den]=ss2tf(A2,B2,Csrl,Dsrl); %open-loop TF
systf=tf(num,den);
[nrows,ncols]=size(den);
flipsign=ones(nrows,ncols);
for i=0:ncols-1
    flipsign(ncols-i)=(-1)^(ncols-i);
end
num2=flipsign.*num;
den2=flipsign.*den;
srl=systf*tf(num2,den2); %new open-loop TF for SRL
[clp,junk]=rlocus(srl,rho); %find closed loop poles for SRL
stable_clp=clp(find((clp)<0)); %isolate stable closed loop poles
KCL=acker(A2,B2,[stable_clp]); %shortcut for pole-placement

% Feedforward gain
H=[A2 B2;[1 0 -1 0]*PHI2 0 0 0 0 0];
J=[zeros(1,8) 1]; %set reference point for tip pos
N1=inv(H)*J';
```

```
Nx=[N1(1,1);N1(2,1);N1(3,1);N1(4,1);N1(5,1);N1(6,1);N1(7,1);N1(8,1)];
Nu=[N1(9,1)];
Nbar=[Nu+KCL*Nx];
F=Nbar;
```

APPENDIX G

MATLAB CODE FOR SYSTEM IDENTIFICATION

```
clear all ; close all ; clc ;
global t y u N
data = xlsread('OL_data3'); %read time, pos, u
%This is the main function for estimating model parameters using
%numerical optimization.

% Time vector
Tf=9.04;
Ts=0.001;
t=[5:Ts:Tf]';
N=length(t);
% Estimated system parameters (note that very poor initial guesses result
% in drastically different final values).
Km=8.17; % overall motor gain [N/V]
M=9.6; % base mass [kg]
b=50; % track-base damping [N*s/m]
Kmup=Km+Km*.25;
Kmdn=Km-Km*.25;
Mup=M+M*.10;
Mdn=M-M*.10;

% Use estimated parameters for initial guesses and set limits.
X0=[Km M b];
LB=[Kmdn Mdn 0];
UB=[Kmup Mup Inf];
%Experimental data
u=data(1:N,3);
y=data(1:N,2)/100; %recorded position converted to meters

% Optimization parameters.
options.MaxIter=500;
options.MaxFunEvals=1000;
options.Display='iter';
options.TolFun=1e-8;
options.TolX=1e-8;
pause
```

% Estimate model parameters based using numerical optimization.
X=fmincon('pos_error',X0,[],[],[],[],LB,UB,[],options); %note that pos_error is being
called without specfying intial X
pause

% Return system parameters from optimization results.
Km=X(1)
M=X(2)
b=X(3)

% Set up system
Gs=linear_track(X);
out=lsim(Gs,u,t);
ybase=out(:,1);
% Plot results and compare with experimental data.
figure
plot(t,u,'r','linewidth',2)
xlabel('time [s]')
ylabel('input voltage [V]')
grid on
title('Motor Input')
figure
plot(t,y,'r','linewidth',2)
hold on
plot(t,ybase,'m--','linewidth',2)
legend('base (data)','base (model)',4)
grid on
xlabel('time [s]')
ylabel('position [m]')
title('Linear Track Ramp Response')
save Trackmodel Gs X

function Gs=linear_track(X)
% This function returns LTI model of the linear track
% based on input parameters.
Km=X(1);
M=X(2);
b=X(3);
% Set up system
Gs=tf([Km],[M b 0])

```matlab
function F=pos_error(X)
% This function computes the error between the data and the theoretical model
% over the course of the simulation.
global t y u N
% Compute system model for these parameters.
Gs=linear_track(X);
% Simulate system using input data.
out=lsim(Gs,u,t);
yth=out(:,1);
% Sum the total error between data and simulation output vectors.
% This is the quantity to minimize in the optimization.
F=0;
for i=1:N
F=F+(y(i)-yth(i))^2;
end
F
```

REFERENCES

[1]   W.J. Book, "Structural flexibility of motion systems in space environment," *IEEE Transactions on Robotics and Automation*, Vol. 9, No. 5, pp. 524-530, Oct. 1993.

[2]   W.J. Book, "Flexible robot arms," *Robotics and Automation Handbook*., pp. 24.1-24.44, CRC Press, Boca Raton, FL, 2005.

[3]   R.H. Cannon and E. Schmitz, "Initial experiments on the end-point control of a flexible one-link robot," *International Journal of Robotics Research*, 1984.

[4]   J.B. Hoagg and D.S. Bernstein, "Nonminimum-phase zeros," *IEEE Control Systems Magazine*, June 2007.

[5]   R.H. Cannon and D. E. Rosenthal, "Experiments in control of flexible structures with noncolocated sensors and actuators," *J. Guidance*, Vol. 7, No. 5, Sept.-Oct. 1984.

[6]   J.J. Slotine et al., "On Sliding Observers for Nonlinear Systems," *Journal of Dynamic Systems, Measurement, and Control*, vol. 109, pp. 245-252, Sept. 1987.

[7]   N.G. Chalhoub and G.A. Kfoury, "Development of a robust nonlinear observer for a single-link flexible manipulator," *ASME International Mechanical Engineering Congress & Exposition*, Nov. 13-19, 2004.

[8]   G.A. Kfoury et al., "Enhancement of the accuracy of the (P-w) method through the implementation of a nonlinear robust observer," *Journal of Sound and Vibration*, Vol. 291, No. 3-5, Apr. 4, 2006.

[9]   M-H. Kim and D.J. Inman, "Reduction of observation spillover in vibration suppression using a sliding mode observer," *Journal of Vibration and Control*, vol. 7, pp. 1087, 2001.

[10] E.M. Elbeheiry and H.A. Elmaraghy, "Robotic manipulators state observation via one-time gain switching," *Journal of Intelligent and Robotic Systems*, 38, pp. 314-344, 2003.

[11] A. Zaki et al., "Variable structure observer design for flexible-link manipulator control," *Transactions of the Canadian Society of Mechanical Engineering*, Vol. 27, No. 1&2, 2003.

[12] J.H. Ginsberg, *Mechanical and Structural Vibrations*, John Wiley & Sons, Inc.: New York, 2001.

[13] P.S. Maybeck, *Stochastic Models, Estimation and Control: Vol. 1*, Academic Press: New York, 1979.

[14] A. Gelb, *Applied Optimal Estimation*, MIT Press: Cambridge, 1974.

[15] B.L. Walcott and S.H. Zak, "Observation of dynamical systems in the presence of bounded nonlinearities/undecertainties," *Proceedings of the IEEE 25th Conference on Decision and Control*, pp. 961-966, Dec. 1986.

[16] T. Kailath, *Linear Systems*, Prentice Hall: New Jersey, 1980

[17] G.F. Franklin et al., *Feedback Control of Dynamic Systems*, Prentice Hall: New Jersey, 2001.

[18] W.J. Book, "Modeling, design, and control of flexible manipulator arms: a tutorial review," *Proceedings of the 29th Conference on Decision and Control*, Dec. 1990.

[19] D.L. Girvin, "Numerical analysis of right-half plane zeros for a single-Link manipulator," M.S. Thesis, Georgia Institute of Technology, Mar. 1992.